UNIVERSITY OF CALIFORNIA,
IRVINE

Water vapor addition in high concentrations to the fuel side of a two-dimensional methane/air diffusion flame

DISSERTATION

submitted in partial satisfaction of the requirements
for the degree of

DOCTOR OF PHILOSOPHY

in Mechanical and Aerospace Engineering

by

Michela Vicariotto

Dissertation Committee:
Professor Derek Dunn-Rankin, Chair
Professor Jack Brouwer
Professor Vince McDonell

2019

DEDICATION

A Leila e Emilio.
Emma, Saffron e Federico.
To my family and friends.

TABLE OF CONTENTS

LIST OF FIGURES

LIST OF TABLES

ACKNOWLEDGMENTS

This work was supported with funds from the National Science Foundation under grant CBET 1605533, with Song-Charng Kong as program manager.

CURRICULUM VITAE

Michela Vicariotto

EDUCATION

Doctor of Philosophy in Mechanical and Aerospace Engineering **2019**
University of Caliornia, Irvine *Irvine, US*

Master of Science in Space Engineering **2015**
Plitecnico di Milano *Milano, Italy*

Bachelor of Science in Aerospace Engineering **2012**
Plitecnico di Milano *Milano, Italy*

REFEREED JOURNAL PUBLICATIONS

Temperature Measurement of Glowing Firebrands **2019**
Fire Technology

James Urban, Michela Vicariotto, Derek Dunn-Rankin, Carlos Fernandez-Pello

Temperature profiles and extinction limits of a coflow water-vapor laden methane/air diffusion flame **2018**
Experiments in Fluids

Michela Vicariotto, Derek Dunn-Rankin

ABSTRACT OF THE DISSERTATION

Water vapor addition in high concentrations to the fuel side of a two-dimensional methane/air diffusion flame

By

Michela Vicariotto

Doctor of Philosophy in Mechanical and Aerospace Engineering

University of California, Irvine, 2019

Professor Derek Dunn-Rankin, Chair

The understanding of thermal and chemical effects of water addition to the fuel side of a diffusion flame is relevant for improving the combustion of naturally wet fuels such as methane hydrates, emulsified fuels and wet biomass, as well as for cases where water is intentionally added to the fuel stream, as for example in steam-assisted flares for the reduction of emissions. In this work, the role of water is evaluated by adding high concentrations of water vapor to the fuel side of a steady non-premixed coflow flame. The steady nature of the flame allows temperature profiles, extinction limits, and OH relative concentrations to be measured at different conditions of inlet velocities, with increasing dilution levels. This work is unique in its attention to the very high dilution levels near extinction and in the detailed measurement campaign providing comprehensive information for laminar 2-D diffusion flames. Temperatures are measured with thin filament pyrometry (TFP). Results from Ar, N_2 and CO_2 diluted flames are also reported to compare the effects of water vapor with those of different diluents. Comparisons in terms of temperatures and extinction limits show close correspondence when adding equivalent levels of diluent thermal capacitance. OH concentrations are obtained through planar laser-induced fluorescence (PLIF) for water and carbon dioxide diluted flames. For a better understanding of the fluorescence signal, and of the radical pool in the combustion process, the experimental measurements

are complemented with results from CFD simulations of the flame. Results confirm that both water and CO_2 are not passive thermal diluents in flames but contribute to chemical pathway changes, particularly near extinction. The difference between these two diluents is evident in that water vapor diluted flames lift before extinguishing while CO_2 diluted flames simply blow out. In addition to assessing the chemical versus thermal role of water dilution in non-premixed flames, this work provides a comprehensive data collection to validate numerical simulations, providing sufficient information to help to assess uncertainties in third body efficiencies of water and shifts in chemical paths when high concentrations of diluents are introduced in the combustion process.

Chapter 1

Introduction

1.1 Water dilution in combustion

Water is a a major product of all hydrogen and hydrocarbon/air reactions, but when added intentionally to the combustion process it can also be considered a non-reactive diluent. The concept of water introduction in combustion systems can be found in early 1900's literature as a means to improve fuel atomization and to protect the turbine section of gas turbine systems. Later, water addition was investigated in numerous articles to provide internal cooling to Otto-cycle engines and to relieve knocking characteristics [1]. Dryer, in his review paper [1], reports the extended literature concerning water addition to practical combustion systems but also highlights the lack of fundamental considerations and studies. He believed the lack of information to be due to non predictable conclusions and results that appeared from water addition studies up to that point suggesting the need for a more in depth understanding of the physical and chemical effects of water, when introduced to the combustion environment. In fact, while as a diluent water can be used beneficially for fire suppression [2, 3], and for decreasing peak flame temperatures to reduce soot [4, 5] and NOx [6, 7, 8] emissions, it can

also act as a reactant or at least as a potential decomposition species that can affect the combustion reaction chemistry. This more subtle contribution to combustion with excess water present has led to some uncertain conclusions and it is the main topic of this work.

1.1.1 Water dilution in premixed flames

Many of the studies found in the literature regarding water diluted combustion investigate the role of liquid and vapor water addition in premixed flames.

Mazas, et al. [9] investigated the effects of water vapor on premixed oxygen-enriched methane flames. They experimentally and numerically measured laminar burning velocities of a axisymmetric conical flame, with water up to 0.45 molar fractions in the reactive mixture. They showed a quasi-linear decrease in burning velocity of the methane flame with increasing water concentrations. The numerical results predicted well this trend for the larger dilution levels, but not for cases of water concentrations below 10% in volume. They also observed that steam addition reduces O and H concentrations while increasing OH concentrations. However, this chemical effect appears to be strongly attenuated when the oxygen concentration is increased in the reactive mixture. They concluded that, for highly oxygen enriched flames, steam can be considered as an inert diluent.

These results were in part consistent with the work of Le Cong and Dagaut [10] who studied the effects of water in hydrogen and methane premixed combustion in a jet-stirred reactor. From reaction path analyses they showed that 10% water addition favors O radical consumption and OH production in the reaction:

$$H_2O + O \rightleftharpoons OH + OH \tag{1.1}$$

which removes O, inhibiting methane oxidation in:

$$CH_4 + O \rightleftharpoons CH_3 + OH \tag{1.2}$$

while, in the absence of water, O atoms would significantly react with methane. Similarly, slower consumption of methane in the presence of water is also an effect of the competition between reactions:

$$H + O_2 + M \rightleftharpoons HO_2 + M \tag{1.3}$$

$$CH_4 + H \rightleftharpoons CH_3 + H_2 \tag{1.4}$$

Their analyses showed that consumption of H is increased in reaction:

$$H + O_2 + M \rightleftharpoons HO_2 + M \tag{1.5}$$

where M is water, which competes with

$$H + O_2 \rightleftharpoons OH + O \tag{1.6}$$

because of the high third body efficiency of water. Those results are in agreement with the fundamental discussion on the role of water in chain-branching reactions by Glassman [11], who reports that water vapor tends to inhibit production of H radical in reaction 1.3. Apart from the inhibition of methane consumption with water addition, Le Cong and Dagaut also observed reduced NOx formation, flame speeds, and adiabatic temperatures.

The key finding from the water dilution studies in premixed flames was, therefore, that water is chemically active species that shifts the population of the more reactive atomic radicals O and H to the less reactive radical OH.

1.1.2 Water dilution in diffusion flames

Non-premixed (or diffusion flame) combustion is important in fires and power applications. Many of the works regarding water addition in diffusion flames utilize either a counterflow configuration with dilution on the oxidizer [12, 13, 14, 15, 7] or fuel side [16, 17], or a coflow configuration with water added to the oxidizer stream [18, 19, 20].

Seiser and Seshadri [12] investigated the influence of water addition on extinction and ignition of hydrogen and methane laminar premixed and diffusion flames. Their experimental and numerical setup involved a counterflow flame where water vapor was added to either the reactants (premixed) or the oxidizer stream (non-premixed) in percentages up to 20% by mass. For each water concentration, the vapor was substituted for nitrogen in such a way to maintain the adiabatic flame temperature constant. They observed a lower extinction strain rate and a higher autoignition temperature as steam was added to the reactants. These behaviors suggest a weaker flame, one that requires higher temperature to initiate and one that can be extinguished with lower flow perturbation. They suggested that the chemical effect of water dilution is mainly related to the high chaperon efficiency in three body reactions which appears to be uncertain, highlighting the need to accurately establish such efficiencies.

Suh and Atreya [13] looked at the temperature profiles, soot and OH radical concentrations in counterflow diffusion flames with water added to the oxidizer side in concentrations up to 0.4 mole fraction. They maintained the molar flow rate and specific heat roughly constant in the oxidizer side by substituting nitrogen with a mixture of water vapor and argon. They reported an increase in maximum flame temperature and OH concentrations. However, OH concentration appeared to increase up to 0.3 water mole fraction, but for higher dilution the OH pool remained the same. The authors referred to this as a turning point before which the chemical enhancement of water vapor is dominant, and after which the physical effect

of suppression becomes more important. Apart from the variations in OH concentrations, other evidence of this turning point can be seen from concentrations of CH_3 radicals. CH_3 is mainly produced in the reaction:

$$CH_4 + H \rightleftharpoons CH_3 + H_2 \tag{1.7}$$

Differently from [10], they observed an increase in the production of CH_3, and thus a more active flame, caused by an increase in production of H atoms when water was added to the system in concentrations up to 0.3 mole fractions. For higher water levels, CH_3 concentrations decreased.

Park, et al. [14] numerically studied a diffusion counterflow H_2 flame with water added on either the oxidizer or fuel side in concentrations up to 0.6 mole fractions. To better understand the chemical effects of water dilution, they introduced an artificial molecule with water thermo-chemical, transport and radiation properties but that is not allowed to participate in any chemical reaction. Results showed an increase in OH concentrations and maximum flame temperature between addition of water and the chemically inert version only for low levels of dilution. Maximum mole-production rates of OH for different chain branching reactions showed the same behavior. However, they reported significant differences between dilution in the fuel and oxidizer streams. A later work from the same group [21], performed a similar study in counterflow methane-air flames. As in the case of H_2 flames, they showed increases in maximum temperatures and OH concentrations only for small water mole fractions (0.1).

Wang, et al. [15] performed numerical simulations of a counterflow diffusion methane flame, diluted with up to 30% water vapor in volume on the oxidizer side. Artificial species were introduced to identify the thermal and chemical effects of water. Contrary to [14], this work showed larger differences in maximum flame temperatures between water and the artificial

molecules at higher water dilution levels. They showed that production rates of H decreased with water addition in reactions $O + H_2 \rightleftharpoons OH + H$ and $OH + H + M \rightleftharpoons H_2O + M$. At the same time, $OH + OH \rightleftharpoons O + H_2O$ and $OH + H_2 \rightleftharpoons H + H_2O$ mainly increased production of OH. In $CH_2O + OH = HCO + H_2O$ the production rate of HCO decreased and the production rate of CH_2O increased with water. Because of the decrease of H and the increase in OH, production rate of CO decreased for $CO + OH \rightleftharpoons CO_2 + H$, while the decrease of HCO and increase of CH_2O induced the production of CO in $HCO \rightleftharpoons H + CO$ and $CH_2(s) + CO_2 \rightleftharpoons CH_2O + CO$ to decrease. However, the work concluded that the thermal and chemical effects of water on the flame temperature cancel each other out.

Zhao, et al. [7] numerically simulated the behavior of counterflow methane-air diffusion flames with steam addition in the air stream in concentrations up to 10% by volume. Under constant flow rates of air and methane conditions, they reported decreasing temperatures and OH concentrations with water addition if initial temperatures are kept constant, and increasing temperatures and OH concentrations with the rise of initial temperatures. To isolate the chemical effect of steam, they fixed the maximum flame temperature by changing the reactants inlet temperatures as water dilution increased (higher inlet T for higher dilution levels). Doing so, they reported an increase in OH with water at constant flame temperature. However, it is not clear whether this result is due to water addition or to changes in the initial temperatures, or in which proportions those two effects contribute to the change in OH concentrations.

Lee, at al. [16] studied the extinction limits and the structure of counterflow diffusion methane-air flames with water added on the fuel side to concentrations up to 0.4 mole fractions. They showed good agreement between predicted and measured temperature trends. Their results reported decreasing flame temperatures with water addition at constant strain rates due to dilution and cooling effects. The works also showed that lower strained flames can sustain higher amounts of added water before extinction occurs. The authors concluded

that chemical effects of water addition on flame structure are negligible.

Padilla, et al. [17] investigated the influence of water addition to the fuel side of a counterflow flame. Their experimental and computational work showed that water chemically affects the production and depletion of O, H and OH radicals. They reported OH concentration measurements to differ from chemical kinetics simulation results suggesting that more work is needed to clarify the role of the third body efficiency of water in the flame chemistry.

Liu, et al. [18] numerically studied the effects of adding steam, in volume concentrations up to 10%, to the oxidizer stream of an ethylene/air coflow diffusion flame. The work isolated the chemical, dilution and radiation effects of water vapor and showed a reduction in flame temperature and soot loading with water addition.

Xu, et al. [19] studied the effect of water vapor on the structure and shape of a laminar coflow non-premixed syngas flame. The work reported numerical and experimental results when water was replaced with N_2 in the oxidizer stream in concentrations up to 0.3 mole fractions. Experimental results for temperatures along the flame centerline and flame heights were compared to numerical simulations, showing good agreement in the trends. The importance of chemical, thermal, transport and radiative effects of water dilution were studied numerically by using artificial species, as described earlier. The work concluded that water addition in the oxidizer stream decreases the centerline temperature less effectively than CO_2 dilution. They reported that water has a fairly small influence below about three quarters of the flame heights as, in this region, the thermal and radiative effects tend to decrease temperature while the chemical and transport effects increase it. However, at higher streamwise positions in the flame, all effects considered resulted in a temperature decrease. They also showed that chemical effects enhance OH production, but thermal and radiative effects from water are to decrease OH concentrations. This work distinguishes behaviors of water addition in different parts of the 2-D coflow flame although the water is added to the base oxidizer stream. This potential for variable effects along the reaction interface is important

for the current work since a 2-D coflow geometry is employed.

Dai, at al. [20] investigated the characteristics of a coflow methane flame, with steam addition in the oxidizer stream. The coflow oxygen level was varied from 3% to 85% by volume, while N_2 diluent was replaced with H_2O. The work numerically showed that the temperature and size of the flame reduced when water was substituted to nitrogen. Such reductions are due to the lower density and higher thermal capacity of water with respect to N_2. Water was found to increase the flame lift-off distance more than nitrogen, due to a longer ignition delay. Differences in flame behavior between the two diluents became more important with increasing dilution levels.

1.2 Motivation

Table 1.1 reports a summary of the studies found in the literature regarding water addition to diffusion flames. The table shows: (1) whether the results are experimental (E) and/or numerical (N); (2) the flame configurations analyzed and the conditions used to increase the level of water dilution; (3) the maximum amount of dilution reached. As can be seen from the table and from the literature review, the role of water addition in combustion has several facets that have not been resolved, particularly in the case of non-premixed combustion when water dilutes the fuel. To create a clear picture of watery-fuel flame combustion, the present study is focused on water dilution in steady non-premixed coflow flames where the diluent is added to the fuel side, extending the work of [17] on counterflow flames to a coflow geometry. This configuration permits high-fidelity measurements and is relevant for a number of combustion applications. Some examples include: combustion of methane hydrates [22], emulsified fuels [23, 24], gel fuels [25], and undried biomass [26], or the behavior of pool fires developing from LNG or oil on water, and steam-assisted flares for the reduction of emissions.

Figure 1.1 shows images of the coflow flame used in this work, at different water dilution concentrations.

Figure 1.1: Laminar water-laden methane/air coflow flame at different water dilution levels: $X_{H_2O} = 0, 0.2, 0.4, 0.6$.

In addition to the lack of information regarding this configuration, Table 1.1 shows the wide spread of conditions used and parameters kept constant during the different studies. Many researchers chose their test conditions differently, generating difficulties and confusion when results are to be compared. The choice of the condition to run is usually related to the authors' interest to isolate a particular effect. In fact, the literature agrees that the change in combustion intensity by water addition is caused by five possible mechanisms: the dilution effect decreases the concentration of the reactants; the thermal effect results from the change in specific heat of the streams when water is added; the chemical effect appears as water participates in the chemical reactions; the radiation effect results from alterations in radiation heat transfer rates in the flames caused by water addition; and the transport effect is caused by differences in transport properties of the streams as dilution increases [27]. Many of the numerical works try to isolate those effects by introducing artificial species. However, in experimental tests, complications arise when trying to do so. This results in a wide array of conditions investigated. Moreover, it is clear from Table 1.1 that most of the studies looked at water concentrations below 40%, but it is of particular interest to understand the behavior of the flame close to the extinction limits as this is where the water vapor will have its most significant impact. Flames that are slightly diluted are strong and fairly impervious to upset, but when getting near the extinction limits, the special behaviors begin to dominate. It is

at these limit conditions that the potential for flame control and optimization are generally found (minimum emission, for example).

Thus, this work is driven by three main motivations: (i) the understanding of the thermal and chemical effects of water when added at high levels, in the fuel side of a nonpremixed flame. Whether water acts as a special diluent with respect to others (such as CO_2, N_2 or Ar) is relevant to practical combustion systems. (ii) The investigation of possible multidimensional effects of a diluent, which is important because flames in practical combustion applications are often multidimensional. The laminar coflow diffusion flame is used for this study as it is a simple multidimensional model from which it is relatively easy to understand the role of heat transfer, fluidynamics and chemical reactions in the combustion process. It is of interest to understand whether the behavior of water diluted flames can be completely described in 1D flames, or whether 2D effects can play a role in the process. Moreover, the 2D coflow flame is more suitable than the counterflow flame configuration for future study at high pressure, thanks to its more compact design and lower gas flow rates needed. (iii) The importance of providing the data to assess uncertainties in third body efficiencies of water and shifts in chemical paths with increasing water dilution. Several studies reported uncertainties in the values of chaperon efficiency of water and highlighted the need to improve the accuracy of chemical mechanisms [12, 17, 28]. Sabia, at al. [28] in their numerical and experimental study of a surrogate for biogas in presence of large water amounts, reported results from several kinetic models showing larger differences between the models and the experiments as water dilution increased. They suggested that the kinetic models are not able to predict auto-ignition delay data as a result of differences in the modeling of the radical production rates and distributions. The authors reported the need to improve the predictability of the mechanisms in non-standard conditions (high water concentrations).

Article	Num/exp	Configuration	Max H_2O dilution
[12]	E + N	Counterflow - Oxidizer dilution, constant adiabatic flame T by replacing N_2 dilution with H_2O	20% mass
[13]	N	Counterflow - Oxidizer dilution, constant molar flow rate and specific heat by substitution of N2 with mixture of Ar and H_2O	40% molar
[14]	N	Counterflow - Oxidizer and Fuel dilution, constant strain rate	60% molar
[15]	N	Counterflow - Oxidizer dilution, constant strain rate	30% molar
[7]	N	Counterflow - Oxidizer dilution, constant maximum flame T by varying water concentrations and inlet Ts	10% molar
[16]	E + N	Counterflow - Fuel dilution, constant strain rate	40% molar
[17]	E + N	Counterflow - Fuel dilution, constant methane flow rate	65% mass
[18]	N	Coflow - Oxidizer ddilution, constant air flow rate (velocity increases with water addition)	10% molar
[19]	E + N	Coflow - Oxidizer ddilution, constant oxidizer volumetric flow rate, N_2 replaced with water	30% molar
[20]	N	Coflow - Oxidizer ddilution, constant oxidizer velocity	80% molar
[29]	N	Coflow - Oxidizer ddilution, constant oxidizer flow rate (velocity increases with water addition)	10% molar

Table 1.1: Water diluted diffusion flames in the literature.

1.3 Objectives

The objectives of this work can be summarized as follows:

- Obtain high precision measurements of temperature and OH concentrations of a coflow diffusion flame with high dilution of water vapor on the fuel side. High fidelity measurements require the development of a reliable system to seed the fuel line with water vapor.
- Identify the humidification limits of highly water diluted diffusion flames.
- Isolate the thermal and chemical effects of water on the combustion reaction process, and identify differences in behaviors between water vapor and other gaseous diluents.
- Compare experimental results to numerical prediction to test the validity of the chemistry mechanism when high concentrations of water are introduced into the combustion process.

1.4 Outline of the dissertation

Chapter 1 reports a summary of the literature review concerning water dilution in combustion applications, and the motivation and objectives of the work. The experimental setup is described in Chapter 2, together with the experimental techniques used to measure temperatures, OH concentrations, and CH* and OH* chemiluminescence. Chapter 3 reports detailed temperature profiles and extinction limits of the water-laden methane/air coflow diffusion flame. Temperature measurements and extinction limits are also reported for flames diluted with Ar, N_2, and CO_2 to compare the effects of water to different diluents. OH concentrations profiles, obtained experimentally for different test conditions, are also presented. Numerical

models are introduced in Chapter 4. Numerical and experimental results are discussed in Chapter 5. Chapter 6 summarizes the conclusions and future work.

Chapter 2

Experimental setup and description

The experimental set-up consist of two main parts: a water addition systems that seeds water vapor into the methane fuel line and a burner. Figure 2.1 report a simple schematic of the set-up. In the next sections, a more detailed description of the main parts of the experimental system is provided.

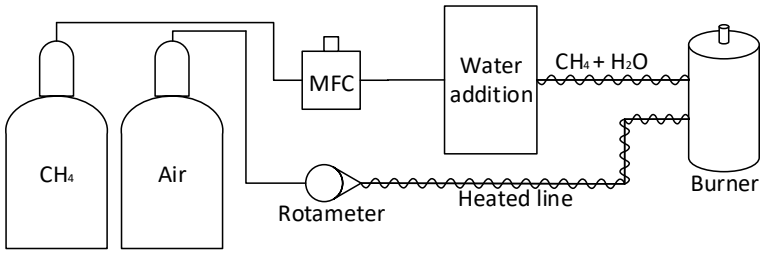

Figure 2.1: Experimental set-up schematic.

2.1 Water addition system

Dilution with water vapor is obtained by flowing the fuel gas through a 40 mL gas bubbler, filled with distilled water and placed into a water bath (Figure 2.2). The bath temperature, and thus the temperature of the water in the bubbler, is controlled by a commercial temperature controlled heater with an accuracy of 0.1 °C. The heater also provides recirculation in the bath to ensure homogeneous temperature. Methane saturates with water vapor as it bubbles through the distilled water. The water mole fraction in the fuel flow, X_{H_2O}, is:

$$X_{H_2O} = \frac{p_{H_2O}(T_b)}{p} \tag{2.1}$$

where $p_{H_2O}(T_b)$ is the water saturation pressure at the bath temperature T_b and p is the total pressure of 1 atm [30].

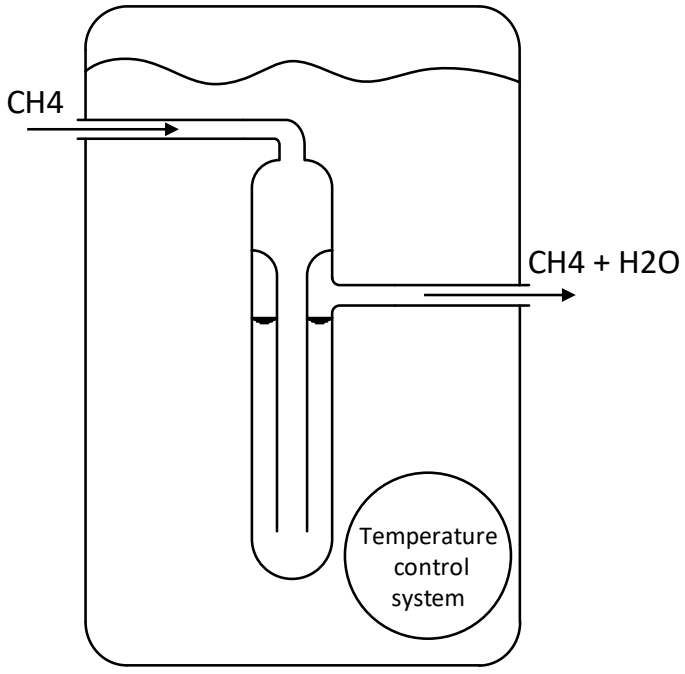

Figure 2.2: Water addition system.

The water addition system was tested at fourteen different temperature conditions (between 30 and 93 °C) flowing air as carrier gas at 40 mL/min. Air bubbled through the system for 30 minutes, and the glass bubbler was weighed before and after to obtain the amount of water lost. Each temperature condition was tested three times. The average water mole fraction in the exiting flow, for each temperature, is reported in Figure 2.3 and compared to the theoretical predictions. The difference between the predicted and the measured water mole fraction in the exiting fuel flow is below 1% up to 87 °C (which corresponds to $X_{H_2O} = 0.61$). Above 87 °C, the difference increases with temperature (up to a maximum of 2.8% at 93 °C) as the amount of water evaporated in time becomes more sensitive to small temperature variations. Figure 2.4 shows how the theoretical mass of water lost becomes more sensitive to temperature variations as temperature increases. Each tested condition showed high repeatability, with a standard deviation on the measured water mole fraction for the three runs always below 0.0015 in mole fraction. The calibration curve shows both that the system has high repeatability and that the contact time and bubble size are sufficient to ensure that the water vapor fully saturates the gas at each condition.

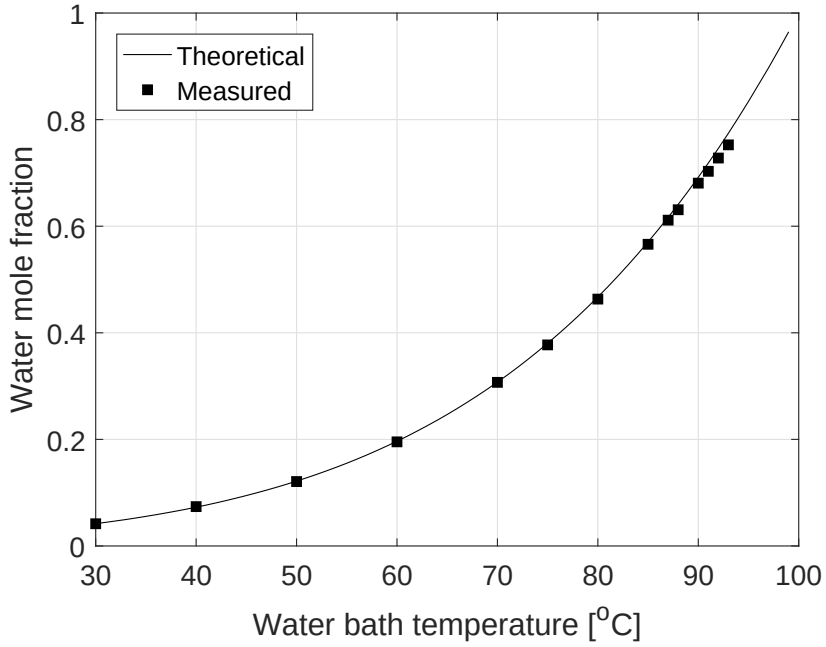

Figure 2.3: Theoretical vs measured water mole fraction.

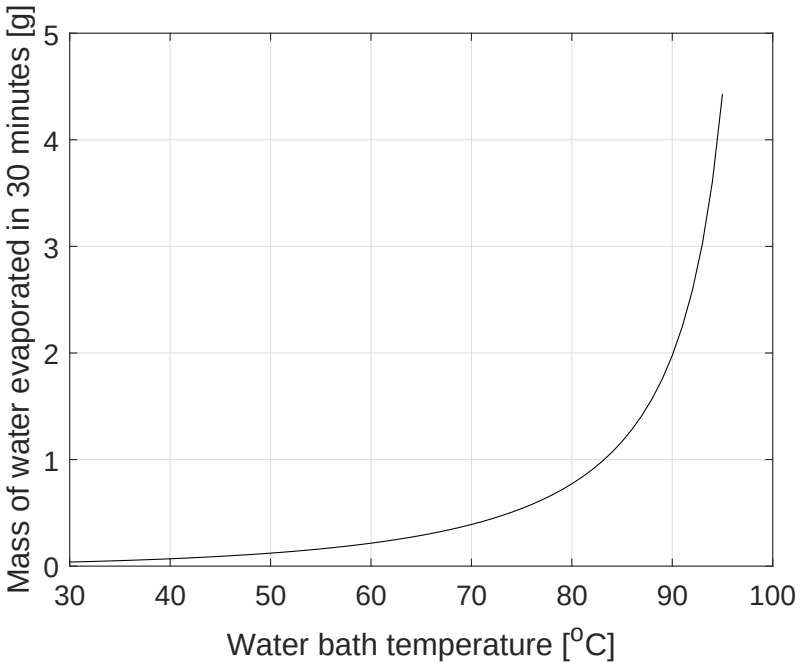

Figure 2.4: Theoretical mass of water lost in 30 minutes with air flowing at 40 mL/min.

2.2 Burner

The laminar diffusion flame is established on a co-annular burner (Figure 2.5) with a fuel tip (inner diameter of 1.8 mm, outer diameter of 2.2 mm) surrounded by a 2.54 cm inner diameter air nozzle. The fuel tube length (7 cm) is sufficient to ensure a fully developed parabolic velocity profile, while the Reynolds number in the fuel tube is always below 100. The outer oxidizer tube is filled with 3.175 mm diameter brass beads, and a stainless steel honeycomb mesh with cell diameter of 1.52 mm is placed at its exit to obtain approximately a top-hat air velocity profile [31]. The fuel tube extends above the honeycomb mesh by 6 mm. The air volumetric flow rates are controlled using a rotameter with an accuracy of $\pm 2\%$ FS (on the full scale). Mass flow controllers of $\pm 1\%$ FS accuracy are used to set the methane flow rate condition, as well as for adding Ar, N_2, and CO_2 as diluents to the fuel line. A check valve with a 1 psi pressure drop is placed after the water addition system, in the fuel line, to damp the fuel flow oscillations caused by the bubbling of methane through water. The fuel line, after dilution, is wrapped in heating tape to prevent condensation when water

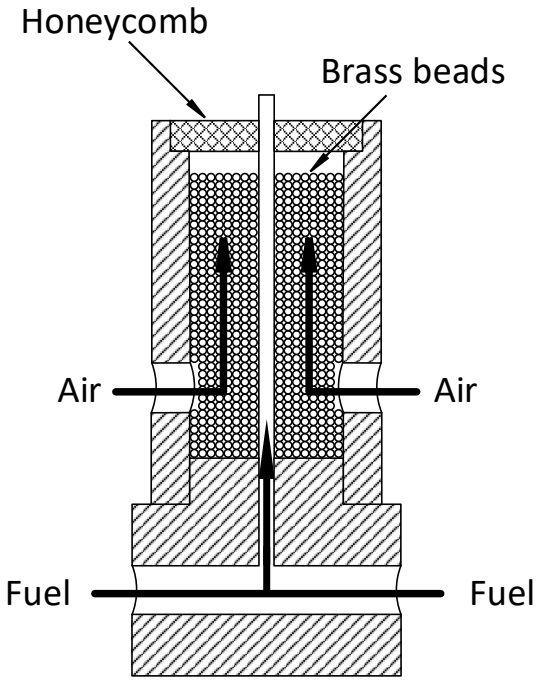

Figure 2.5: Burner.

is added. The oxidizer line and the burner walls are also heated to avoid local condensation or water droplet effects in the burner or at the fuel tube exit. The lines are heated also when methane is diluted with Ar, N_2, or CO_2 to ensure always the same temperature of 510 $\pm$ 10 K at the burner exit for both air and fuel.

2.3 Thin filament pyrometry

2.3.1 Measurements method

TFP was first introduced for combustion by [32, 33] and has then been widely used in several reacting flow environments. Uncertainties related to the use of thin-filament pyrometry are small, having been found by [34] to be 30 K in the temperature measurements of a coflowing methane/air diffusion flame. Similarly, [35] reported temperature uncertainties to

be between 36 K and 45 K, depending on the experimental approach employed. Their study also investigated fiber aging and spectral emissivities. The current work employs the best practices recommended by these earlier comprehensive works in TFP.

A 14 μm Ceramic Grade Nicalon SiC fiber is placed in the flame and imaged with a Nikon D90 DSLR camera. A GB40 color filter, manufactured by SCHOTT INC., is placed between the camera lens and the flame to prevent saturation of the red channel. The signal I of the glowing fiber can be correlated to its temperature T using the Planck's law for graybodies:

$$I(\lambda, T) = \frac{2\epsilon hc^2}{\lambda^5 e^{hc/\lambda kT} - 1} \tag{2.2}$$

where λ is the wavelength, ϵ is the fiber emissivity (0.88) and h, c and k are the Planck's constant, the speed of light and the Stefan-Boltzmann constant, respectively. The camera detected signal $D(T)$ can be calculated as a function of the fiber temperature integrating I over the range of response of the camera ($\lambda_1 = 400$ nm, $\lambda_2 = 720$ nm):

$$D(T) = \eta \int_{\lambda_1}^{\lambda_2} I(\lambda, T)\tau(\lambda)S(\lambda)d\lambda \tag{2.3}$$

where η is the constant that accounts for the efficiency of the light collection system, $\tau(\lambda)$ is the transmittance of the color filter, and $S(\lambda)$ is the spectral response of the camera. The spectral response of the camera was obtained through calibration. The output of a tungsten lamp was imaged with the camera through a monochromator, obtaining images every 5 nm in the range 400-720 nm. The light relative intensity was captured with a spectrometer to normalize for the difference in light intensity at different wavelengths (more details on the calibration procedure and instruments can be found in [36]).

Two approaches can be used to obtain temperature from Equation 2.3: intensity ratio, or

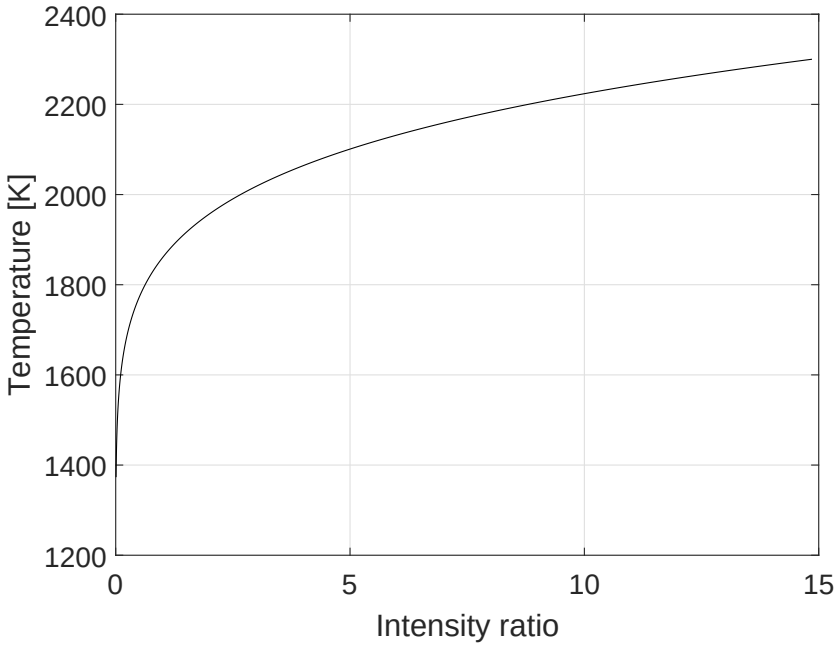

Figure 2.6: Intensity ratio vs temperature.

color ratio. Equation 2.4 shows the equation related to the intensity ratio approach:

$$\frac{D(T)}{D(T_0)} = \frac{\int_{\lambda_1}^{\lambda_2} I(\lambda, T)\tau(\lambda)S(\lambda)d\lambda}{\int_{\lambda_1}^{\lambda_2} I(\lambda, T_0)\tau(\lambda)S(\lambda)d\lambda} \tag{2.4}$$

To solve for the temperature T, the camera detected signal $D(T_0)$ at a known temperature T_0 is needed as a calibration point. Figure 2.6 shows an example of the intensity-temperature relation. Alternatively, it is possible to consider the camera signals from the RGB (Red-Blue-Green) channels separately, and obtain temperatures using a color-ratio approach without the need of a calibration point. For example, considering red and blue channels:

$$\frac{R}{B} = \frac{\int_{\lambda_1}^{\lambda_2} I(\lambda, T)\tau(\lambda)S_R(\lambda)d\lambda}{\int_{\lambda_1}^{\lambda_2} I(\lambda, T)\tau(\lambda)S_B(\lambda)d\lambda} \tag{2.5}$$

In this work, Equation 2.5 is applied to three different color ratios: R/G, R/B, and G/B. A look-up table with the relations between color ratios and temperature is generated as shown Figure 2.7.

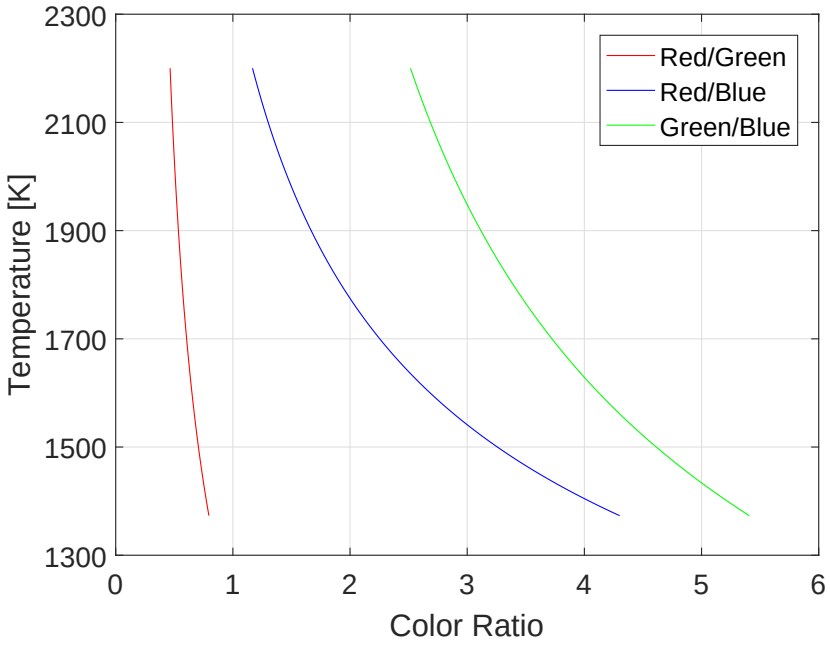

Figure 2.7: Color ratio vs temperature look up table.

For this study, a single point color-ratio is used to calibrate the intensity ratio based approach. Figure 2.8 shows the fiber temperature profiles obtained from processing a typical thin-filament pyrometry picture. Three different color ratios (R/G, G/B and G/B) and the calibrated intensity ratio show good agreement and an accuracy of about 50 K in the measurements. This is consistent with the uncertainties related to the use of thin-filament pyrometry found by Maun, et al. [34] to be 30 K in the temperature measurements of a coflowing methane/air diffusion flame. Similarly, Ma, at al. [35] carried on an detailed uncertainties analysis both on the measurement method and on the radiation corrections and reported uncertainties on the final temperature to be between 36 K and 45 K, depending on the experimental approach employed. The fluctuations seen in Figure 2.8 are also related to the possible unsteadiness in the flame during the camera exposure time.

TFP images were taken with a Nikkor 50 mm f/4 lens, exposure time of 1/1000 s, and ISO sensitivity between 200 and 320. The raw ".nef" format was used to minimize the internal built-in processing of the camera. The pictures were then processed with the open-source software DCRAW [37] to apply linear gamma correction, and demosaicking. A more detailed

discussion of the demosaicking method chosen is reported in Appendix A.

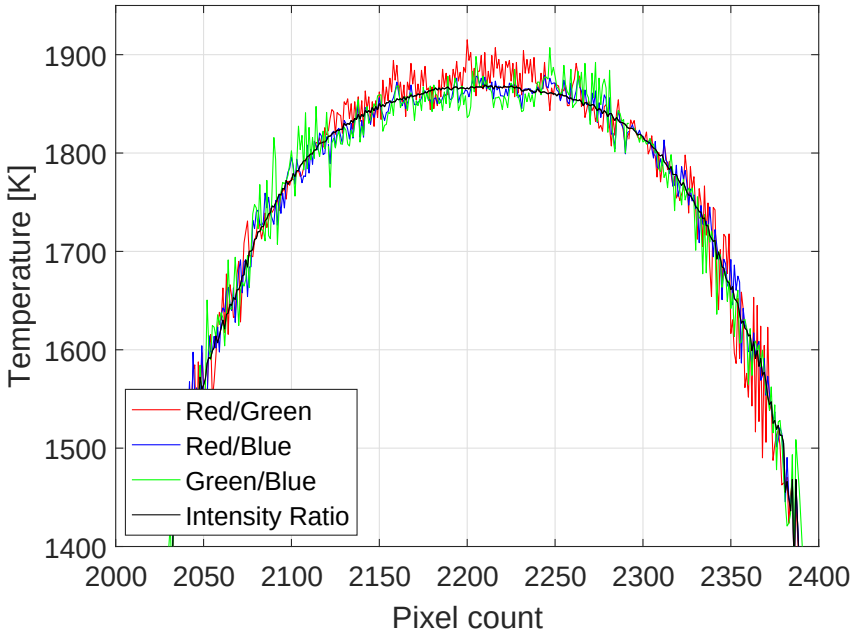

Figure 2.8: Temperature profile obtained with color-ratio and intensity ratio approaches of an imaged fiber.

2.3.2 Radiation corrections

Once the temperature of the fiber is determined, a radiation correction is necessary to retrieve the temperature difference between the fiber (T_f) and the surrounding gas (T_g). The fiber is heated by the hot gas and cooled by radiation losses, as described by equation 2.6. Conduction along the fiber can be neglected due to the low fiber thermal conductivity and diameter [33, 34, 35].

$$h(T_g - T_f) = \epsilon\sigma(T_f^4 - T_\infty^4) \tag{2.6}$$

In Equation 2.6, σ is the Stefan-Boltzmann constant, T_∞ is the ambient temperature, and h is the convective heat transfer coefficient calculated as:

$$h = \frac{Nu\ k}{d_f} \tag{2.7}$$

where k is the gas thermal conductivity, d_f is the fiber diameter and Nu is the Nusselt number obtained with the following correlation [35].

$$Nu = (0.8237 - 0.5\ln(Pe))^{-1} \qquad Pe < 0.2 \tag{2.8}$$

Pe is the Peclet number:

$$Pe = \frac{U d_f}{\alpha} \tag{2.9}$$

U is the gas velocity and α is the gas diffusivity. The gas phase properties needed to perform the corrections (k, U and α) are determined from CFD OpenFoam simulations of the coflow flame run at each dilution condition with a single-step chemistry (more details on the simulations can be found in Chapter 4). The gas properties are taken from the numerical results at each fiber position in the flame. Figure 2.9 shows a comparison between a temperature profile corrected with gas properties obtained from simulations run with a single-step chemistry, and with GRI-Mech 3.0 chemistry [38]. The maximum difference between the two profiles is 3.5 K; the use of a single-step mechanism versus GRI 3.0, in the computational model, has a negligible effect on the corrected temperatures for TFP. This is because the chemistry detail has little effect on the main thermal loss mechanisms from the fiber, as these depend on velocity and temperature. Thus, it is enough to run simulations with a single step-chemistry; running a more detailed mechanism does not affect the corrected temperatures while it requires a much larger computation time.

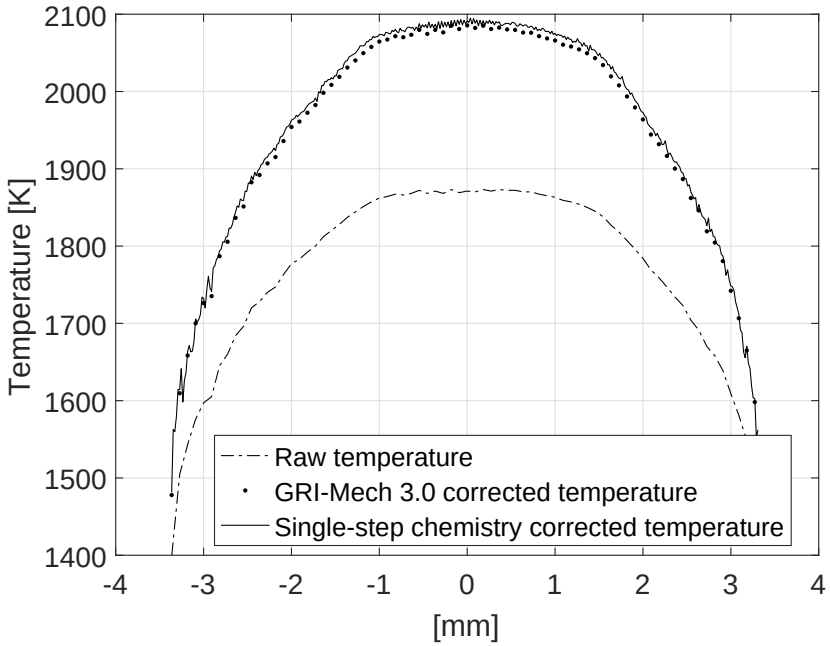

Figure 2.9: Radiation corrections using single-step vs GRI 3.0 chemistry in the simulations.

2.4 OH Planar laser-induced fluorescence

As discussed in Chapter 1, OH is an important molecule in water diluted flames. It has been identified in many of the mechanisms as responsible for special features associated with water chemistry. Measurements of relative concentrations of OH in the diluted flames are obtained with planar laser-induced fluorescence. Laser induced fluorescence, as depicted in Figure 2.10, can be described as a spontaneous radiation emission that arises because of the stimulation of an atomic or molecular system to an upper (excited) quantum state. In general, for diagnostic purposes, the fluorescence emission spectrum is different from that of the incident laser excitation to avoid interferences from spuriously scattered laser light or Mie scattering from particles present in the environment [39]. In PLIF, laser light is shaped into a thin sheet and passed through the regions of interest to excite fluorescent tracers in the flame to obtain 2D concentration measurements of the molecule under investigation. Unfortunately, collisional decay process can cause redistribution of population from the excited level, complicating the interpretation of experimental data. The increase in total decay rate

due to collisions is known as quenching. In addition to this, the fact that transitions between energy levels in atoms and molecular systems are not infinitely sharp must be taken into account. Line broadening affects the shape of the spectral signatures from the transition, impacting the interpretation and accuracy of experimental measurements. Lastly, the intensity of the coupling between the lower and upper quantum states transition is a function of temperature. This effect should also be accounted for when interpreting the measured fluorescence signal. The quantification of those three phenomena will be further discussed in Section 4.3.

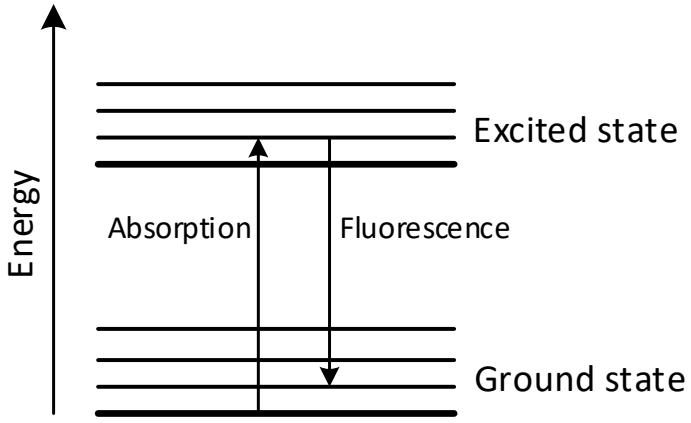

Figure 2.10: Fluorescence process.

OH PLIF measurements are taken by exciting OH with a 283.2 nm wavelength at the $Q_1(7)$ line in the $A^2\Sigma^+$–$X^2\Pi$ (1,0) band. The details for the transition choice are described in [40]. The setup includes a 532 nm Surelite III Nd:YAG laser, a Vista dye laser, and a doubling crystal; each laser shot has an energy of about 6 mJ. A plano-concave cylindrical lens with focal length of -10 cm is followed by a plano-convex cylindrical lens with focal length of 30 cm to create a laser sheet of 2.5 cm height. The OH fluorescence signal in the $A^2\Sigma^+$–$X^2\Pi$ (0,0), (1,1) band is detected using a EM-ICCD PIMAX-4 camera and a Semrock FF01-320/40-25 filter. 1000 images are taken at each condition, with a gate time of 75 ns. The OH signal images are then averaged, and a background picture of the flame, taken with no

laser excitation, is subtracted to avoid any effect from chemiluminescence or soot. Images of a dye cell with a mixture of methanol and Rhodamine 590 is used to correct the detected fluorescence signal for variations of the energy intensity in the laser sheet.

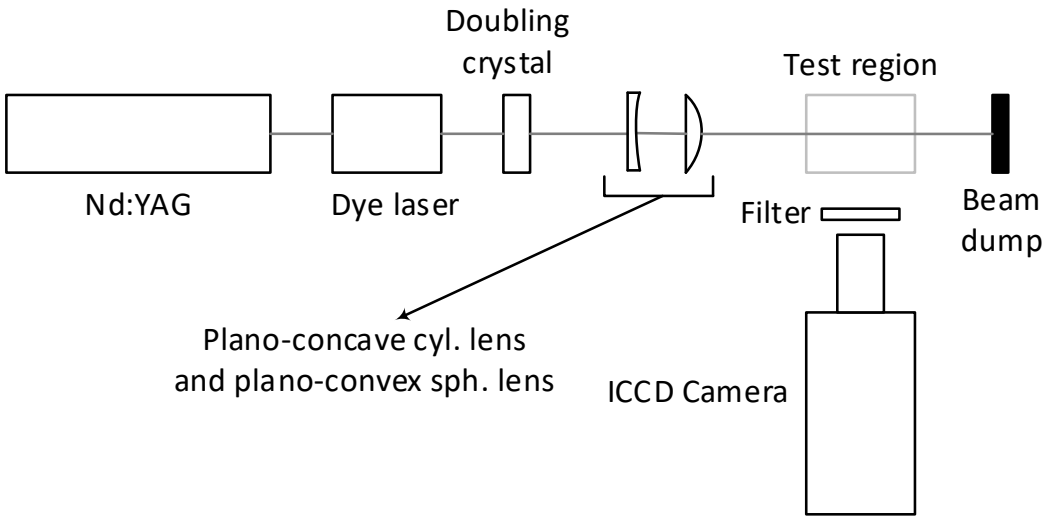

Figure 2.11: Schematic of the OH PLIF experimental setup.

2.5 OH* and CH* chemiluminescence

Chemiluminescence is the electromagnetic radiation emitted from the de-excitation of electronically excited species that are formed via chemical reactions in the combustion reaction zone [41]. Early work on OH chemiluminescence [42, 43] suggested that OH* is primarily formed in reaction:

$$CH + O_2 \rightleftharpoons CO + OH^*$$

The production of CH* was identified by [44] to be from:

$$C_2H + O \rightleftharpoons CO + CH^*$$

Chemiluminescence imaging is widely used in combustion as a diagnostic tool. The technique is straightforward to apply as no laser is needed, it typically requires for only a suitable collection optical system and a sufficient detector sensitivity [45]. The literature recognizes CH* and OH* to be the primary species responsible for much of the visible and ultraviolet luminescence in typical hydrocarbon-air flames. OH and CH chemiluminescence is then routinely employed to detect flame position, shape and structure, as they indicate the location of the reaction zone and of heat release [46, 47, 48].

In this work, OH chemiluminescence images were taken with the same camera system as in Figure 2.11. 100 images, taken using the EM-ICCD PIMAX-4 camera with an exposure of 100 ms, were averaged for each water dilution condition, and a background picture was subtracted. The CH chemiluminescence photographs were taken with the Nikon D90 camera, and without the use of a narrow band filter. Thus, the imaged signal is mainly due to CH^* with some contributions from ${C_2}^*$ and ${CO_2}^*$. In this work, chemiluminescence images are used as qualitative indicators of the location of heat release rate and are not meant for any quantitative analysis. Thus, being ${CO_2}^*$ also present in the high temperature reaction zone, its broadband contribution to the CH^* signal has not been isolated. The Abel inversion of the CH* images was performed using the three-point deconvolution technique, as in [49].

Chapter 3

Experimental results

This chapter provides the data and images of the diluted flames using the methods described in the prior chapter. As a reminder, the information includes chemiluminescence as a qualitative indicator of the locus of maximum reaction rate and the level of intensity of the heat release; the fluorescence is both a qualitative indicator of the extended reaction zone towards the oxygen side and a semi-quantitative measure of the radical concentration; and the TFP measurements provide quantitative temperature maps of the flames. These results are useful in direct comparison to determine the impact of dilution on these features and as a comprehensive data collection that can be used for model and simulation validation.

3.1 Flame appearance

Figures 3.1 and 3.2 show how the flame appears differently as larger amounts of water are added to the fuel. The images show the flame in two different conditions. The experiment in Figure 3.1 is run keeping the mass flow rate of methane constant at 35 mL/min in all the dilution conditions, so that the carbon input in the flame is constant for all dilution levels.

This means that the total mass flow rate of the fuel stream increases with water dilution. The images in Figure 3.2 are taken at increasing water amounts, but keeping the total mass flow rate of the fuel stream constant. Since the pictures were taken during TFP experiments, the SiC fiber is visible in the images, and the flame looks green as the BG40 filter is positioned in front of the camera. However, these pictures are not suitable for temperature information from the fibers because they are overexposed with respect to TFP images. In both mass flow rate conditions, it is possible to see that the luminous zone associated with soot dims and then disappears as water is added to the fuel. This agrees with the finding from Axelbaum and Law [50] that showed the effects of fuel concentration and temperature reduction on soot formation when an inert is added to the fuel of a diffusion flame. Liu et al. [18] proposed that water vapor addition to the oxidizer stream of a diffusion flame significantly reduces soot loading as the chemical effect of water lowers concentrations of propargyl, benzene and pyrene in the early stage of soot formation.

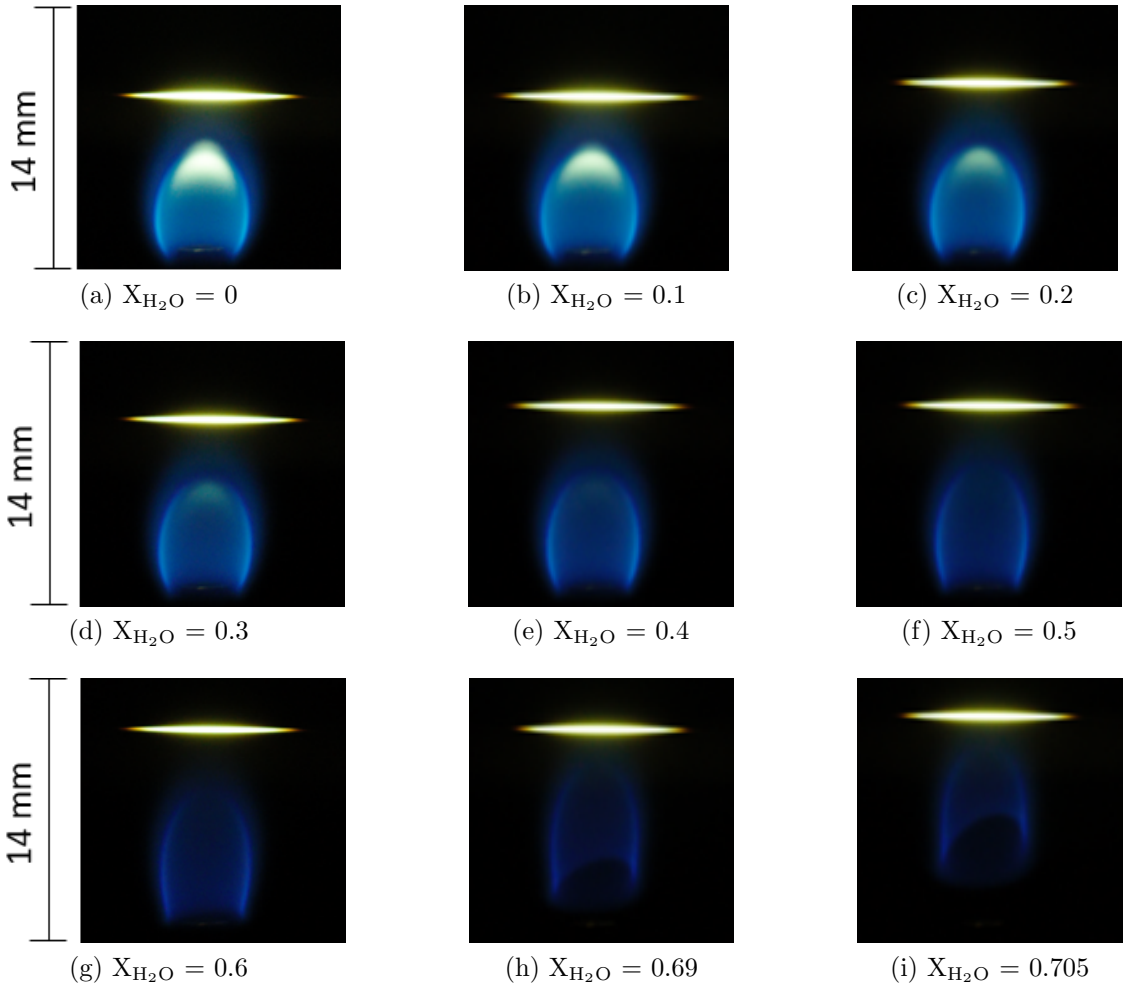

(a) $X_{H_2O} = 0$ (b) $X_{H_2O} = 0.1$ (c) $X_{H_2O} = 0.2$

(d) $X_{H_2O} = 0.3$ (e) $X_{H_2O} = 0.4$ (f) $X_{H_2O} = 0.5$

(g) $X_{H_2O} = 0.6$ (h) $X_{H_2O} = 0.69$ (i) $X_{H_2O} = 0.705$

Figure 3.1: Water dilution at constant CH_4 flow rate.

3.2 Temperature measurements

Sections 3.2.1 and 3.2.2 report the TFP results for the water diluted flame, and for methane dilution with Ar, N_2, or CO_2. Temperature profiles are mapped after positioning the SiC fiber horizontally in the flame at different heights. For each dilution condition, the fiber is first placed 0.25 mm above the burner tip, and then raised upward by 0.7 mm for each photograph. Figure 3.3 shows a typical TFP image of a flame with zero water dilution, which corresponds to the case of largest amount of soot present. It is clear that the flame, and the soot signal, is not visible, thus not affecting the temperature measurements. Moreover,

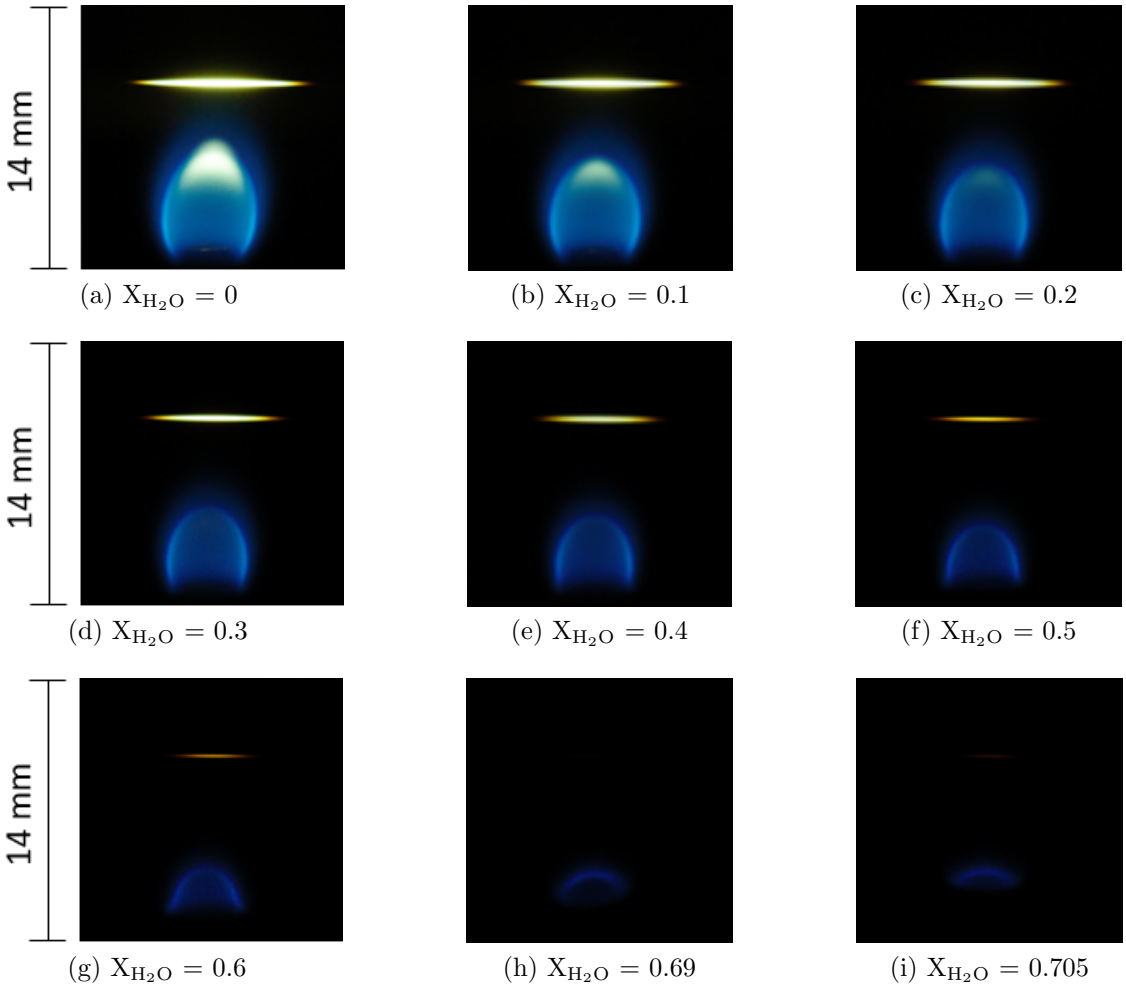

(a) $X_{H_2O} = 0$ (b) $X_{H_2O} = 0.1$ (c) $X_{H_2O} = 0.2$

(d) $X_{H_2O} = 0.3$ (e) $X_{H_2O} = 0.4$ (f) $X_{H_2O} = 0.5$

(g) $X_{H_2O} = 0.6$ (h) $X_{H_2O} = 0.69$ (i) $X_{H_2O} = 0.705$

Figure 3.2: Water dilution at constant total mass flow rate.

during processing, a background image of the flame is subtracted to further assure a pure fiber response.

Figure 3.4 (a) shows an example of pyrometry temperature measurements at one dilution condition, before radiation correction. Figure 3.4 (b) shows the corrected temperatures in the same flame. Each line in the plots correspond to one fiber height above the burner tip. Depending on the experimental condition, photographs of twelve to twenty fiber heights are captured. Those temperature profiles, along the fiber, are then used to create the flame temperature contours reported in the next section.

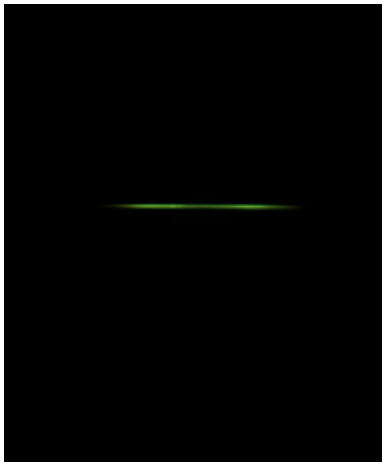

Figure 3.3: Typical TFP image (flame with no water dilution).

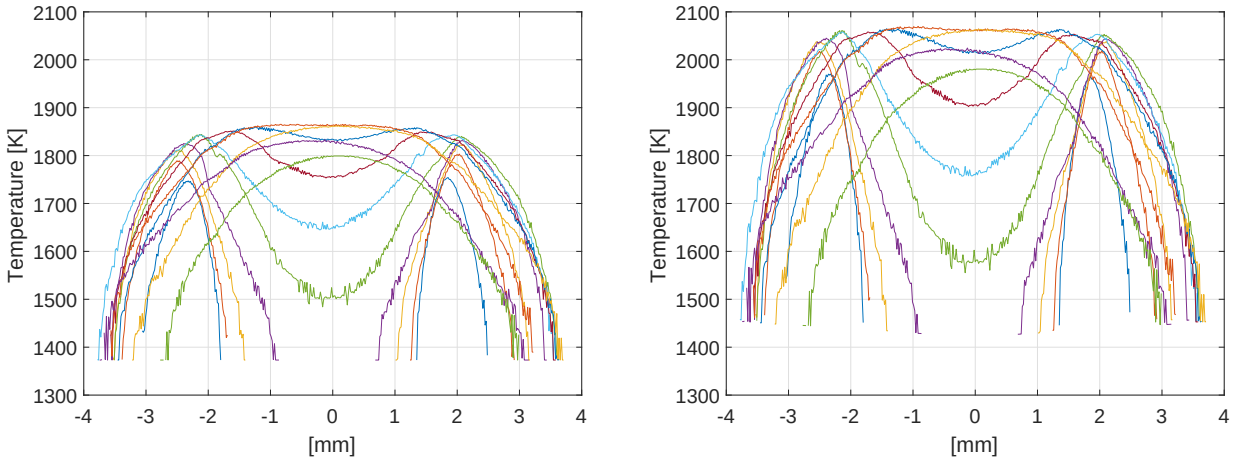

Figure 3.4: Example of temperature profiles (each line corresponding to an axial location in the flame): (a) fiber temperature; (b) gas temperature.

3.2.1 Water diluted flames

Figures 3.6 and 3.7 show the contour plots of the radiation corrected temperature profiles obtained at different levels of water dilution in the two inlet fuel flow conditions. The uneven lateral profile of the flame, in some of the images, is due to small movements of the flame between TFP photographs. Results in Figure 3.6 are obtained keeping the methane flow rate constant at 35 mL/min (at ambient temperature). The average fuel velocity at the exit

of the burner (at 510 K) is 39.9 cm/s at zero water mole fraction, and it increases as more water is added to the flow. The experiments of Figure 3.7 were run at constant total mass flow rate for the methane-water mixture, which is nearly equivalent to a constant momentum of the fuel jet. The air coflow was kept at a velocity of 46 cm/s at the burner exit in all the experiments. In both fuel flow rate conditions, the flame was able to sustain 0.705 mole fraction of water. A further minor increase in the diluent mole fraction of less than 0.01 resulted in flame extinction via a blowoff process, where the lifted flame started to oscillate and then extinguished.

In the case of increasing total mass flow rate, as the fuel inlet velocity increases, the flame stretches and becomes taller as it is driven by the momentum of the fuel jet. As the dilution level increases, the reaction zone moves downstream and the flame becomes clearly lifted from the fuel tip between 0.5 and 0.6 water mole fraction. Above 0.6 water mole fraction, small increases in the dilution level result in larger lifting of the flame as the extinction limit is approached.

A similar behavior can be seen in Figure 3.7. In this case, as more water is added to the fuel, less methane is introduced in the flame and the reaction zone shrinks. The temperature of the flame at extinction is lower than in the case of increasing mass flow rate at the same water content. The smaller, lower momentum, flame experiences higher heat loss by diffusion per unit heat release. The lower temperature could also be related to incomplete oxidation of CO into CO_2 caused by the relatively higher disruption from the coflowing air when the fuel jet momentum is lower. In the condition of constant total mass flow rate and lower fuel velocity, the flame can be sustained at a lower temperature, as shown in Figure 3.5 which reports the peak temperatures. This result is similar to what has been seen in counterflow flame results where water-diluted lower strained flames can be sustained at lower temperatures [36]. There is speculation that the reason for the ability of water-diluted flames to sustain themselves at lower temperature is related to the expected increase in OH radical in these flames. That assertion is one of the topics being evaluated in this study.

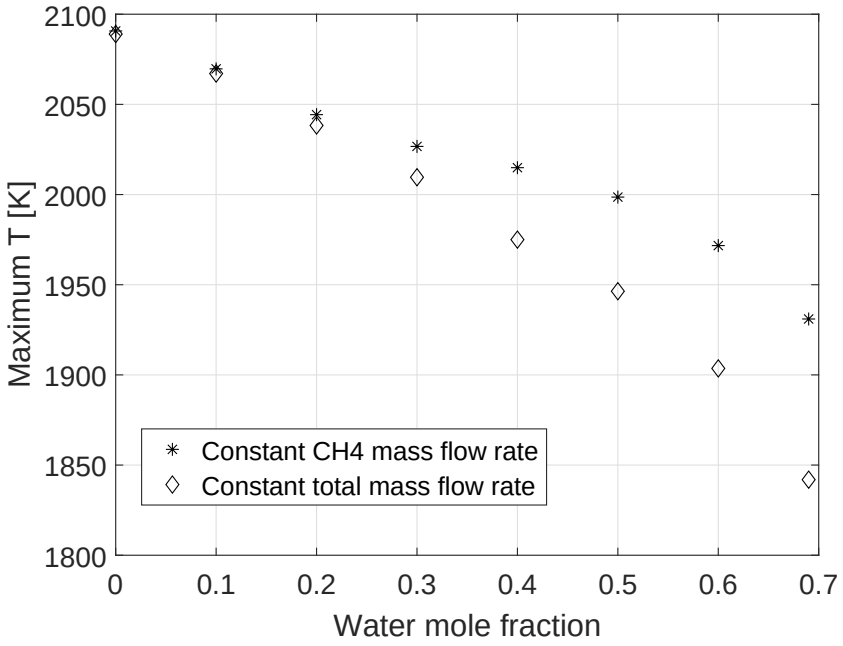

Figure 3.5: Experimental peak temperatures.

3.2.2 Ar, N_2, and CO_2 diluted flames

Experiments were also run with Ar, N_2, and CO_2 as diluents and the trends in maximum flame temperature were compared. The amounts of dilution with Ar, N_2, or CO_2 were such that the heat capacity rate (defined as the molar specific heat c_p multiplied by the molar flow rate) of the diluents added was always equal to the corresponding water case. Figure 3.8 shows the raw maximum temperatures (these data were not corrected for radiation) for the four different diluents. The x-axis is the water mole fraction at which the heat capacity rate was kept constant for the other three diluents. Figure 3.9 shows the same temperature results, but in this case the x-axis represents the actual mole fraction of each diluent. For diluents with lower heat capacities, a larger mole fraction of gas needs to be added to the methane flow than for higher c_p diluents. This means that for the same thermal absorptive loading, the velocity of the fuel mixture at the flame inlet is larger for gases with lower molar c_p. For the gases considered: Ar has the lowest c_p (20.8 J/molK at 510 K), followed by N_2 (29.7 J/molK), H_2O (35.3 J/molK) and CO_2 (44.9 J/molK). Figure 3.8 shows that temperatures

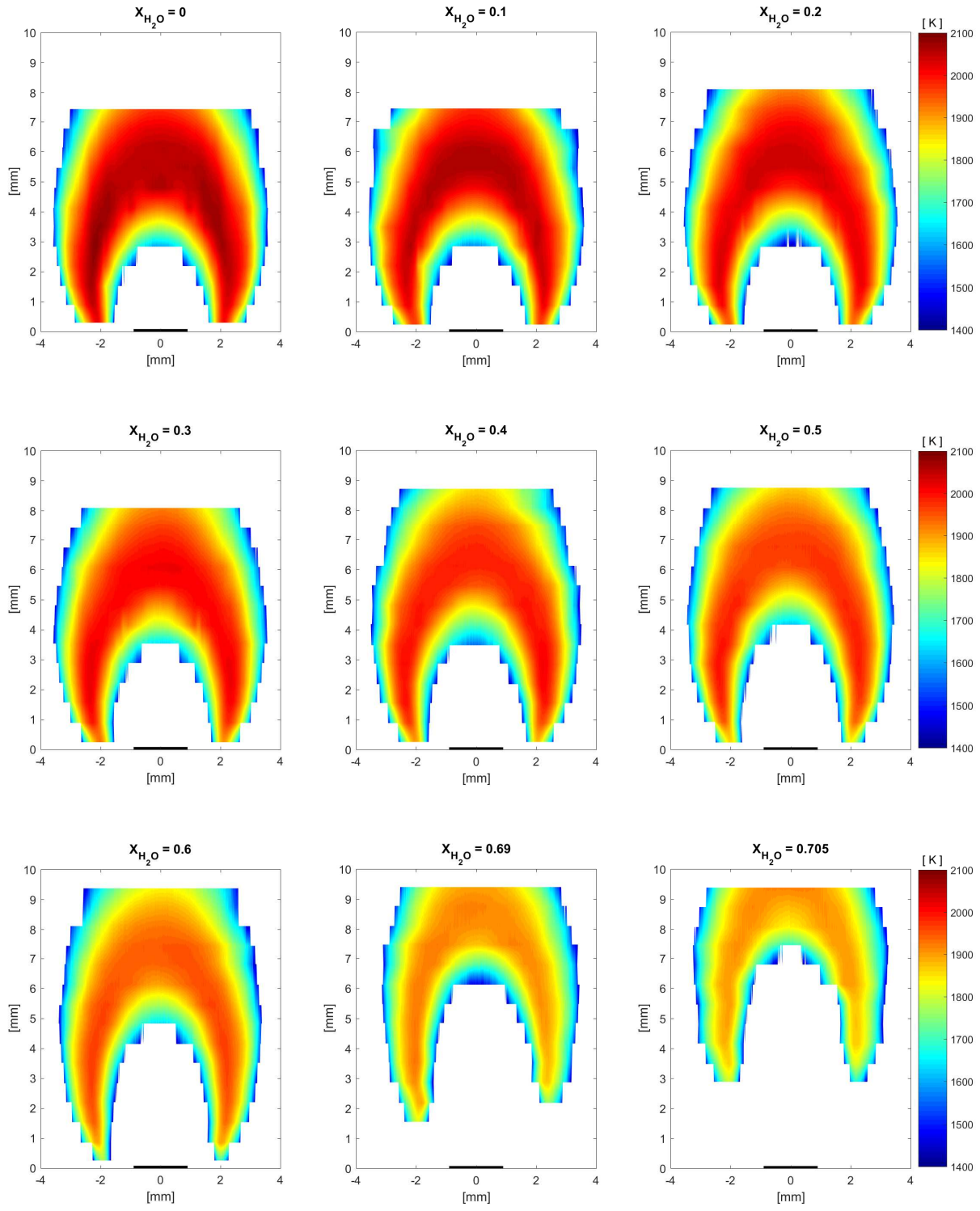

Figure 3.6: Temperature contours of the water diluted constant methane flow rate flame.

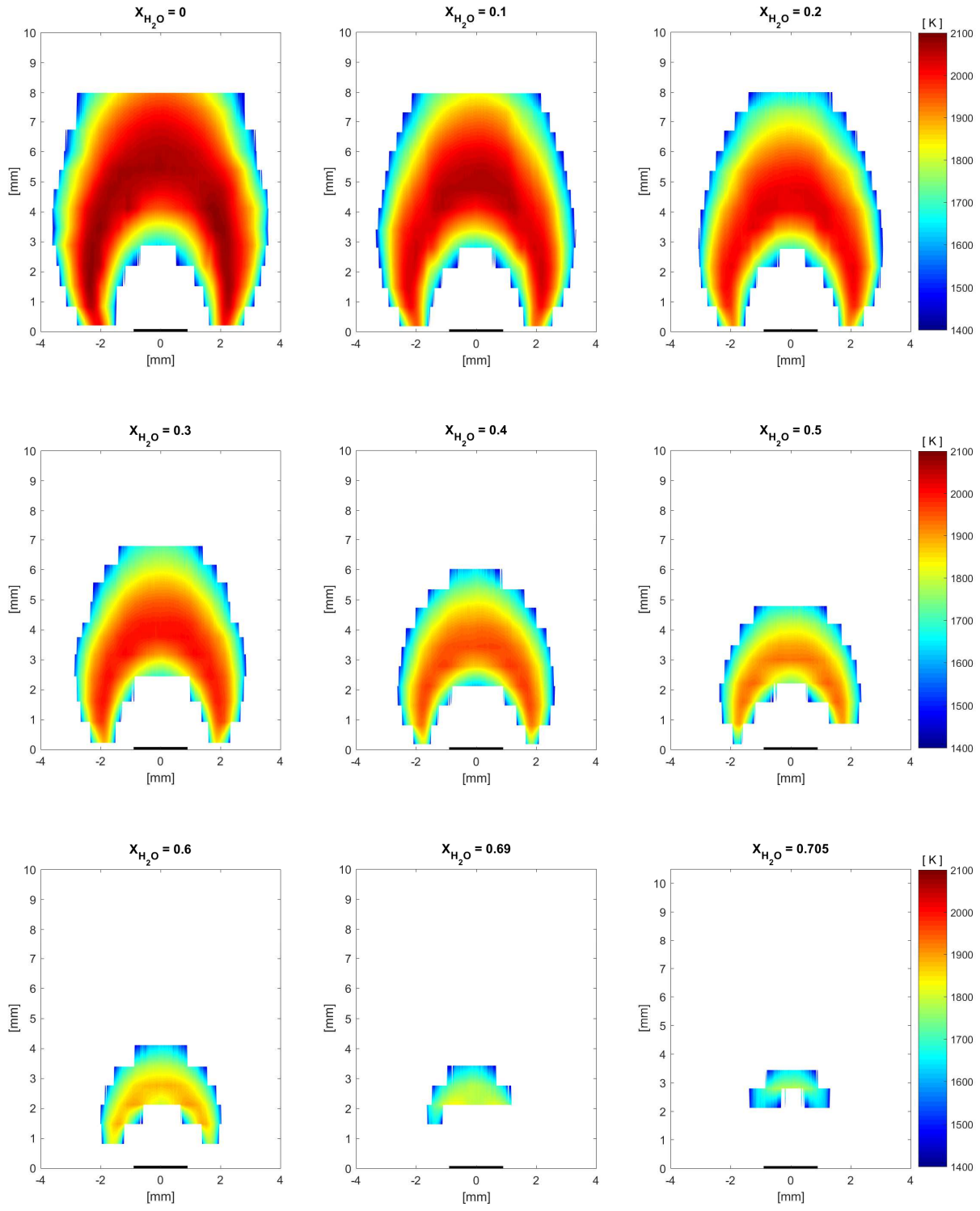

Figure 3.7: Temperature contours of the water diluted constant total mass flow rate flame.

and extinction limits are similar between different diluents when compared in terms of heat capacity rate. The water diluted flame extinguished between X_{H_2O} of 0.705 and 0.715. The CO_2 flame extinguished between the equivalent water mole fractions of 0.695 and 0.705. The N_2 diluted flames extinguished between heat capacity rates equivalent to water mole fractions of 0.705 and 0.71. In the case of Ar dilution, the flame extinguished slightly earlier, between the equivalent water mole fractions of 0.68 and 0.685. From Figure 3.9 it is possible to observe that near extinction the flame temperatures are lower for diluents with reduced inlet fuel velocities. This is consistent with the results obtained for the cooler water diluted flame subjected to lower strain fields. Those temperatures were not corrected for radiation, however calculations in pure N_2, or CO_2 at a temperature of 2100 K were carried out and showed that radiation corrections would not differ more than 30 K between water, N_2, or CO_2, which is below the 50 K uncertainties in the measurements. These temperature results show that chemical effects are minor as regards the thermal structure of the flame and the limits of extinction, but this result needs to be confirmed against possible counterbalancing chemical effects. Note that since all diluted flames sustain themselves at lower temperatures, the concept of specific radical species playing a role is unlikely. Figures 3.8 and 3.9 show a slight increase in temperature for low levels of dilution. Being the uncertainties of the TFP measurements in the order of 50 K, it is not possible to conclude that this increase is physical. Moreover, the temperatures reported in those plots have not been corrected for radiation heat losses. As dilution increases and the gas velocity increases, the radiation corrections become smaller. However, a similar behavior was also seen in counterflow experiments with water addition [36], thus it would be of interest to investigate more deeply the role of dilution in this region. Raw temperature contour plots of the flames discussed in this section can be found in Appendix B.

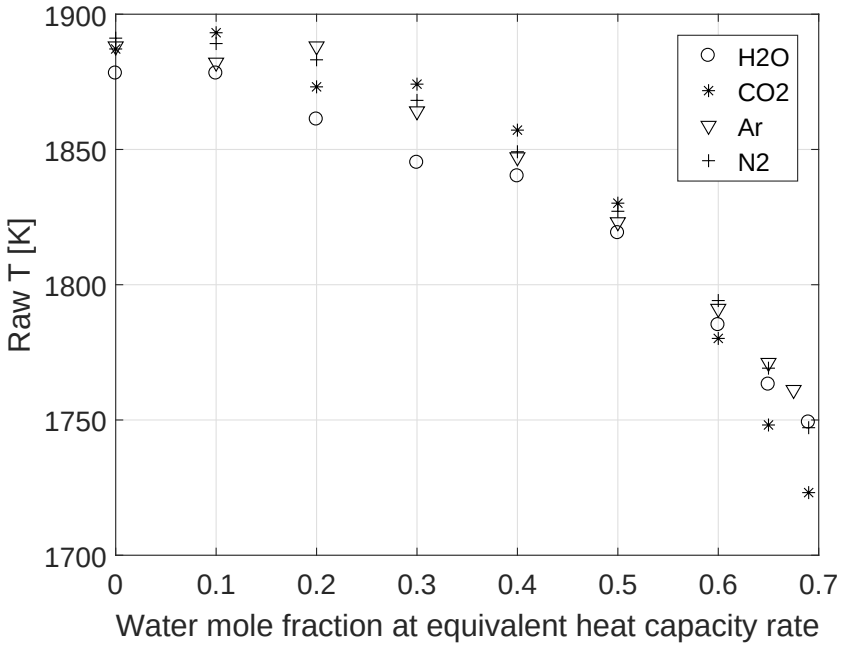

Figure 3.8: Experimental raw peak temperatures for H_2O, Ar, N_2, and CO_2 diluted flames vs equivalent heat capacity rate.

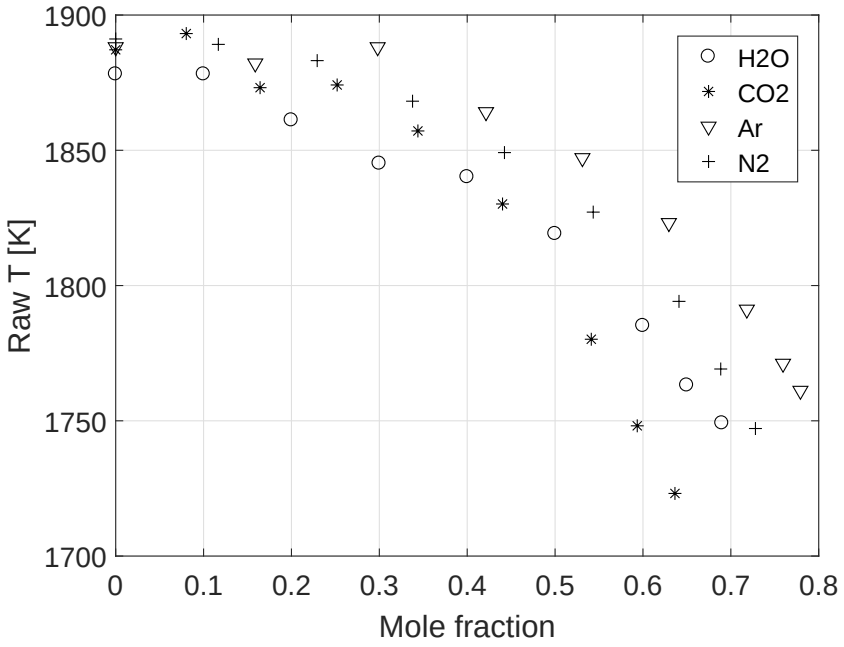

Figure 3.9: Experimental raw peak temperatures for H_2O, Ar, N_2, and CO_2 diluted flames vs mole fraction.

3.3 OH* and CH* chemiluminescence measurements

In Figures 3.10 and 3.11 the Abel inverted images of the chemiluminescence from the flame are reported, in black, over the measured temperature contours for the two fuel flow conditions tested. For water mole fractions up to 0.3 in the case of constant methane flow rate, and up to 0.2 in the constant total mass flow rate case, the soot incandescence signal contribution at the flame tip is also captured by the photographs, and it is clearly visible in the deconvoluted images. The Abel inversion was performed using the three-point deconvolution technique, as in [49]. The deconvolution technique suffers from singularities in the symmetry axis; this causes the noise in the center of the figures. As more water is added to the flame, the flame dims and the deconvolution becomes noisier. The temperature profiles are scaled on the peak temperature of each dilution condition, so it is possible to see how the reaction zone is positioned with respect to the maximum temperature region in each image.

Figures 3.12 and 3.13 show the OH* chemiluminescence images of the water and of the CO_2 diluted flames. The images are not shown on the same intensity scale, as the high diluted flames would be too dim to be visible if directly compared to the scales of the non-diluted cases. Some differences between the two diluents can be appreciated looking at those images. When CO_2 is added to the fuel stream, the flame stretches more than in the water case. According to the model developed by Roper [51], the flame height is inversely proportional to the diffusivity of the gases in the flame region. The lower diffusivity of CO_2 in air than water explains the larger height of the carbon dioxide flame. The other difference between the two dilution cases is the lift-off height of the flame just before extinction happens. The lift-off of the flames when diluted with 0.69 water mole fraction or the equivalent amount of CO_2 are similar. However, the CO_2 diluted flame blows off with a small increase of diluent. On the other end, the water diluted flame lifts significantly more before extinction happens.

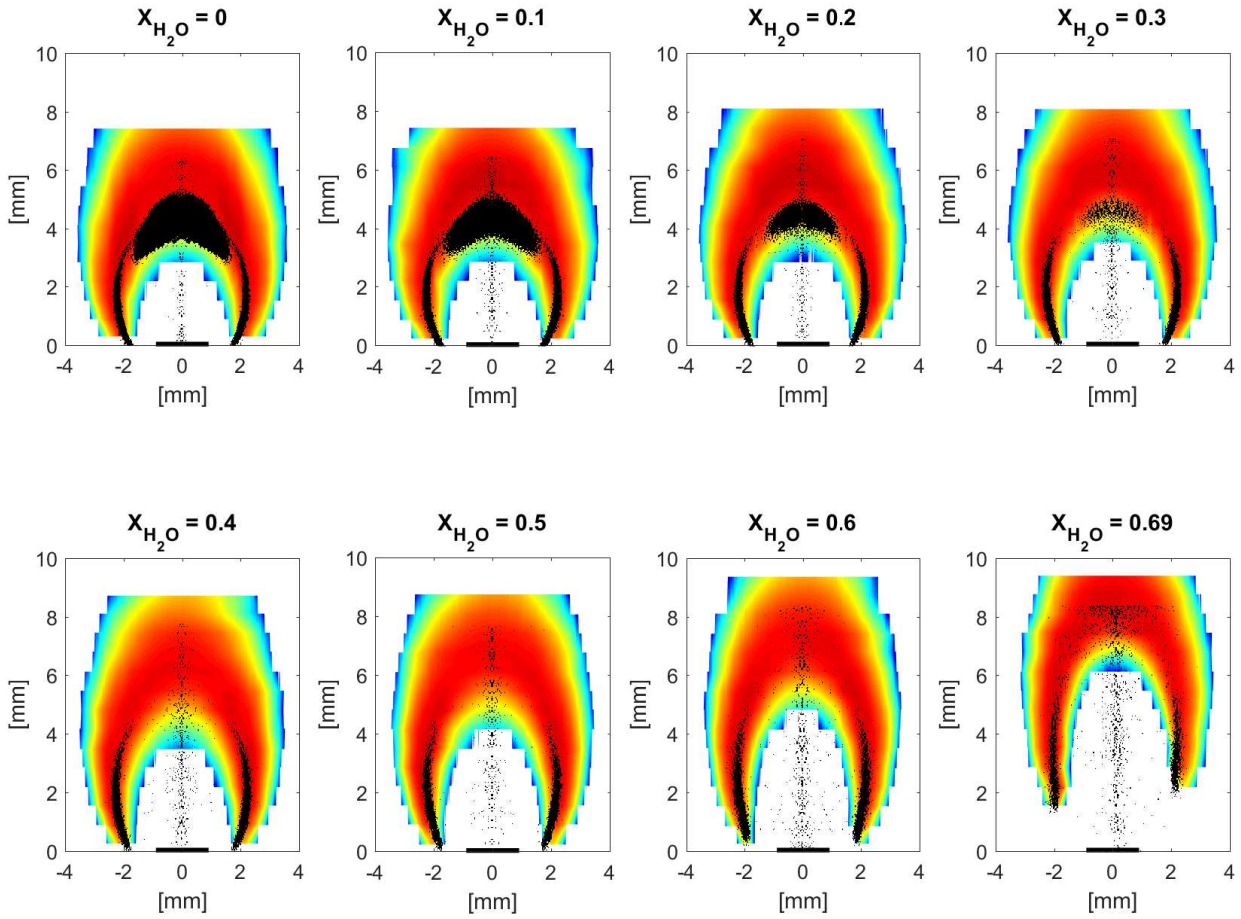

Figure 3.10: Abel inverted images and temperature contours of the water diluted constant methane flow rate flame.

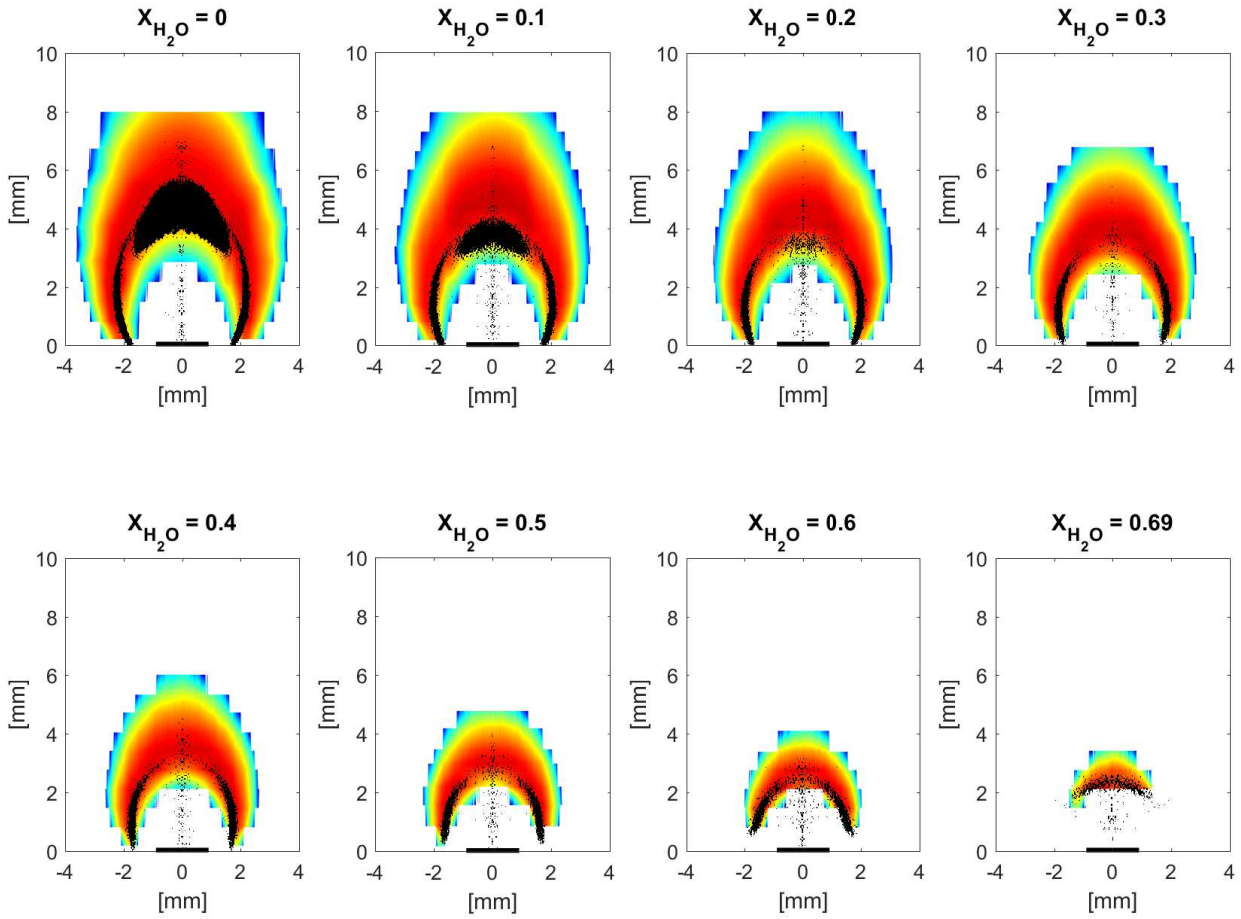

Figure 3.11: Abel inverted images and temperature contours of the water diluted constant total mass flow rate flame.

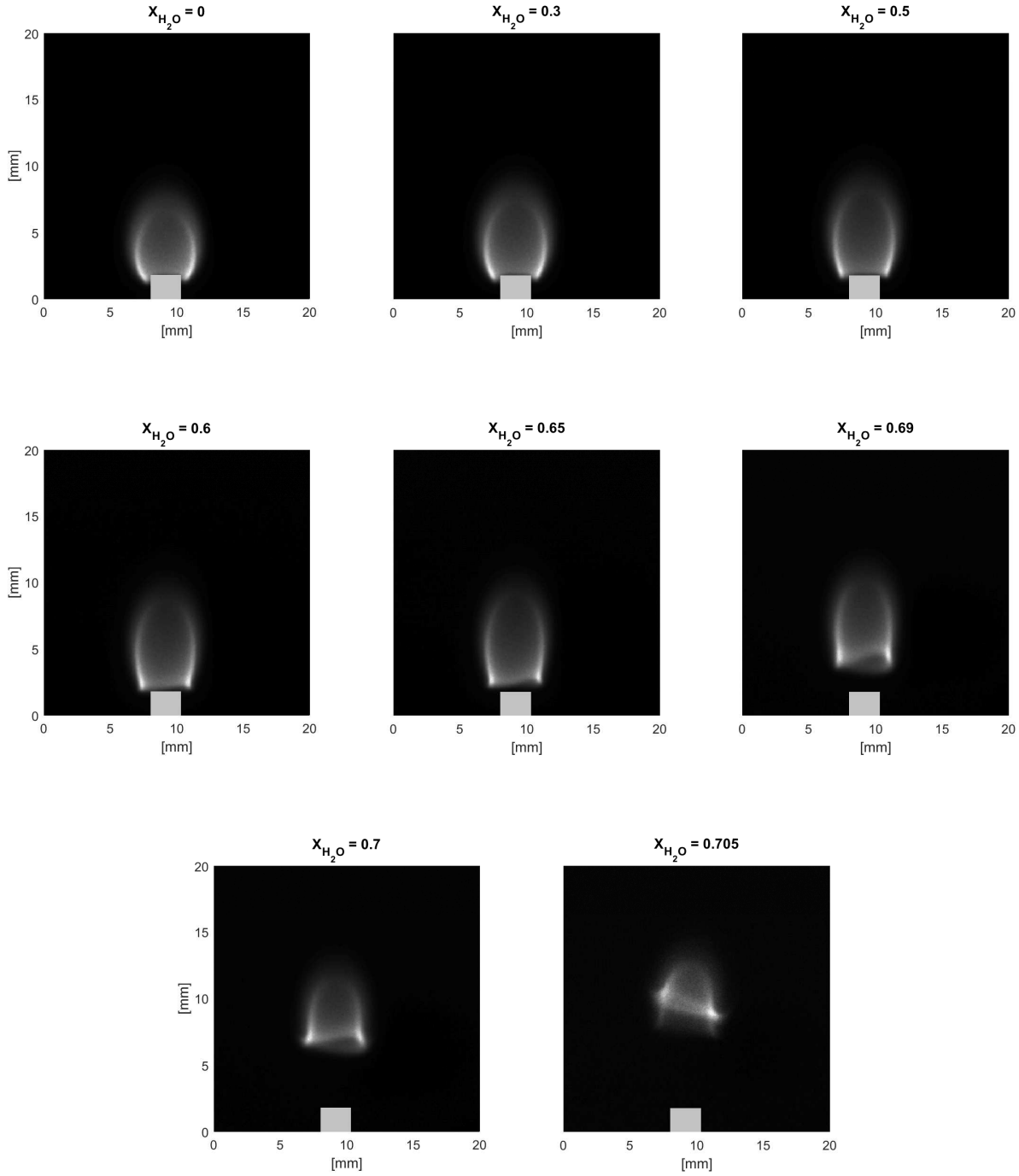

Figure 3.12: OH chemiluminescence images of the H_2O diluted flames.

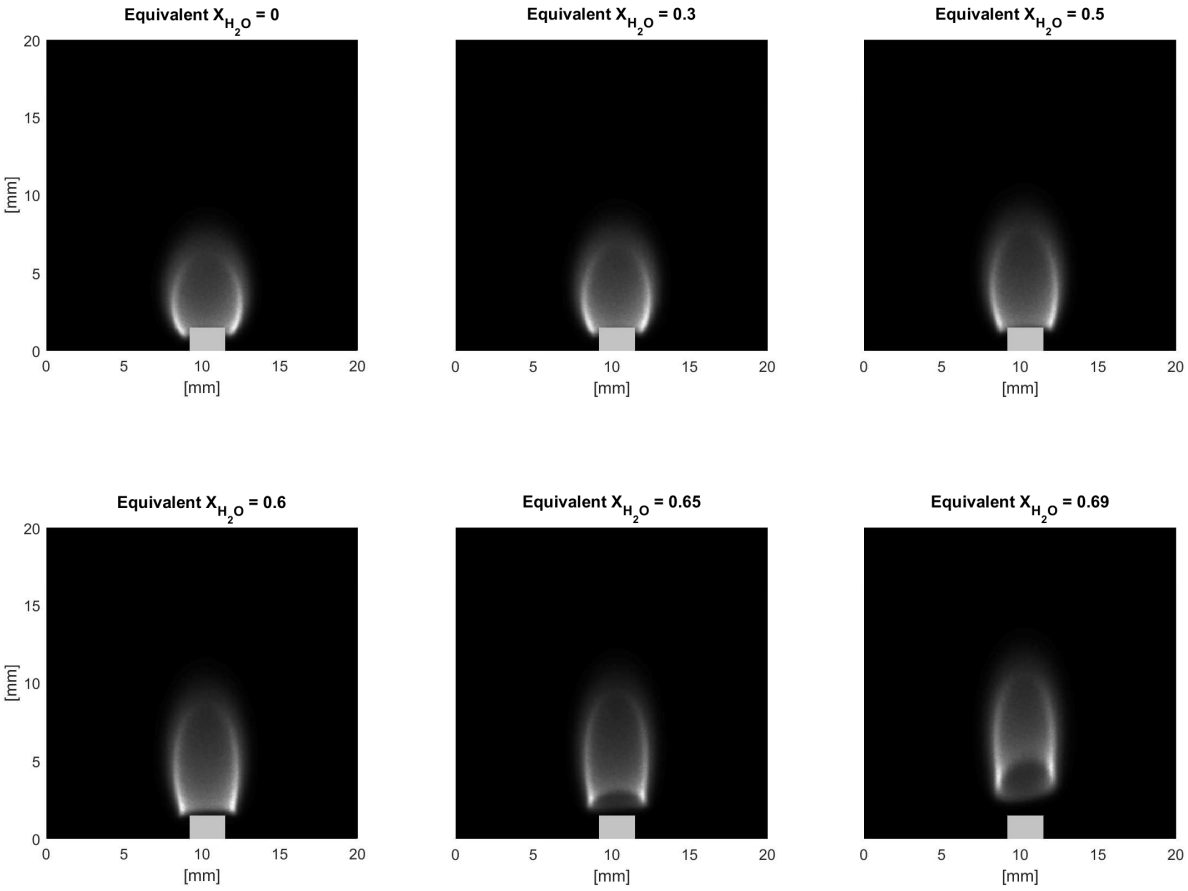

Figure 3.13: OH chemiluminescence images of the CO_2 diluted flames.

3.4 OH fluorescence measurements

OH PLIF was performed in water diluted, and in CO_2 diluted flames. The condition used, with both diluents, was the constant methane flow rate one. Two conditions of air coflow velocity were tested. One set of experiments was run at constant air coflow velocity, to match the TFP experiments presented in the previous section. A second case was also run, for both water and CO_2, where the air coflow velocity was always matched to the fuel velocity. Figures 3.14 and 3.15 show the OH images of the water and CO_2 diluted flame with constant air velocity. Images for the experiments where the air coflow velocity was matched to the fuel velocity at each dilution levels can be found in Appendix C. The reason for the asymmetry in the flame edges is due to the presence of the fuel tip blocking the laser light. For the case in Figure 3.14, the laser is shooting through the flame from the left side, the flame edge is completely visible on the left side, but the fuel tip blocks the laser (and thus OH fluorescence) on the right side of the flame. As in the TFP measurements, the heat capacity rate was kept constant with respect to the water case when testing the carbon dioxide dilution flames. As discussed earlier, the CO_2 diluted flame extinguishes at a similar heat capacity rate of water: between 0.695 and 0.705 water mole fraction at equivalent heat rate for the constant air velocity, and between 0.55 and 0.56 for the matched velocities case. It is possible to see that the water diluted flames lift higher above the burner just before extinction than the CO_2 diluted flames. This could be an effect of the difference in momentum of the fuel jet as the inlet velocity of the CO_2/methane mixture is lower than the water/methane one at the same heat capacity rate. Another explanation for this effect, which can be seen in both the conditions tested, can be related to a difference in the radical pool between the water and the CO_2 diluted flames. As it was shown in the previous section, different diluents result in comparable maximum flame temperature. However, being that both water and CO_2 are possibly active species in the reaction, their addition to the fuel stream can affect the concentrations of important radicals such as OH, O and H in different ways. This can result

in a stronger flame, in case of CO_2 dilution with respect to water addition, explaining the upstream positioning of the flame edge and the smaller lift-off height. These considerations will be further discussed in Section 5. Figure 3.16 shows a side-by-side comparison of the OH fluorescence images in the two dilution cases. As was discussed in previous sections, the flame shape between the two cases is different, especially as extinction is approached. The carbon dioxide diluted flame stretches more, while the lift-off height of the water diluted flame is larger. The CO_2 diluted flame, in fact, blows off with a small addition of diluent with respect to the 0.69 equivalent water mole fraction case while the water case lifts considerably with a 0.01 water mole fraction increase in the dilution concentration.

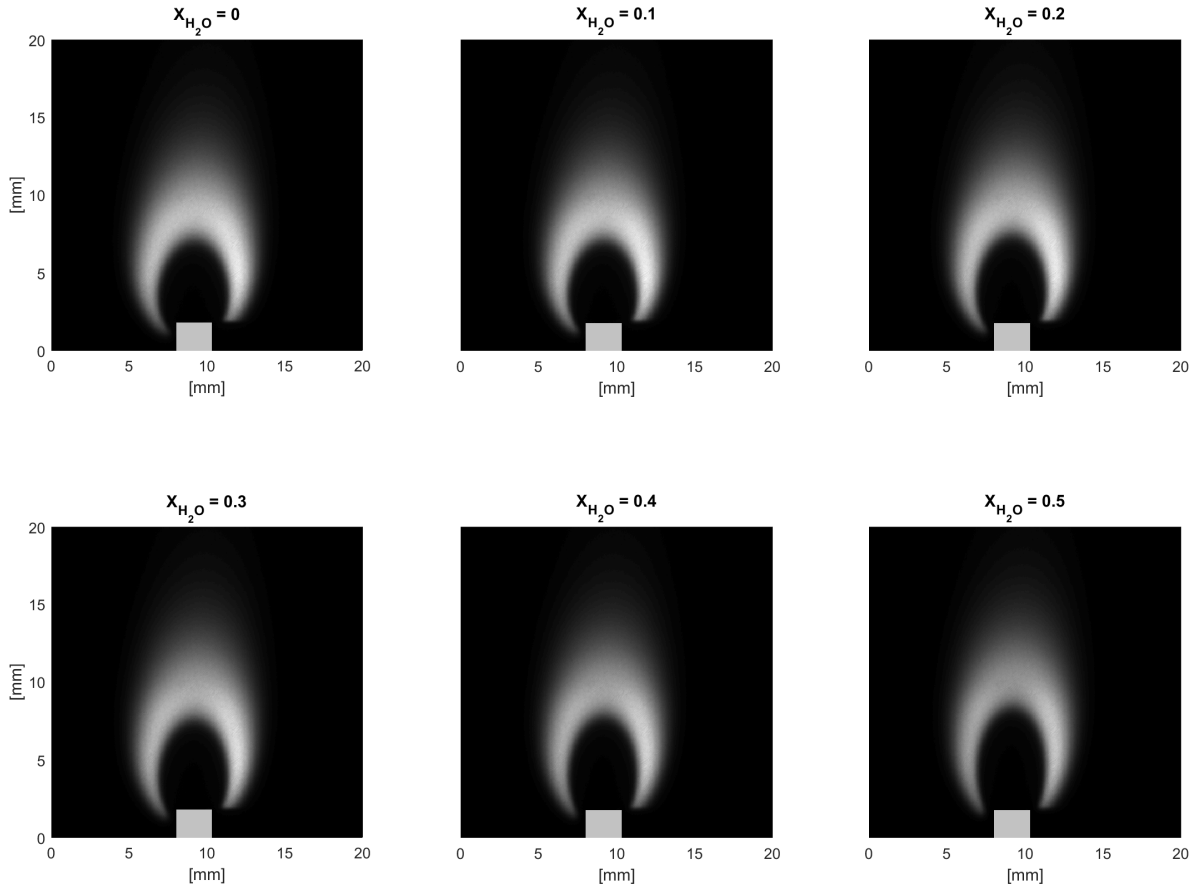

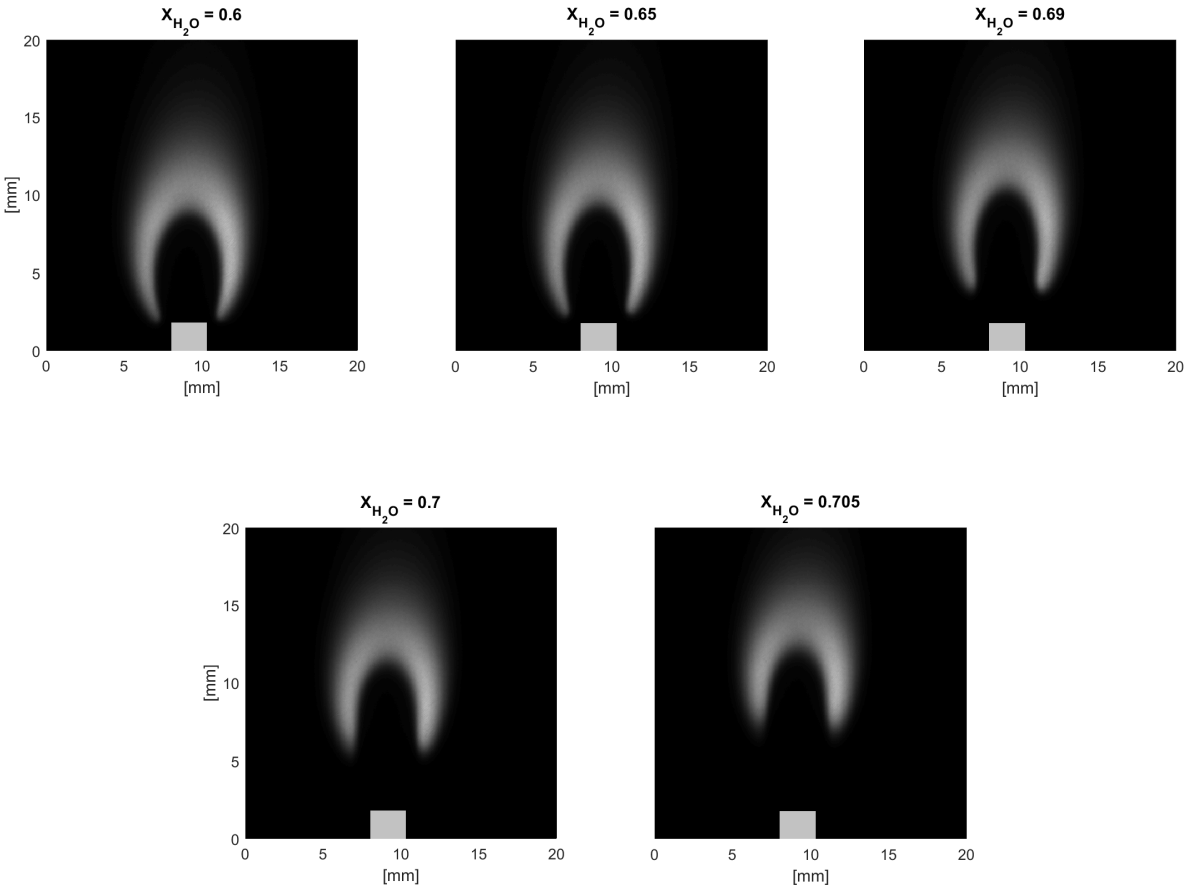

Figure 3.14: OH PLIF images of the water diluted flame, constant air coflow velocity.

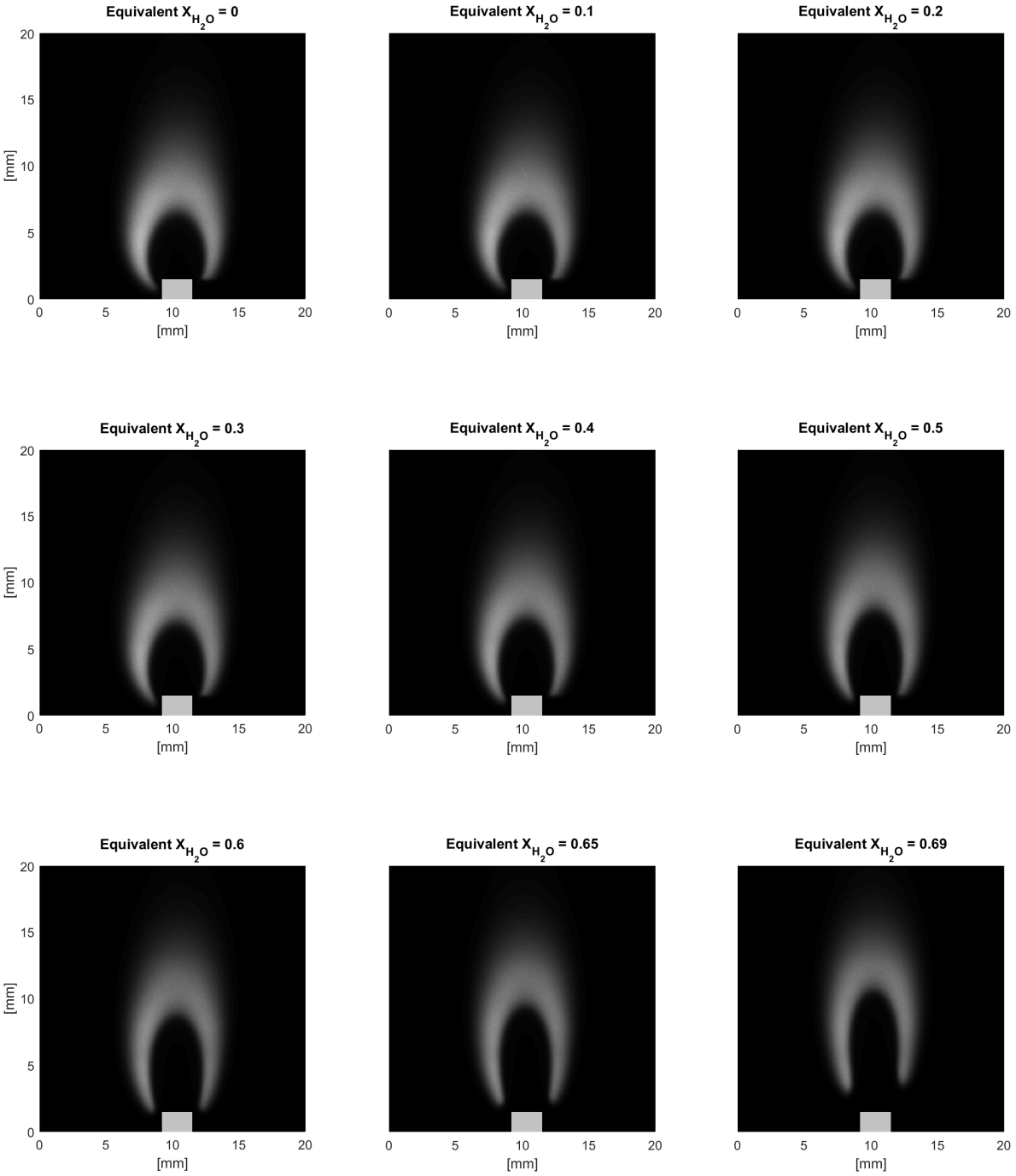

Figure 3.15: OH PLIF images of the CO_2 diluted flame, constant air coflow velocity.

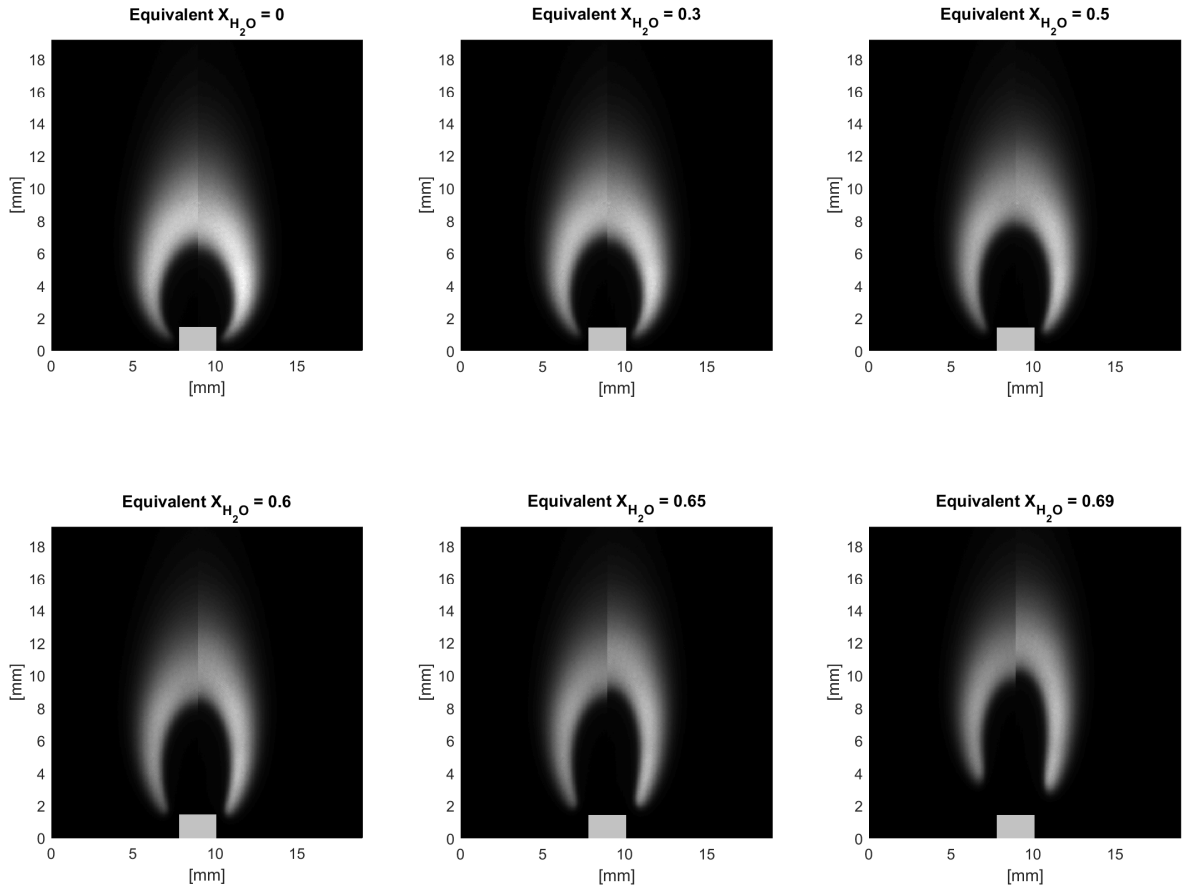

Figure 3.16: OH PLIF images at constant air coflow velocity: H_2O dilution on the left, CO_2 dilution on the right .

Figures 3.17 and 3.18 shows a comparison between integrated and peak OH signals obtained experimentally with PLIF for the H_2O and CO_2 flames. The plots also report the standard deviations around each condition tested. Standard deviations on the 1000 images taken in each experiment were always below 5% for the integrated OH signal, and around 10% for the peak signals.

For the water dilution case, the integrated results, normalized to unity at the zero-dilution condition, show three regions of interest. At low dilution levels, experiments show an increase in total OH signal. A region of linear decrease follows. Near extinction, a fast roll-off appears. However, it is important to point out that the fuel velocities at the exit of the fuel tube are not the same between H_2O and CO_2 diluted gases at the same condition of heat capacity rate. In fact, CO_2 has higher heat capacity at 510 K than water; a lower mole fraction of gas needs to be added to the methane flow to reach the same thermal absorptive loading resulting in a lower inlet fuel velocity. The pronounced roll-off of integrated OH could be the effect of the change in the flame shape. To avoid this, Figure 3.18 reports the results for peak OH, normalized with respect to the maximum pixel intensity at the zero water addition case. At low dilution levels, the water diluted case behaves differently than when diluting with CO_2, with an initial increase in peak OH, as observed before. Similarly to what was discussed for the temperature measurements, the increase is small with respect to uncertainties in the OH fluorescence measurements. However, a similar behavior was observed in counterflow experiments [36]. Moreover, as reported in Chapter 1, this increase in OH concentrations and temperature was also observed by [13] at low dilution levels. This behavior would be worth a more in depth analysis. As dilution increases, peak OH measurements become linear and become comparable close to extinction. However, since water is a better fluorescence quencher than CO_2, and being that temperatures are comparable near extinction, a correspondence in the PLIF signal hints at a larger amount of OH for the H_2O case. Since TFP results showed that temperatures at extinction for the two diluents considered here are comparable, this difference in OH concentration is not

purely a thermal effect. To compare quantitatively the effects of the two diluents, simulated fluorescence was performed and it is described in the following chapter.

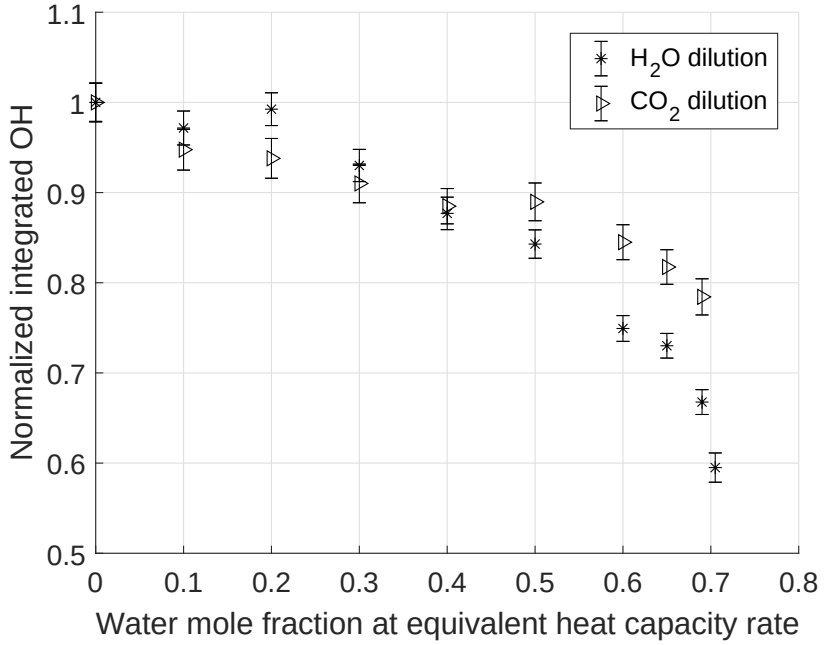

Figure 3.17: Experimenal integrated OH results for H_2O and CO_2 diluted flames.

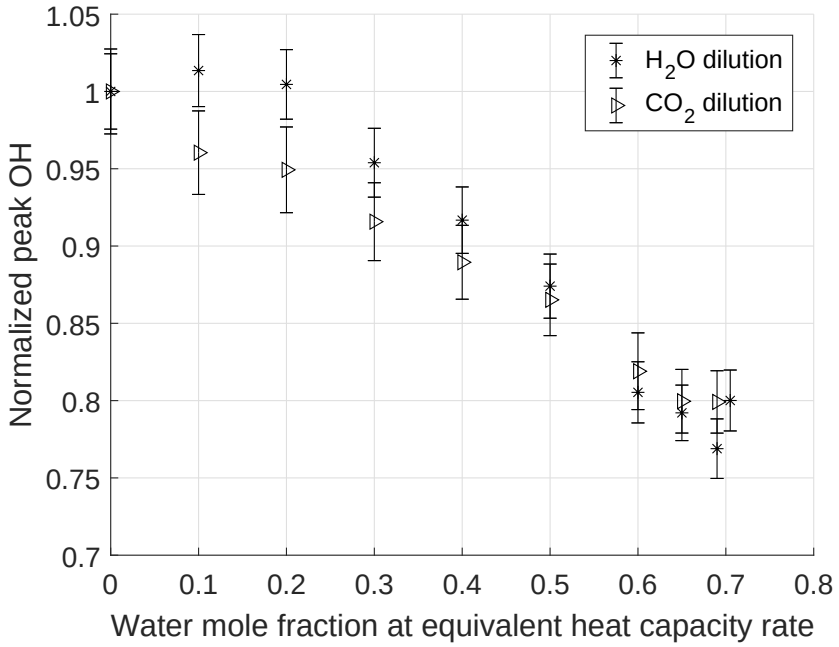

Figure 3.18: Experimenal peak OH results for H_2O and CO_2 diluted flames.

Integrated OH results for the cases of air coflow velocity matched to the fuel velocity can be found in Appendix C. These velocity matched results vary in the details but do not provide any different physical insight as regards the differing level of OH between water diluted and CO_2 diluted flames.

OH PLIF measurements were also performed for H_2O and CO_2 dilution by keeping the adiabatic flame temperature constant. To do so, H_2O or CO_2 was substituted to N_2 in the fuel line. Results of those experiments are reported in Appendix C.

Chapter 4

Numerical model

Numerical computations of the diluted coflow diffusion flame are useful to provide a comparison with the experimental measurements, perform radiation corrections for TFP, to quantify the local quenching species and obtain a quantitative measure of OH, and to study other physical and chemical effects of the diluent in the flame behavior. Initially, simulations were carried out with OpenFOAM [52]. Later, the software used to obtain numerical results was changed to PeleLM [53]. Additional details on the OpenFOAM simulations and the reasons for the change in the numerical tool can be found in Appendix D.

The PeleLM combustion software is an open-source software developed at Lawrence Berkeley National Laboratory for chemically reacting low Mach number flows [54, 55]. The code solves the reacting Navier-Stokes equations in the low Mach number regime, where the characteristic fluid velocity is small compared to the sound speed, and the effect of acoustic wave propagation is unimportant to the overall dynamics of the system. Accordingly, acoustic wave propagation can be mathematically removed from the equations of motion, allowing for an increase in the allowable time step over an explicit, fully compressible method.

4.1 Governing equations

The conservation equations in the low Mach number regime, and assuming a mixture-average diffusion model are the following:

$$\frac{\partial(\rho \boldsymbol{u})}{\partial t} + \nabla \cdot (\rho \boldsymbol{u}\boldsymbol{u} + \tau) = -\nabla \pi + \rho \boldsymbol{F} \tag{4.1}$$

$$\frac{\partial(\rho Y_i)}{\partial t} + \nabla \cdot (\rho Y_i \boldsymbol{u} + \boldsymbol{\mathcal{F}_i}) = \rho \dot{\omega}_i \tag{4.2}$$

$$\frac{\partial(\rho h)}{\partial t} + \nabla \cdot (\rho h \boldsymbol{u} + \boldsymbol{\mathcal{Q}}) = 0 \tag{4.3}$$

with:

$$\boldsymbol{\mathcal{F}_i} = -\rho D_{i,m} \nabla Y_i \tag{4.4}$$

$$\tau_{i,j} = \frac{2}{3}\mu \delta_{i,j} \frac{\partial u_k}{\partial x_k} - \mu \left(\frac{\partial u_i}{\partial x_j} + \frac{\partial u_j}{\partial x_i} \right) \tag{4.5}$$

$$\boldsymbol{\mathcal{Q}} = \sum_i h_i \boldsymbol{\mathcal{F}_i} - \lambda \nabla T \tag{4.6}$$

where ρ is the density, $\boldsymbol{u}$ is the velocity, τ is the stress tensor, π is the perturbational pressure field, $\boldsymbol{F}$ is the external forcing term. Y_i is the mass fraction of species i, $\boldsymbol{\mathcal{F}_i}$ is diffusion flux for species i, $\dot{\omega}_i$ is the molar production rate for species i. h is the enthalpy of the gas mixture and $\boldsymbol{\mathcal{Q}}$ is the heat flux. μ is the shear viscosity, $\delta_{i,j}$ is the Dirach delta function, λ is the conductivity, and T is temperature. $D_{i,m}$ are the mixture-averaged diffusion coefficients:

$$D_{i,m} = \frac{\sum_{j \neq i} Y_j}{\sum_{j \neq i} X_j / D_{ij}} \tag{4.7}$$

where X_i is the mole fraction of species i, and D_{ij} are the binary diffusion coefficients of species pairs i, j. The conductivity λ is calculated with the following empirical mixture

formula:

$$\lambda = \frac{1}{2}\left(\frac{1}{\sum_i \frac{X_i}{\lambda_i}} + \sum_i X_i \lambda_i\right) \tag{4.8}$$

A chemistry model involving N_s species interacting through a set of M_r elementary reaction steps, can be written as:

$$\sum_{i=1}^{N_s} \nu'_{i,r}\,[X_i] \rightleftharpoons \sum_{i=1}^{N_s} \nu''_{i,r}\,[X_i] \qquad \text{for} \quad r \ni [1, M_r] \tag{4.9}$$

where $[X_i]$ is the molar concentration of species i. $\nu'_{i,r}$ and $\nu''_{i,r}$ are the stoichiometric coefficients on the reactant and product sides of reaction r, associated with species i. The molar production rate $\dot{\omega}_i$ is calculated as follows:

$$\dot{\omega}_i = \sum_{r=1}^{M_r} \nu_{i,r} R_r \tag{4.10}$$

with $\nu_{i,r} = \nu''_{i,r} - \nu'_{i,r}$. The rate of reaction R_r can be expressed in terms of the forward and backward rate coefficients $k_{f,r}$ and $k_{b,r}$:

$$R_r = k_{f,r} \prod_{i=1}^{N_s} [X_i]^{v'_{i,r}} - k_{b,r} \prod_{i=1}^{N_s} [X_i]^{v''_{i,r}} \tag{4.11}$$

The reaction rate coefficients $k_{f,r}$ and $k_{b,r}$ are calculated using the Chemkin modified Arrhenius reaction format:

$$k_f = A T^{\beta} e^{-\frac{E_a}{RT}} \tag{4.12}$$

where A is the pre-exponential factor, β is the temperature exponent, E_a is the activation energy, and R is the universal gas constant. The balance of forward and backwards rates are

governed by equilibrium thermodynamics through the equilibrium constant Kc, r. In low Mach regime Kc, r is a function only of temperature and thermodynamic properties of the reactants in reaction r.

$$k_{b,r} = \frac{k_{f,r}}{Kc, r} \tag{4.13}$$

with:

$$Kc, r = e^{\left(\frac{\Delta S_r^0}{R} - \frac{\Delta H_r^0}{RT}\right)} \left(\frac{p_0}{RT}\right)^{\sum_{i=1}^{N_s} \nu_{i,r}} \tag{4.14}$$

where ΔS_r^0 and ΔH_r^0 are the change in enthalpy and entropy of the reaction r, and p_0 is the ambient pressure. The thermodynamic properties are modeled assuming a mixture of ideal gases. Species enthalpies, entropies ans molar heat capacities are calculated with polynomial fits, as functions only of temperature.

It is not the aim of this work to discuss the details of the numerical approach, however it is important to point out some of the main features of PeleLM. One of these, is the use of a multi-implicit spectral deferred correction method (MISDC) to provide coupling between advection, diffusion, and reactions during treatment of conservation of mass and energy. More specifically, at each time step the integrator iteratively evaluates reactions (R), advection (A), and diffusion (D) with coupling between each other: R is computed with a source term formed using previous iterates of D and R. Similarly, D uses iterated approximations of A and R, and R uses approximations of A and D. When this is taken to convergence, each time step is computed with an implicit method that couples R, D and A. This method allows for the code to take large time steps with good accuracy, even with coarse grids, avoiding numerical extinction of the flame.

4.2 Coflow flame simulation details

The flame is simulated using a 10 x 40 mm mesh in cylindrical coordinates with a 64 x 256 coarse grid. PeleLM uses adaptive mesh refinement (AMR) to regrid the mesh, creating increasingly finer grids embedded in the coarser grids until the solution is sufficiently resolved. An error estimation procedure, based on user-specified criteria, evaluates where additional refinement is needed. In this work two levels of refinement above the coarse grid are used. Figure 4.1 shows an example of the temperature profile for a typical flame simulated with two levels of adaptive refinement, the images are cut vertically at the 20 mm location. The initial coarse mesh, with 64 x 256 grids, has spatial resolution of about 156 μm (Figure 4.1 (a)). The first regridding step is based on a temperature gradient criteria. All grids with temperature gradients larger than 50 K are tagged to be spatially halved in both directions, resulting in a final resolution, in the regridded area, of about 78 μm. Figure 4.1 (b) shows the first refinement level, the red box in the image show the refined areas. The second refinement criteria is set the same temperature gradient as in the first refinement, with the addition of an additional criteria on OH mass fractions greater than 0.002. The resolution in this area becomes of about 39 μm (Figure 4.1 (c)). The total number of grids obtained after two levels of refinement depends on the flame shape and properties, and is different for each case run. However, as an example, the number of grids in the case reported in Figure 4.1 can be calculated. The initial mesh has 64x256, or 16384, grids. In the first refinement step, the 40x64 grids area in the red box in Figure 4.1 (b) is refined and becomes an area of 80x128 grids. Thus, after the first level of AMR, the total number of grids is 24064. Out of those, 13824 have a 156 μm resolution, while the rest have a 78 μm resolution. After the second AMR step, the total number of grids become 36352. Figure 4.2 shows the OH profile of the flame, with the two levels of ARM. ARM allows to obtain a finer mesh only where a better resolution is needed, avoiding longer computation times associated with an overall fine mesh.

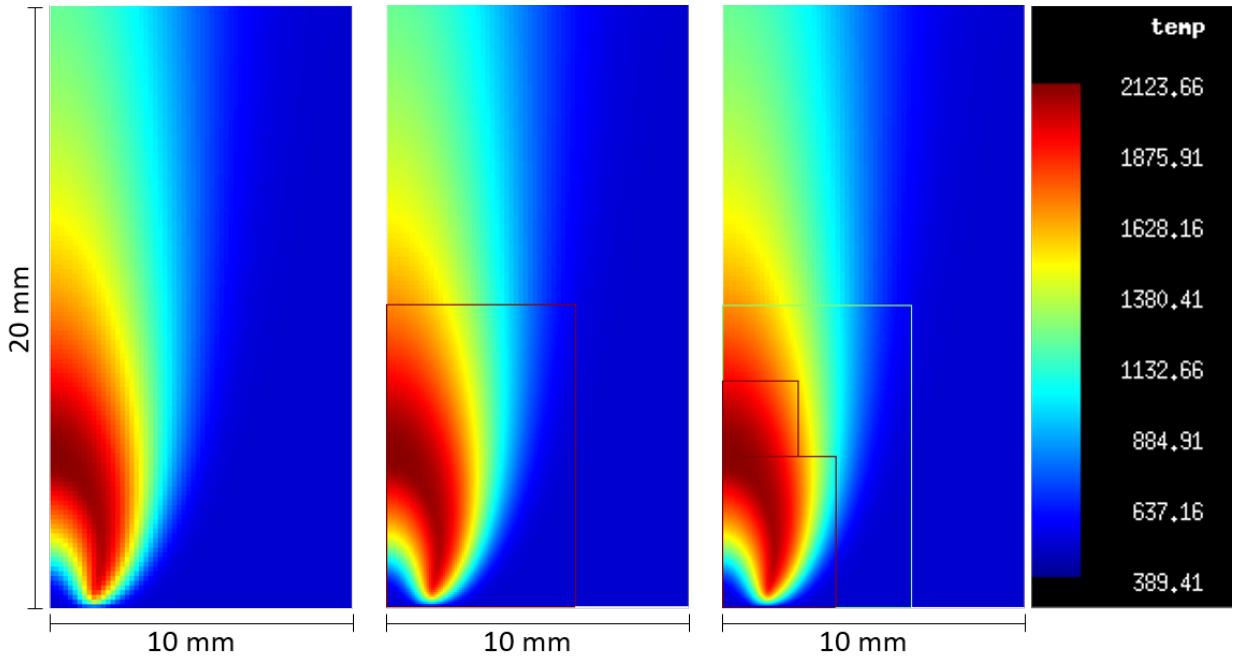

(a) (b) (c)

Figure 4.1: Temperature profile with two levels of AMR: (a) coarse grid; (b) first refinement on temperature criteria; (c) second refinement on temperature and OH mass fraction criteria.

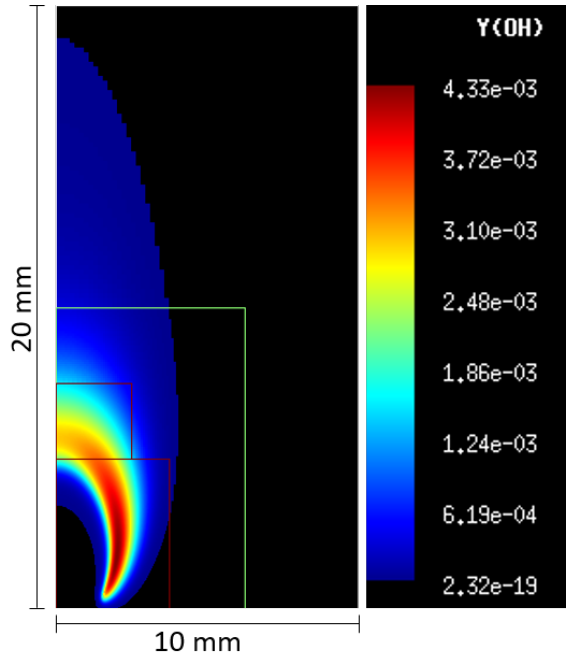

Figure 4.2: OH numerical profile with two levels of AMR.

Boundary conditions are set on the four sides of the computational domain. Referring to the images in Figure 4.1, the left side is the flame axis is set as the flame axis of symmetry. The right side is defined as a slip wall, where the normal velocity is always zero, and the gradient of temperature across the boundary is also null. The top boundary is set as outflow, the values for velocities and temperature are calculated by the code with a first order extrapolation from the last cell in the interior of the domain. Pressure is set in the whole domain to be always constant and equal to ambient pressure. The bottom side is the inlet boundary, where the values for temperature and gas velocities are specified. The fuel enters the domain between the symmetry axis and the 0.9 mm horizontal location. The fuel inlet velocity has a parabolic profile, with average velocity matching the experimental conditions, and inlet temperature of 510 K. Moving horizontally from left to right, the fuel region is followed by a 0.2 mm region from which no gases enter the computational domain; this represents the fuel tube wall. The remaining part of the boundary is the air inlet. The air inlet temperature is fixed at 510 K, the air velocity profiles will be discussed in more details in Section 4.2.1.

The burner geometry in the simulations, does not account for the extruded fuel tip so that air and fuel streams both enter the computational domain at the zero vertical location. This can have an effect on the results at low water concentrations. Near extinction, the flame lifts from the burner which should reduce the effect from the geometry configuration. However, based on the results comparison shown later, the significance of the geometric difference between experiment and calculation may be the reason for significant differences in the simulated flame shapes with respect to the experimental one.

Results are obtained running the GRI-Mech 3.0 chemistry, consisting of 53 species and 325 elementary chemical reactions. Previous work on water addition to the methane stream of a counterflow diffusion flame compared results from the GRI-Mech 3.0 chemistry to results obtained using the methane mechanism developed at the National University of Ireland, Galway [56]. The mechanism consists of 118 different chemical species and 663 elementary

reactions. Padilla, et al. [17] report that the comparison between the two chemistry models shows similar predicted behaviors for major species, O, H and OH radicals, temperatures and other intermediate species.

Each numerical simulation is run up to steady state condition. The steady state condition is defined such that the relative errors of all species and major variables calculated by the code (i.e. horizontal and vertical velocities, temperature, density, etc..) between the predicted values at a certain time step, and 100 time steps later, is below 0.5 %. The relative error e_r is defined as:

$$e_r = \frac{||V_0 - V_{100}||}{||V_0||} \tag{4.15}$$

where V represents the predicted values of the variable of interest, V_{100} represents the results 100 time steps after V_0. As the code do not perform the calculation with a fixed time step, the progression in real time between 100 time steps is not fixed, it varies between about 1.5 ms and 3 ms.

4.2.1 Inlet gases velocity profiles

As mentioned above, the fuel inlet velocity profile is parabolic, with average speed matching the experimental fuel speed at each water dilution condition considered. The air velocity was initially set to be constant and equal to the experimental velocity of 46 cm/s, with a top hat profiles. The code implements a hyperbolic tangent velocity profile for the air stream, to avoid any singularities at the interface between the air and the fuel tube wall that would occur if a completely flat profile was to be used:

$$V_{air}(x) = V_0 \tanh\left(\frac{2(x - (x_f + x_{th}))}{C_{BL}}\right) \tag{4.16}$$

where V_0 maximum velocity at the right wall, x_f is the fuel tube radius, x_{th} is the fuel tube thickness, and C_{BL} is a constant selected by the user to define the thickness of the region of the velocity transitions from zero to V_0. Originally, the constant C_{BL} was set to 0.2 mm and V_0 was set to 46 cm/s to approximate the experimental top-hat velocity profile, as shown in Figure 4.3. Figure 4.4 shows a comparison between the simulated OH profile (right) and the experimental OH fluorescence images (left) with increasing dilution levels. As mentioned earlier, while the burner has an extruded fuel tip, the PeleLM simulations are run with fuel and air gases entering the domain at the zero vertical height. The images in Figure 4.4 are compared side by side by aligning the burner tip in the experimental images to the fuel inlet position of the numerical computational domain. It is clear from the images that while the flame shape and position is well predicted at low water concentrations, the flame lifts earlier and more abruptly in the numerical results than it does in the experiments. This can be related to the difference in geometries. The presence of the extruded burner tip possibly creates a region of mixing which helps the flame edge to remain attached closer to the burner. As the aim of the numerical work is to perform simulated fluorescence to quantify the effects of fluorescence quenching, it is important to obtain numerical results that predict well the flame shape and position.

The condition of 0.6 water mole fraction in the fuel stream, being the condition at which the difference in flame lift-off between experiments and simulations becomes significant, was selected to discuss the effect of the air velocity profile in the flame positioning. A good match between the experimental and numerical flame position is defined, in this work, as a similar vertical positioning of the maximum gradient of OH concentration on the flame symmetry axis. The vertical location of the maximum gradient was determined from the OH PLIF images and the difference between this value and the one found from the simulated flames was calculated. Figure 4.5 shows the location of the maximum gradients and the difference (Δ) for a typical flame.

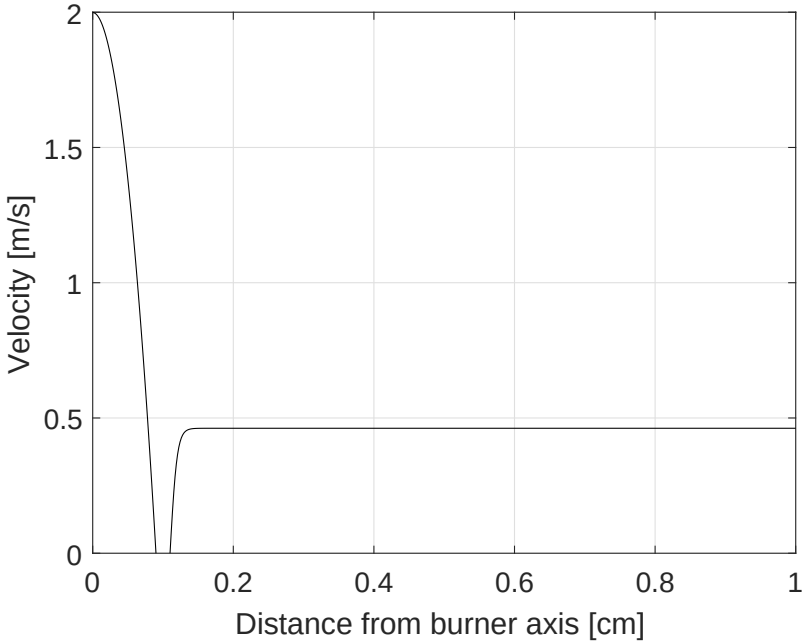

Figure 4.3: Fuel and air velocity profiles for the 0.6 water mole fraction case, with C_{BL} = 0.2 mm and V_0 = 46 cm/s.

The black stars in Figure 4.6 shows the difference between the vertical location on the flame axis of the maximum OH gradient between experimental PLIF images and numerical simulations, as a function of the boundary layer constant C_{BL} in the air velocity profile. The plot shows that the flame moves downward as the transition between zero air velocity and V_0 becomes smoother. However, as C_{BL} is increased while keeping V_0 fixed to 46 cm/s, the total mass of air introduced in the domain, and thus the average velocity of the air profile, decrease. To maintain the total mass flow rate of air constant, V_0 needs to increase with increasing C_{BL}. The hollow circle in Figure 4.6 refers to the case of C_{BL} = 0.3 mm and V_0 = 52 cm/s. In this condition, the average air velocity is then 46 cm/s.

Figure 4.7 shows the experimental vs numerical comparison of the OH profiles at increasing boundary layer constant C_{BL}. The bottom plots show the inlet gas velocity profile. The last images on the right represent the condition chosen as the best prediction of the flame shape at this water dilution level. All the cases were then run with the new air velocity profile.

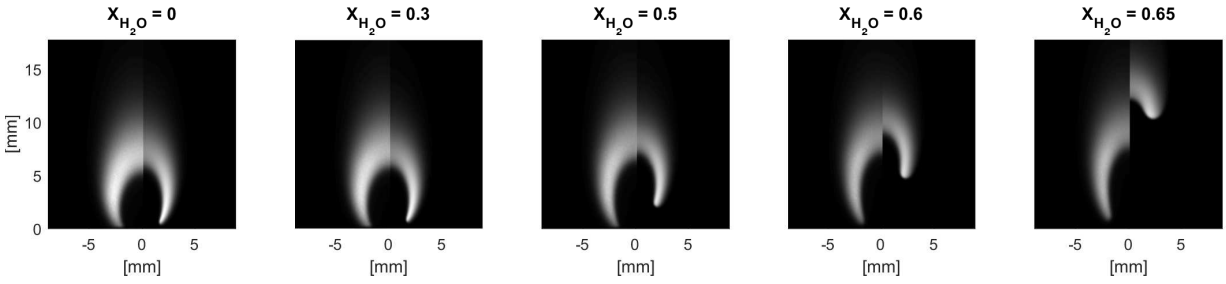

(a)

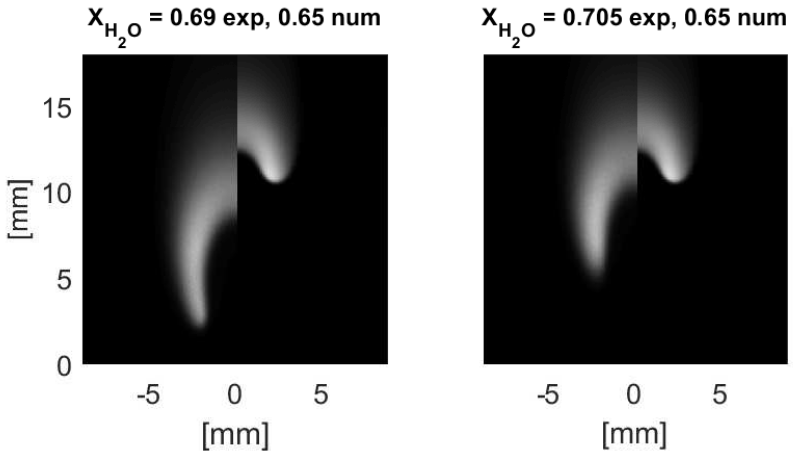

(b)

Figure 4.4: Experimental OH fluorescence (left) vs numerical OH concentration (right) profiles at increasing water concentrations: (a) water dilution from 0 to 0.65 mole fractions; (b) 0.65 water mole fraction in the numerical results compared to higher water concentrations for the experimental images.

Figure 4.8 shows the OH profile comparison at different dilution levels. The images show that while the flame shape is in good agreement at 0.6 water mole fraction, at higher dilution levels the simulated flames still lift significantly more than in the experiments.

The same procedure used to find the new velocity profile for the case of 0.6 water mole fraction, was followed for the cases with higher water dilution. Figure 4.9 shows the difference between the vertical location on the flame axis of the maximum OH gradient between experimental OH PLIF images and numerical simulations at 0.65 mole fraction of water in the fuel stream, as a function of increasing boundary layer constant C_{BL}. At each condition,

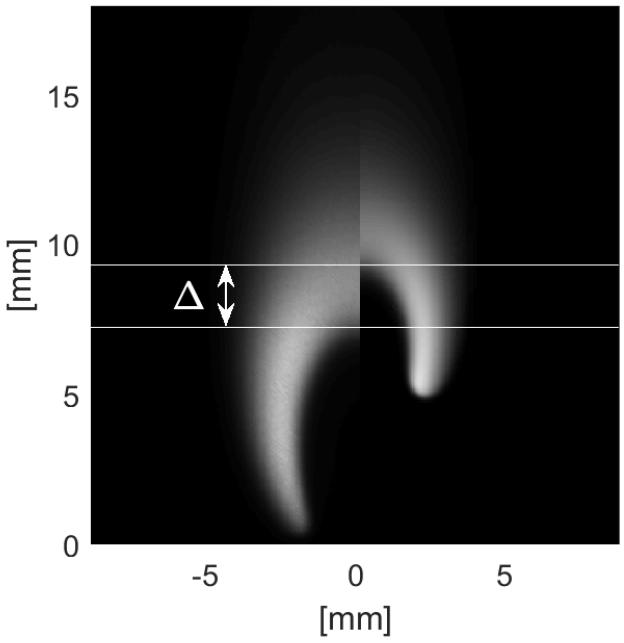

Figure 4.5: Difference Δ between the location of the maximum gradient on the OH profile along the flame axis in the experimental images and the numerical OH profiles for a typical flame.

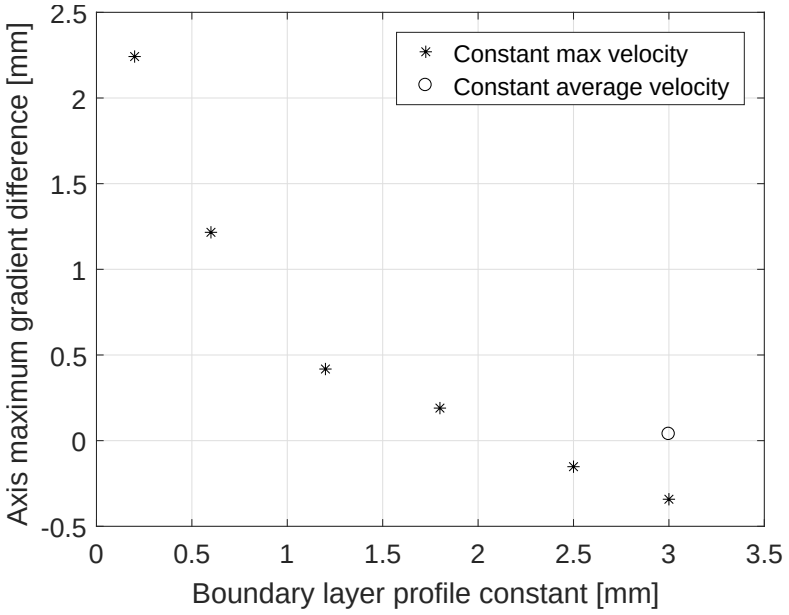

Figure 4.6: Difference between the vertical location on the flame axis of the maximum OH gradient between experimental OH PLIF images and numerical simulations at 0.6 mole fraction of water in the fuel stream, as a function of the boundary layer constant C_{BL}.

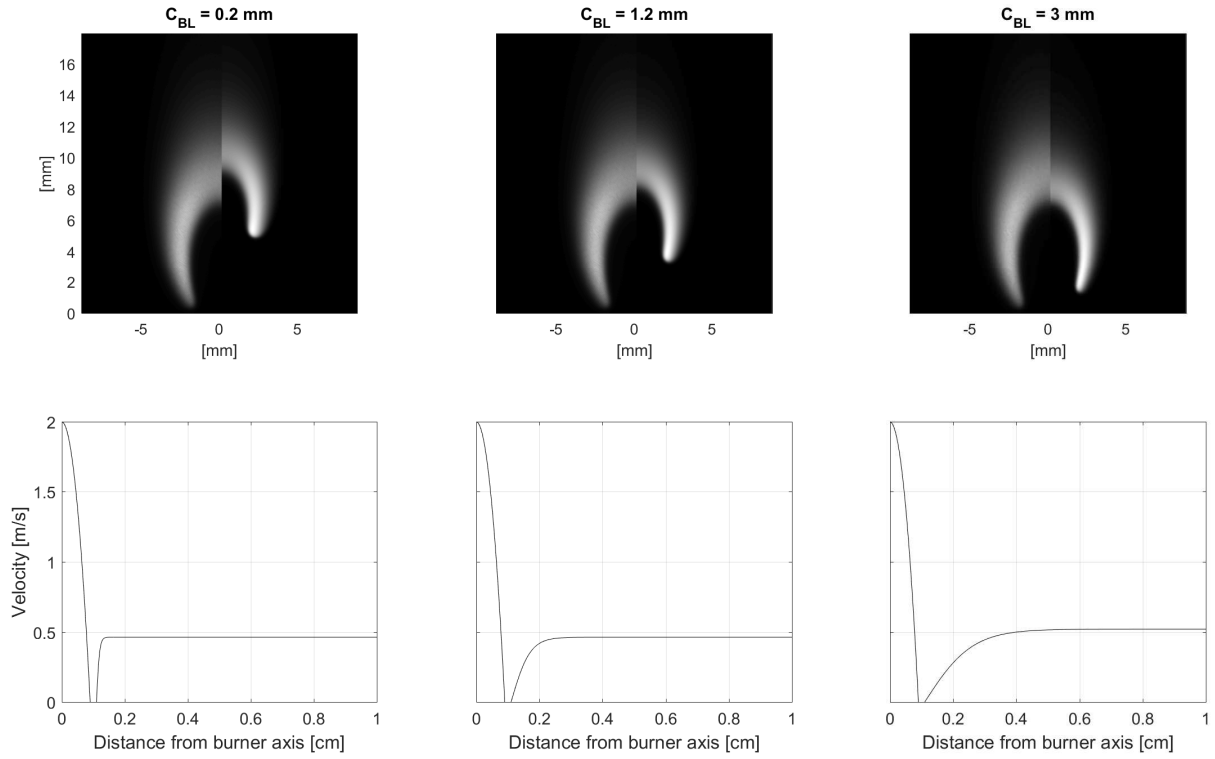

Figure 4.7: Top: Experimental OH PLIF images (left) vs numerical OH simulations of the 0.6 water mole fraction diluted flame at increasing values for C_{BL}. Bottom: corresponding inlet gases velocity profiles.

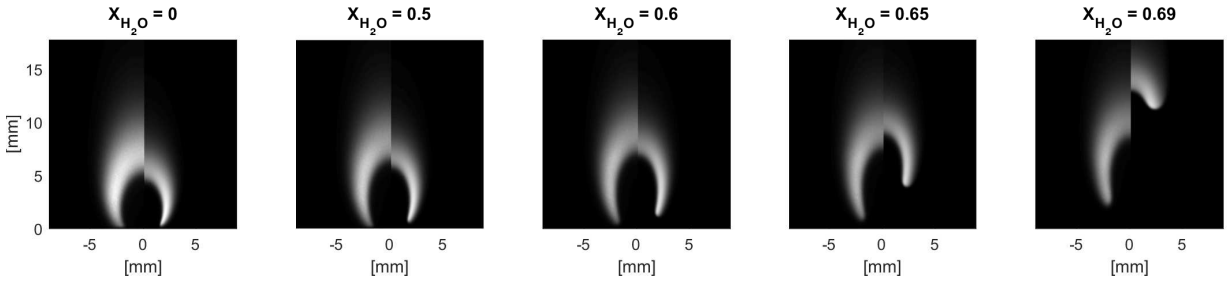

Figure 4.8: Experimental OH PLIF images (left) vs numerical OH simulations of the 0.6 water mole fraction diluted flame with $C_{BL} = 0.3$ mm and $V_0 = 52$ cm/s.

the value for V_0 was adjusted so that the average air velocity remained constant at 46 cm/s. However, extrapolating from the data shown in the plot it is possible to see that to reach zero maximum gradient difference, the value of C_{BL} would need to be raised to values similar or greater than the horizontal dimension of the computational domain. For this reason, the value C_{BL} was increased from 0.3 mm to 0.55 mm, keeping $V_0 = 52$ cm/s. Doing so, the average velocity of the air profiles decreases, but the simulations predict well the flame

shape, as can be seen in Figure 4.10. The same was also done for the case of 0.69 water mole fraction in the fuel stream. Figure 4.10 shows the final OH profiles used to study the flame in the following sections.

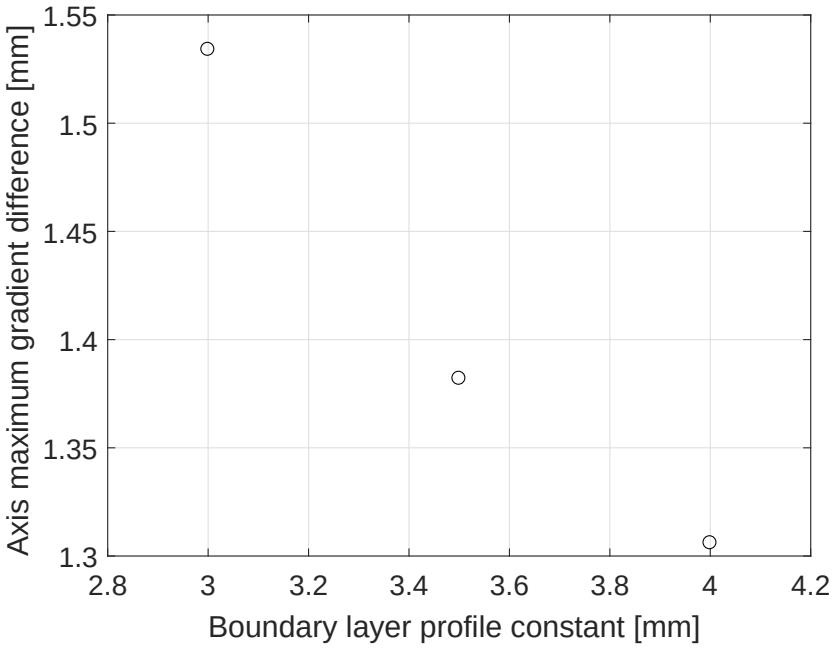

Figure 4.9: Difference between the vertical location on the flame axis of the maximum OH gradient between experimental OH PLIF images and numerical simulations at 0.65 mole fraction of water in the fuel stream, as a function of the boundary layer constant C_{BL}.

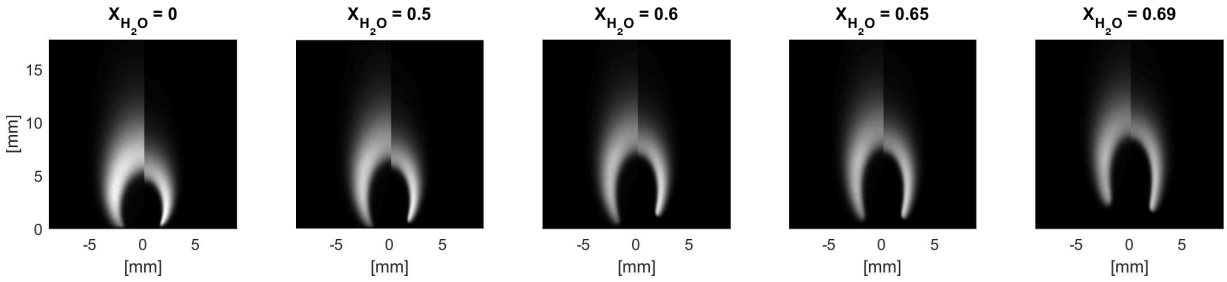

Figure 4.10: Experimental OH PLIF images (left) vs numerical OH simulations with the final inlet gases velocity profiles (right).

4.3 Simulated fluorescence

As mentioned in Section 2.4, OH PLIF measurements are complicated by phenomena such as collisional de-excitation (quenching), line-shape broadening and temperature sensitivity of the transition intensity. It is important to quantify those effects, as well as their evolution through the flame. Those effects can be quantified using the results obtained from the numerically simulated flames. Following the description of [57] and [58], the fluorescence signal can be modeled by generating the steady-state solution to the population rate equations for the states involved. The relationship between the fluorescence signal detected S_f and the OH density population N_{OH} can be expressed as follows:

$$S_f = C_{exp}\eta_f k_{\nu' J' \nu'' J''}(T) g(\phi_L(\nu)\phi_{OH}(\nu)) N_{OH} \tag{4.17}$$

where C_{exp} represents the group of experimental constants (such as the laser intensity, the probe volume, the collection solid angle and the transmission efficiency of the collection system); η_f is the fluorescence quantum yield (representing the fraction of fluorescence emitted spontaneously by a molecule compared to the overall de-excitation); $k_{\nu' J' \nu'' J''}$ represents the sensitivity to temperature (T) of the transition; $g(\phi_L(\nu)\phi_{OH}(\nu))$ is the overlap integral between the laser lineshape ϕ_L and the absorption lineshape ϕ_{OH} which are functions of frequency ν.

The following sections provide the details of the modeling of each of the phenomena considered and the quantification of the corrections needed in order to obtain the correct information on OH concentrations from the experimental PLIF results.

4.3.1 Fluorescence quantum yield

For a simplified two-level system, the quantum yield can be written as follows:

$$\eta_f = \frac{A_{J'J''}}{A_{J'J''} + Q_c} \tag{4.18}$$

where $A_{J'J''}$ is the spontaneous emission coefficient and Q_c is the quench rate. For OH in flame environments, Q_c is typically much greater that $A_{J'J''}$, this difference is also be enhanced, in this work, by the increasing presence of quenching species (H_2O and CO_2 diluents). Furthermore, the spontaneous emission coefficient represents a known constant which can be included in the term C_{exp} in Equation 4.17 [58]. The fluorescence quantum yield can then be written as:

$$\eta_f = \frac{1}{Q_c} = \frac{1}{N_{tot} \sum_i \chi_i \sigma_i(T) v_i(T)} = \frac{1}{\frac{p}{k_b T} \sum_i \chi_i \sigma_i(T) v_i(T)} \tag{4.19}$$

where N_{tot} is the total density population; p is pressure; k_b is the Boltzmann constant; χ_i is the colliding species mole fraction; σ_i is the quenching cross section; and $v_i(T)$ is the mean relative velocity between OH and the colliding species:

$$v_i(T) = \sqrt{\frac{8 k_b T}{\pi \mu_i}} \tag{4.20}$$

μ_i is the reduced mass of the ith collider:

$$\mu_i = \frac{m_i m_{OH}}{m_i + m_{OH}} \tag{4.21}$$

The quenching cross sections are modeled with the fit suggested by [59]:

$$\sigma_i(T) = C_0 \left((1 + h_c) e^{-h_c} + C_1 h_c^{2/\alpha} \gamma(2 - 2/\alpha, h_c) \right) \tag{4.22}$$

Species	C_0 [$\mathring{A}$]	C_1 [-]	C_2 [-]	α [-]
CO	12.297	1.664	6.206	4.60
H_2	4.240	1.360	3.079	3.50
O_2	7.997	1.327	3.866	3.95
NO	27.238	1.800	1.269	3.90
CO_2	11.872	1.391	8.205	3.22
H_2O	17.870	2.251	4.302	3.12
CH_4	13.679	1.109	3.591	3.05

Table 4.1: Fit coefficients used to model the quenching cross sections of the colliding species considered in this work.

with:

$$h_c = \frac{C_2 T_r}{T} \tag{4.23}$$

T_r is the reference temperature (300 K); C_0, C_1, C_2 and α are the fit constants as in Table 4.1; and $\gamma(a, b)$ is the incomplete gamma function.

The quench rate Q_c was calculated in each cell of the simulation domain for the various flame configurations by considering the following major colliding species: H_2O, CO_2, CO, CH_4, H_2, O_2 and NO. Figure 4.11 shows the modeled cross sections of the selected major colliding species as a function of temperature. It is clear that water is an important quencher, together with NO and CO_2. Higher water dilution levels in the flame will result in higher quenching rates.

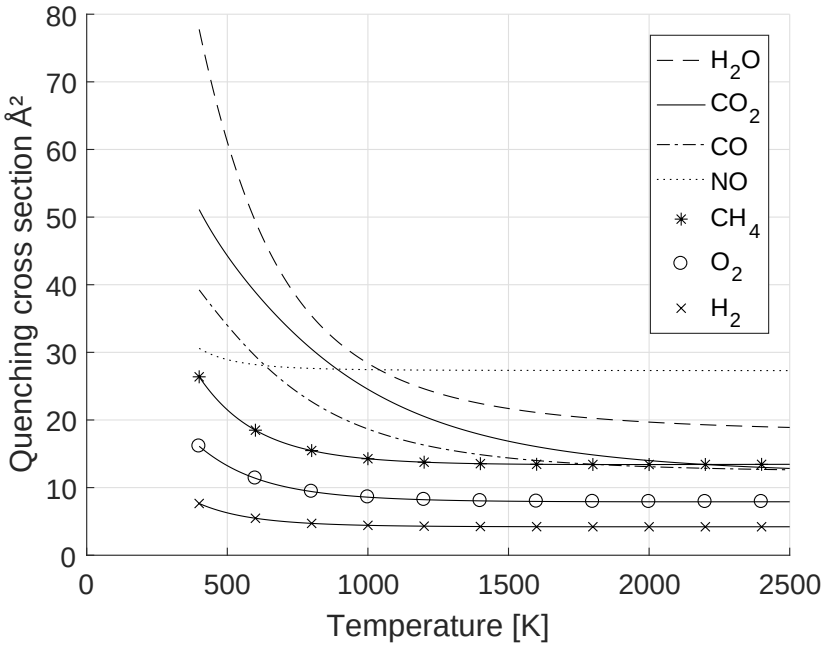

Figure 4.11: Modeled quenching cross sections of selected colliding species with OH as function of temperature.

Figures 4.12 and 4.13 shows the simulated results for the non diluted flame and for the 0.6 water mole fraction diluted flame. The left plots reports the quenching rate Q_c normalized by peak rate of the 0.6 water dilution case. The calculation of the quenching rates are performed over a region of interest, as will be discussed in the next section. The plot in the center shows the OH mass fraction, while the plot on the right represents the water mass fraction. Comparing the quenching rates with the water concentrations shows that higher quenching rates are present in the flame region where more water can be found, as expected.

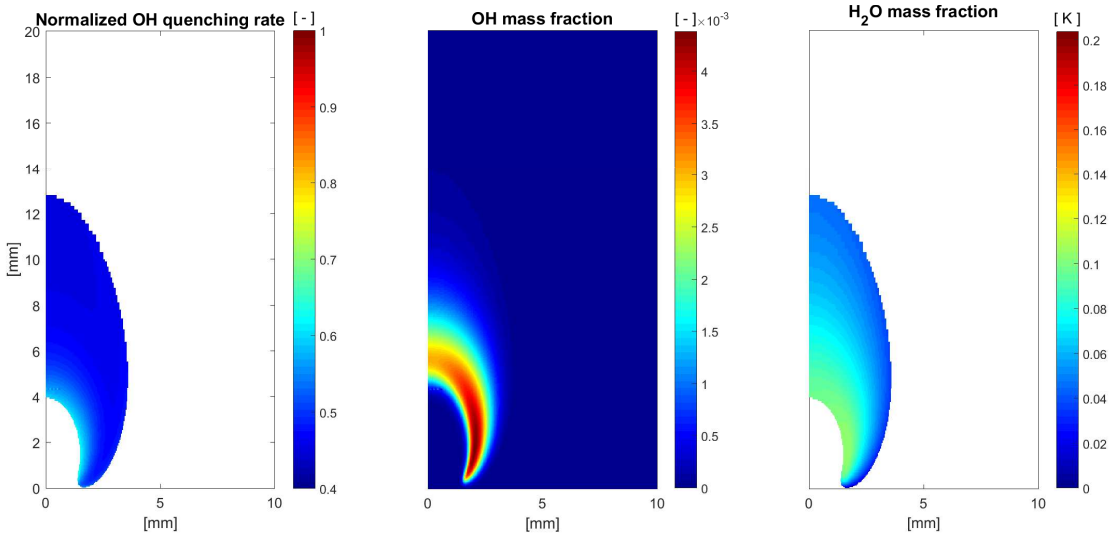

Figure 4.12: Simulated normalized OH quenching rate, OH mass fraction and water mass fraction for the non diluted flame.

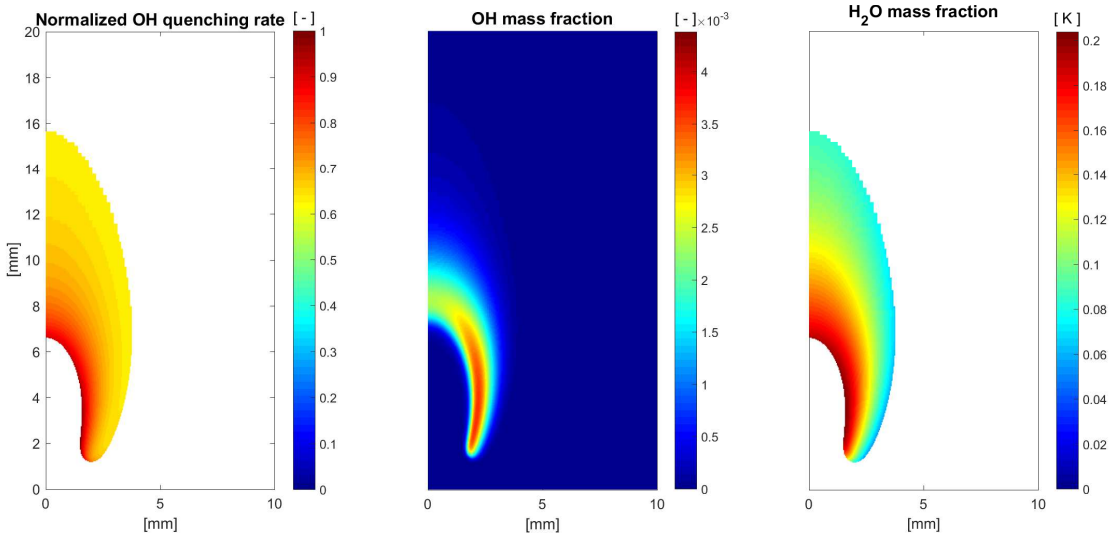

Figure 4.13: Simulated normalized OH quenching rate, OH mass fraction and water mass fraction for the 0.6 water mole fraction diluted flame.

4.3.2 Overlap integral

Broadening of spectral lines reflects the efficiency of the laser photons to interact with the species according to the probed transition. This effects can impact the interpretation of the measurements [39]. Line broadening can be caused by the thermal motion of the molecules (Doppler effect) or by pressure. However, with constant pressure through all the conditions

considered in this work, the effect of pressure broadening is not considered further.

The overlap integral g is defined as:

$$g = \int_{-\infty}^{+\infty} \phi_L(\nu)\phi_{OH}(\nu)d\nu \tag{4.24}$$

The laser lineshape is assumed to be Gaussian on average, so that it can be defined as follows:

$$\phi_L(\nu) = \sqrt{\frac{4\ln 2}{\pi \text{FWHM } c}} \exp\left[-4\ln(2)\left(\frac{\nu-\nu_0}{\text{FWHM } c}\right)^2\right] \tag{4.25}$$

where the FWHM of the laser was estimated to be 0.15 cm^{-1} by [40]; c is the speed of light; and ν_0 is the transition center frequency. The Doppler lineshape function is defined as:

$$\phi_{OH}(\nu) = \frac{c}{\nu_0}\sqrt{\frac{m}{2\pi k_b T}} \exp\left[-4\ln(2)\left(\frac{\nu-\nu_0}{\Delta\nu_D}\right)^2\right] \tag{4.26}$$

where m is the molecular mass; and $\Delta\nu_D$ the transition width.

$$\Delta\nu_D = \frac{2\nu_0}{c}\sqrt{\frac{2\ln(2)k_b T}{m}} \tag{4.27}$$

As the calculation of the convolution integral in each pixel of the flame requires a considerable amount of computing time, it was only calculated at each grid of the simulation domain with OH mass fraction greater than 10^{-4}. Figures 4.14 and 4.15 report the overlap integral value normalized by the peak value in the zero dilution case, the OH mass fraction, and the temperature profiles for the zero and 0.6 water mole fraction diluted flames. The overlap integral is a function of temperature; in particular, from the equations above, it is possible to write:

$$g \propto \frac{e^{-\frac{1}{T}}}{\sqrt{T}} \tag{4.28}$$

which decreases with increasing temperatures. Consistently with this, Figures 4.14 and 4.15 show larger values of the overlap integrals for flame regions with lower flame temperatures.

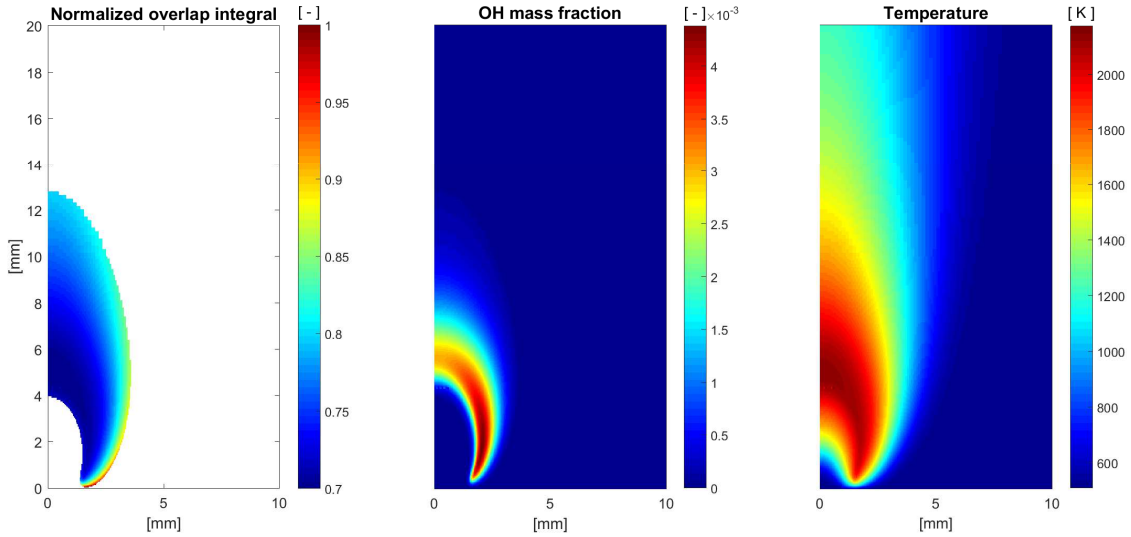

Figure 4.14: Simulated normalized overlap integral values, OH mass fraction and temperatures for the non diluted flame.

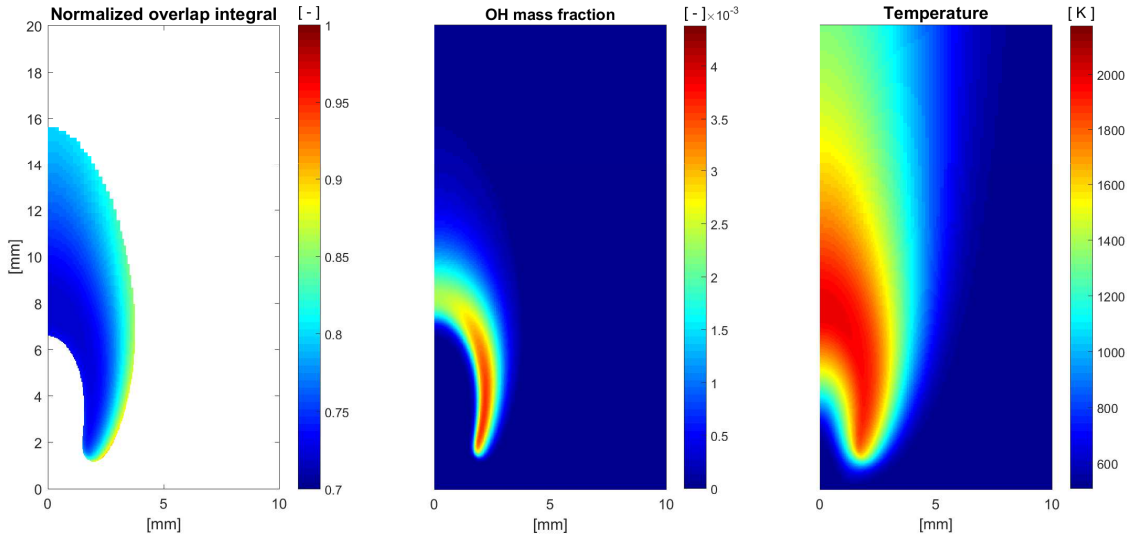

Figure 4.15: Simulated normalized overlap integral values, OH mass fraction and temperatures for the 0.6 water mole fraction diluted flame.

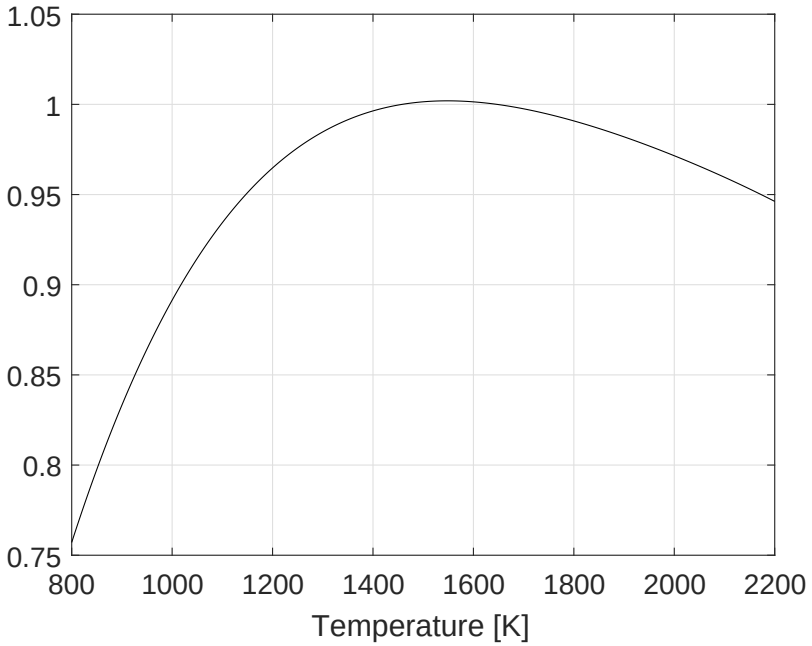

Figure 4.16: Sensitivity of the $Q_1(7)$ transition used in this work to temperature.

4.3.3 Absorption line temperature sensitivity

The temperature dependence of the ground state of OH was simulated by [40] following the work of [60], and results are reported in Figure 4.16. As for the other effects, the temperature sensitivity was accounted for in each cell of the numerical domain.

Figures 4.17 and 4.18 report the simulated temperature sensitivities and the temperature profiles for the zero and 0.6 water mole fraction diluted flames. Higher contributions can be seen for temperatures between 1400 and 1600 K. Thus, a larger contribution to the fluorescence signal is present for higher diluted flames.

The quenching, line-shape broadening and temperature sensitivity effects are calculated for each numerical case run and accounted for as described by Equation 4.17 to obtain the simulated fluorescence results discussed in Chapter 5.

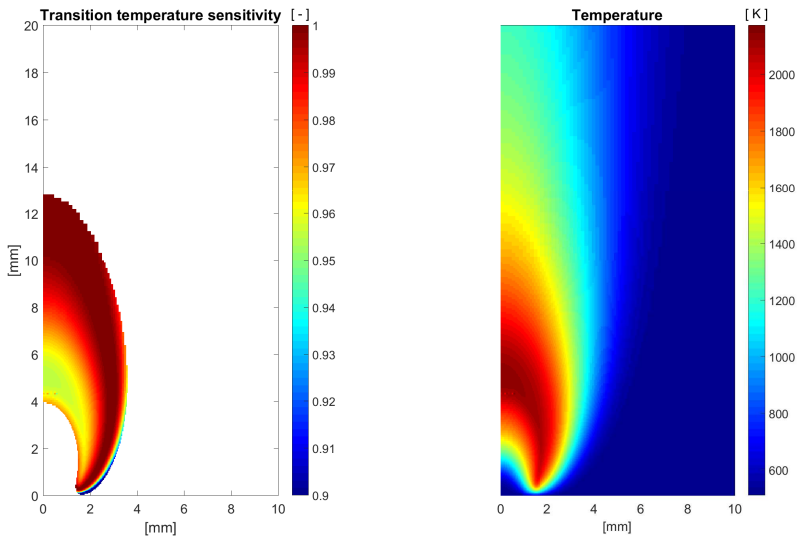

Figure 4.17: Simulated temperature sensitivity of the transition, and temperature profiles for the non diluted flame.

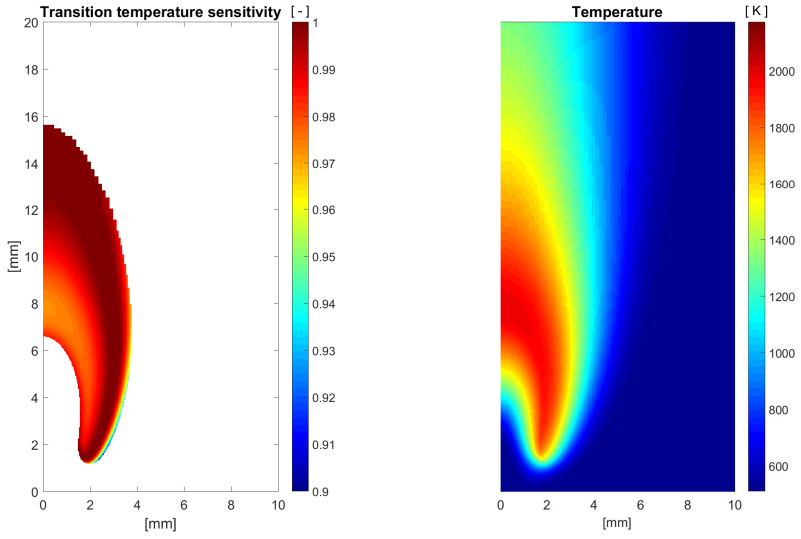

Figure 4.18: Simulated temperature sensitivity of the transition, and temperature profiles for the 0.6 water mole fraction diluted flame.

Chapter 5

Results and discussion

In this chapter, the experimental and numerical results are compared and discussed. In particular, temperatures results and OH, H and O radical pools are analyzed.

5.1 Temperatures

Figure 5.1 shows the experimental and numerical peak temperatures for the water diluted flames at constant methane flow rate. The PeleLM simulations match well the maximum temperature near extinction but over predict the flame temperatures at lower water mole fractions. This is likely an effect of heat losses to the burner that are not accounted for in the numerical model. As the fuel dilution level is increased, the flame lifts (in both the experiments and the simulations) resulting in lower losses, and a better prediction of the flame temperature can be obtained by the numerical results. The temperature of the burner fuel tip was monitored using a FLIR SC 620 IR camera as the flame was burning with increasing water concentration in the fuel flow. As the flame lifted, the burner tip temperature decreased confirming that heat losses to the burner can play an important role

at low dilution levels. The results of those tests can be found in Appendix E. Similar to the experiments, where extinction happens between 0.705 and 0.715, the numerical results predict extinction between 0.69 and 0.72 water mole fraction.

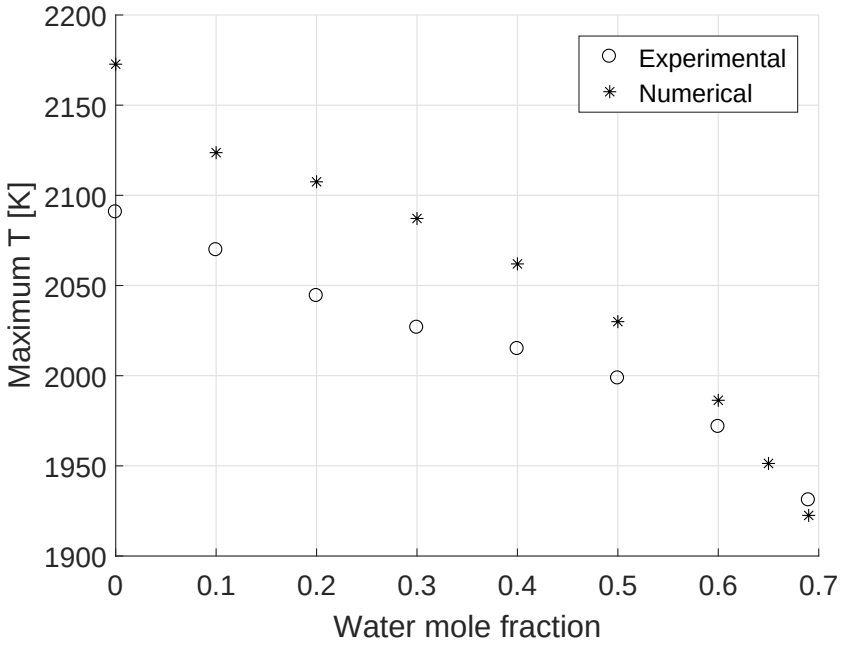

Figure 5.1: Experimental vs numerical peak temperature with H_2O dilution.

Figure 5.2 shows the peak temperature of the simulated flames with increasing levels of H_2O and CO_2 dilution. The simulations show a similar trend in peak temperatures between the two diluents, and agree with the experimental results reported in Chapter 3. For the case of CO_2 dilution, the simulations show a difference in peak temperatures between the two diluents of about 60 K. As seen from the experimental results, at constant heat capacity rates, the CO_2 diluted flame is sustained at a slightly lower temperature. However, extinction happens at the same levels of thermal loading introduced by the diluents, suggesting that the CO_2 diluted flame is a stronger flame than the water case. To further analyze such hypothesis, the following sections will evaluate the concentrations of O, H and OH radicals, which represent the key chain branching species responsible for sustaining all combustion systems.

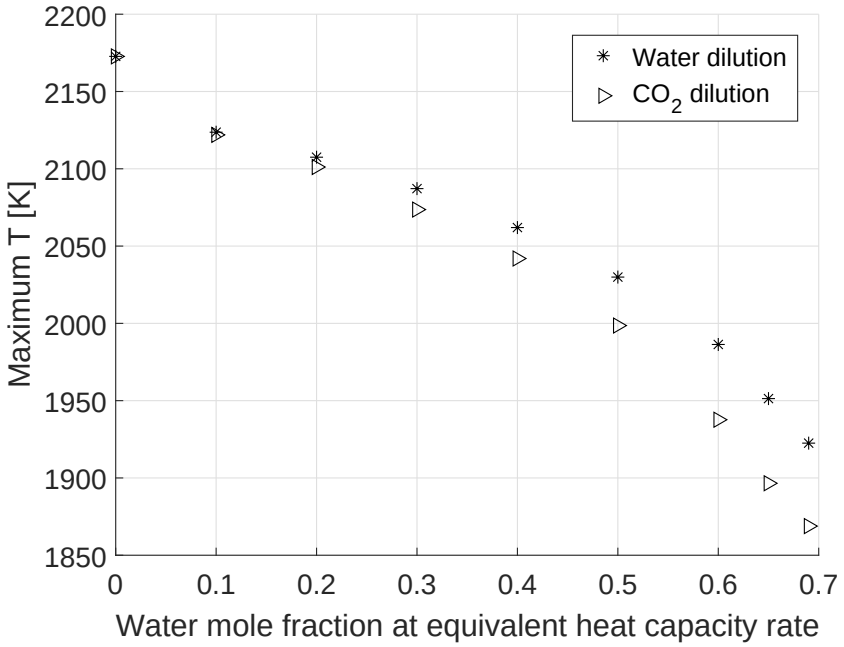

Figure 5.2: Numerical peak temperature with H_2O and CO_2 dilution.

5.2 Radical concentrations

5.2.1 OH experimental and numerical distribution profiles

Figures 5.3 and 5.4 shows the comparison between experimental and numerical OH profiles at different water and CO_2 dilution levels. For each flame image, results from PLIF are plotted on the left, while numerical results are on the right. In both experimental and numerical images, each pixel is normalized by the maximum intensity of the zero dilution case. The inlet velocity profiles in the PeleLM simulations for high concentrations of water dilution were adjusted in order to obtain a flame with a similar shape to the experimental run. This was discussed in the previous chapter. However, in the case of CO_2, reported in Figure 5.4, the velocity profile used for the air coflow is the same for all the dilution levels and corresponds to the water cases between 0 and 60% diluent concentration. This shows that the simulations can predict well the shape and the lift-off height of the flames with CO_2 dilution, while they do not do so at high water addition levels.

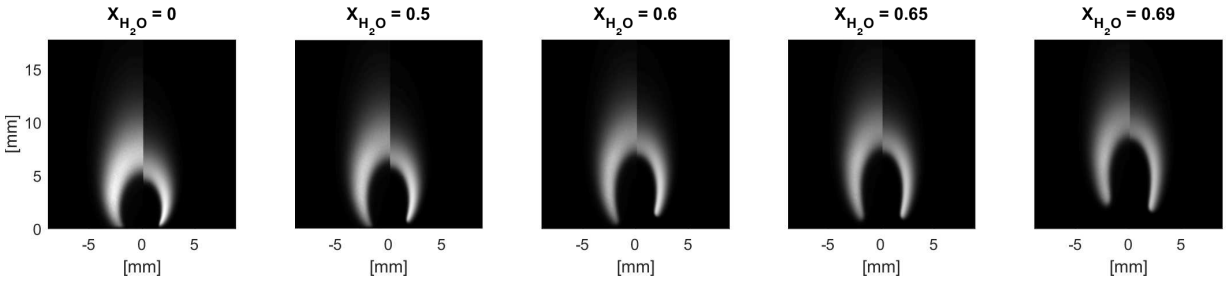

Figure 5.3: Experimental (left) vs numerical (right) results for OH profiles at increasing H_2O concentrations.

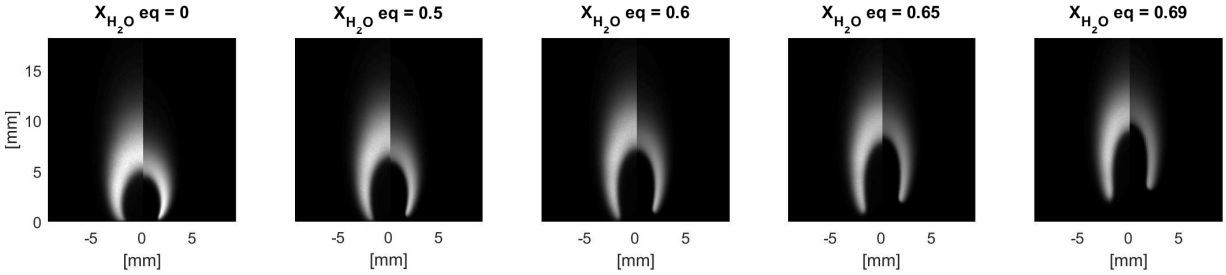

Figure 5.4: Experimental (left) vs numerical (right) results for OH profiles at increasing CO_2 concentrations.

5.2.2 OH experimental and numerical concentrations

OH profiles are first compared by integrating the experimental and numerical radical concentrations. To account for stretching of the flame at different dilution levels and different diluents, the results are also normalized by the flame wing height. The flame wing height is defined as the vertical distance between the flame edge and the position of maximum OH gradient along the axis, as shown in Figure 5.5. Figure 5.6 reports the experimental integrated OH and the integrated OH molecule count obtained from simulated fluorescence, for the water dilution case. The integrated values are normalized by the zero water case. Figure 5.6 (a) shows good agreement between the experimental and numerical data. As dilution increases, the flame lifts and stretches. To account for possible changes in flame shape, the integrated OH results are normalized by the flame wing height in Figure 5.6 (b). Similarly, Figure 5.7 is obtained using the same methods, but integrating OH only over the flame wing region. Doing so, it is possible to see that the decrease in OH with water dilution in this

region is always greater than the corresponding value when integrating over the whole domain. This is suggesting that, as water is added to the flame, more OH needs to be present in the wing region for the flame to be sustained.

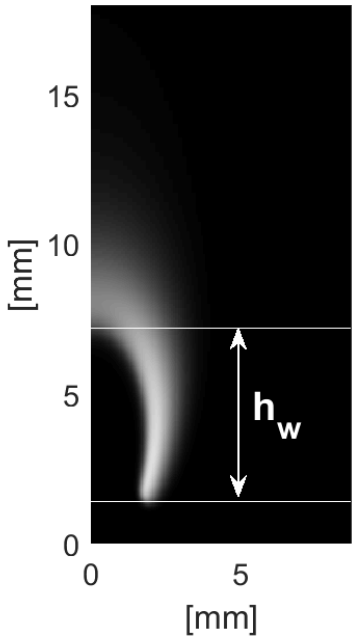

Figure 5.5: Flame wing height h_w in a typical flame.

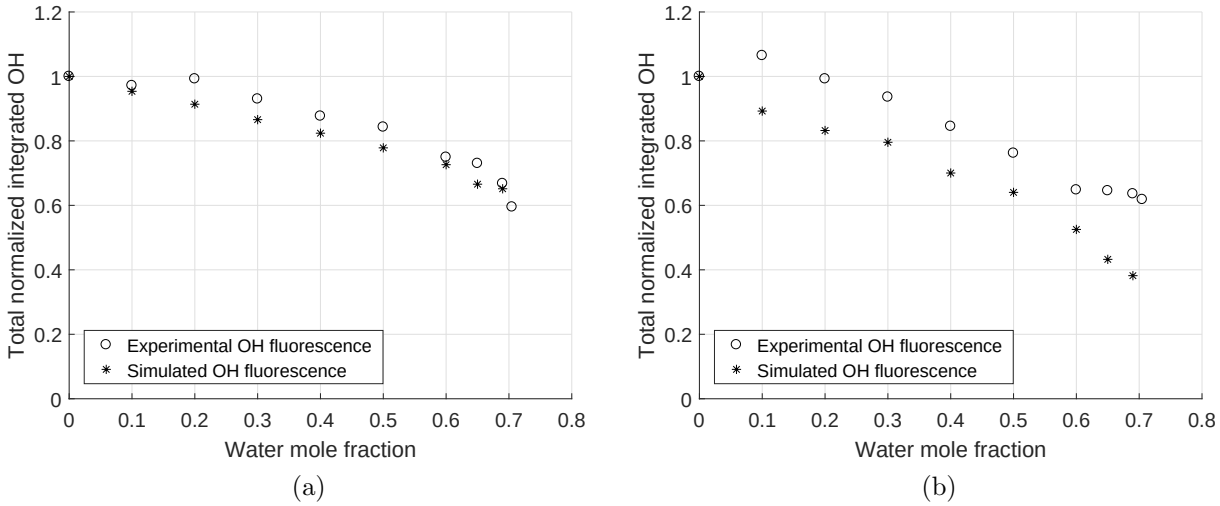

Figure 5.6: Experimental vs simulated fluorescence for H_2O diluted flames: (a) integrated OH over the whole domain; (b) integrated OH over the whole domain, normalized by flame wing height.

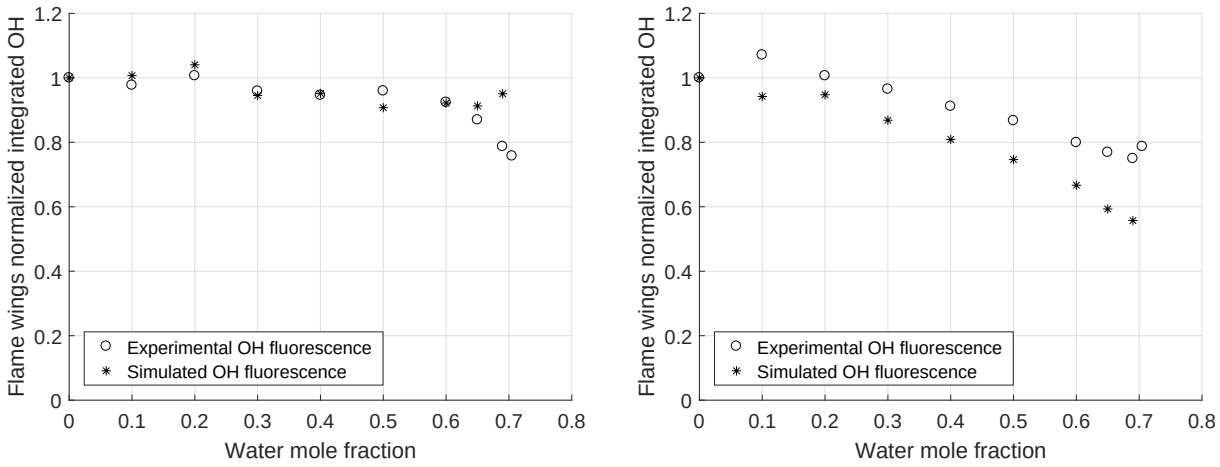

Figure 5.7: Experimental vs simulated fluorescence for H_2O diluted flames: (a) integrated OH over the wing region; (b) integrated OH over the wing region, normalized by flame wing height.

Similarly to what was discussed before for the water diluted flames, Figures 5.8 and 5.9 report the experimental PLIF and numerical fluorescence integrated OH results for the CO_2 diluted flame. In this case, the simulations under-predict more the OH concentrations with respect to the water case. This can also be seen from the images in Figure 5.4, where the experimental results appear clearly brighter than the numerical ones. Consistently with the water case, if the OH integration is performed only over the flame wing region, the relative concentrations appear higher than the case where integration is done on the overall domain.

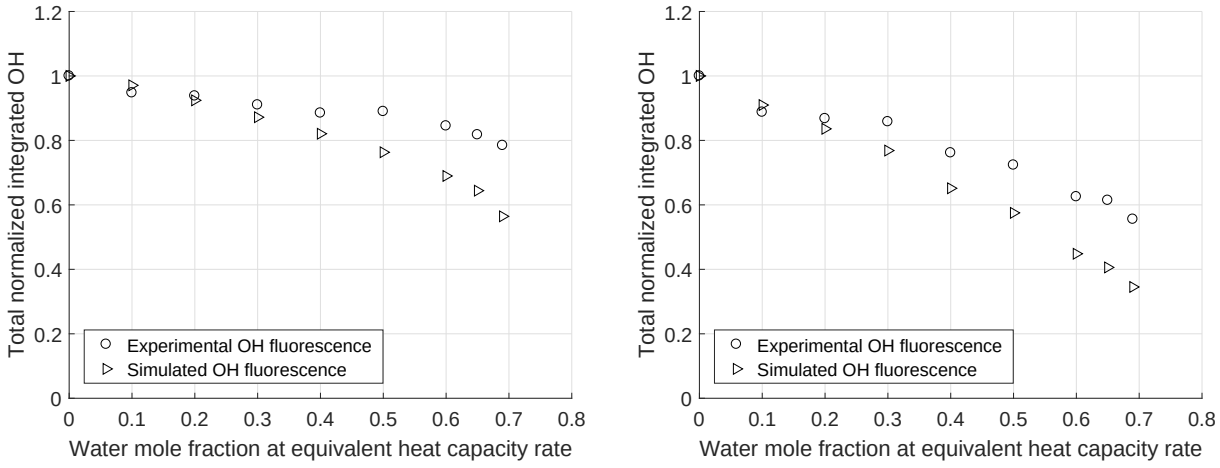

Figure 5.8: Experimental vs simulated fluorescence for CO_2 diluted flames: (a) integrated OH over the whole domain; (b) integrated OH over the whole domain, normalized by flame wing height.

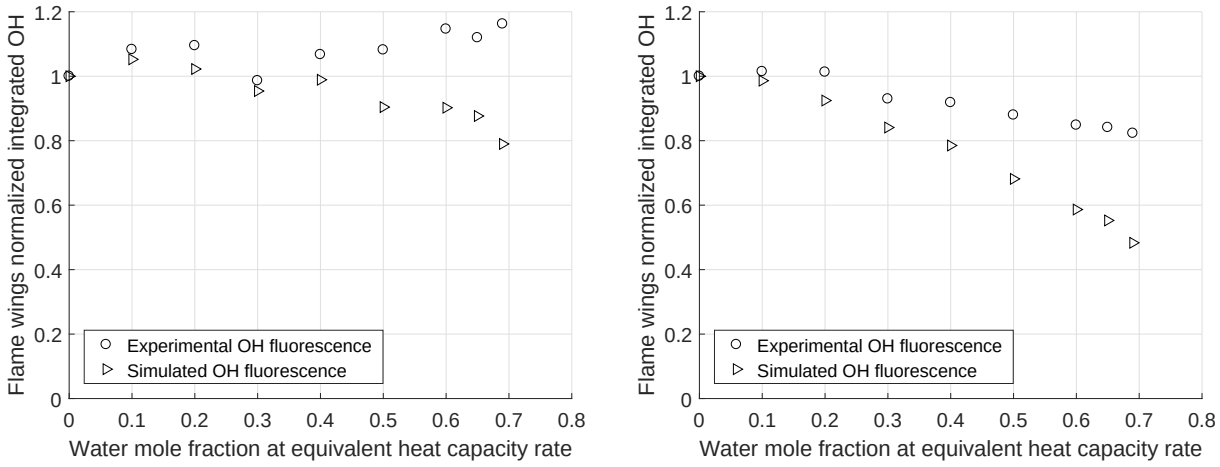

Figure 5.9: Experimental vs simulated fluorescence for CO_2 diluted flames: (a) integrated OH over the wing region; (b) integrated OH over the wing region, normalized by flame wing height.

Figures 5.10 and 5.11 report the integrated OH molecule count obtained numerically for the H_2O and CO_2 diluted flames. In this case, those are not the simulated fluorescence results, but the prediction of the total OH present in the flame. It is interesting to notice that, independently of the figure of merit used, the simulations always predict higher concentration of OH in the water case. This agrees with the notion found in the literature that water enhances OH production in the flame. Figure 5.10 (a) shows that the total concentration of OH remains about constant in the water case, while it decreases with increasing CO_2 dilution. In both diluent cases, the temperature decreases with increasing mole fraction of water or CO_2, thus the behavior of OH cannot be related purely to a thermal effect when water is added to the flame. Moreover, when looking at the OH concentrations in the wing region in Figure 5.11 (a), it is clear that the OH radical concentration increase with dilution, but it increases considerably more with addition of water to the fuel stream.

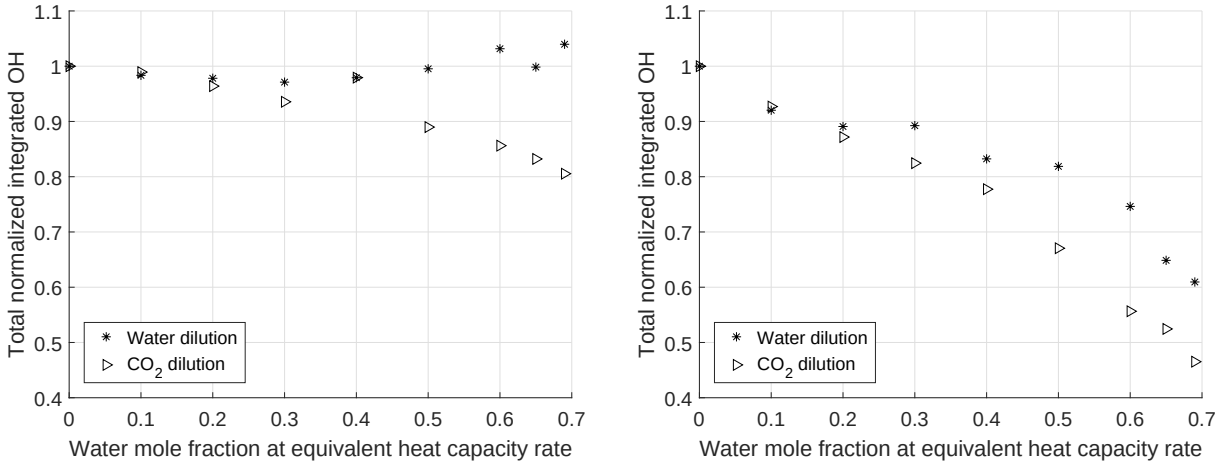

Figure 5.10: Simulated OH concentrations for H_2O and CO_2 diluted flames: (a) integrated OH over the whole domain; (b) integrated OH over the whole domain, normalized by flame wing height.

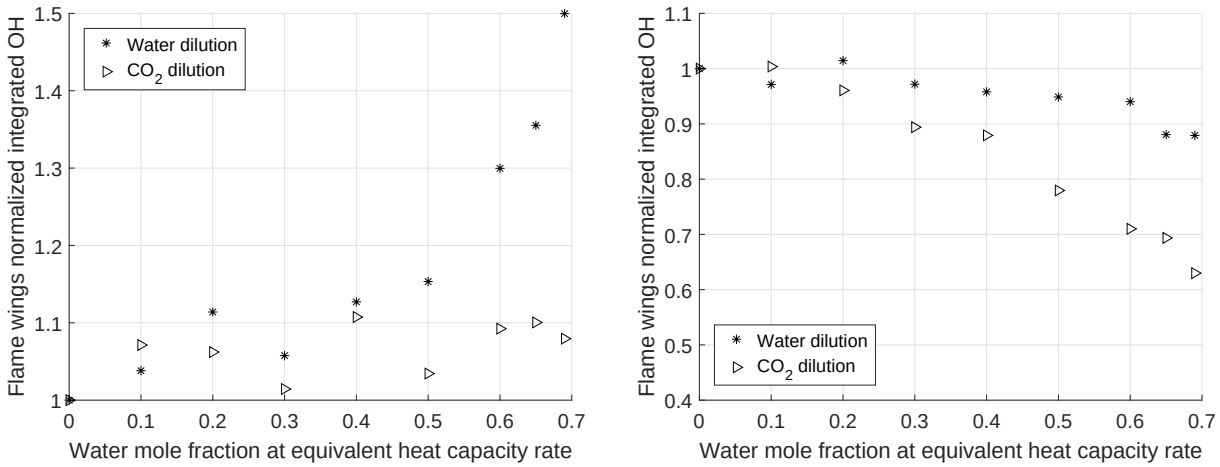

Figure 5.11: Simulated OH concentrations for H_2O and CO_2 diluted flames: (a) integrated OH over the wing region; (b) integrated OH over the wing region, normalized by flame wing height.

Figure 5.12 shows the axial distribution of OH obtained through numerical simulation. Figure 5.12 (a) represents the water diluted flame, while Figure 5.12 (b) is for CO_2 dilution. All curves are normalized with respect to the maximum OH concentration along the axis in the zero water dilution case. It is important to notice that the location of peak OH along the axis does not change between the simulated overall OH concentration and the simulated OH fluorescence. Moreover, from those images it is possible to see that OH decreases more with CO_2 increasing dilution levels than with water, and the decrease in OH concentration detected with fluorescence is more important in the water case as the H_2O molecule is a better fluorescence quencher than CO_2. Figure 5.13 shows the OH trends along the flame axis found experimentally. Each curve is obtained by integrating the flame axis and its left and right pixel vertically. Normalization is done with respect to the maximum intensity obtained for the zero dilution case. As expected, for high dilution levels the CO_2 flame shows a larger OH concentration, but this is not accounting for the greater quenching that affect the water flame with respect to CO_2 dilution. From this image, it is also possible to see that, as dilution increases, the CO_2 flame stretches more than the water one, and its OH peak

appears at a higher vertical location in the flame.

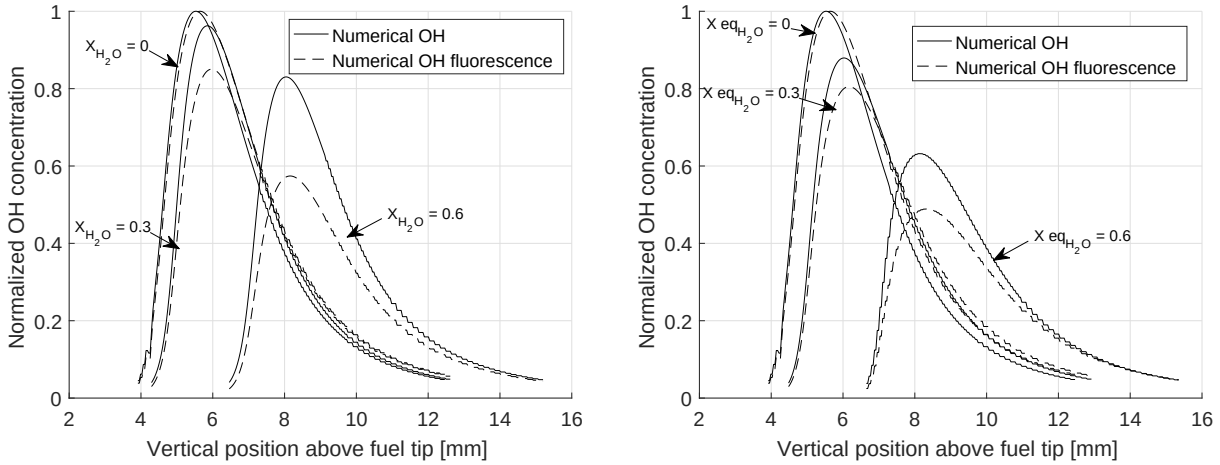

Figure 5.12: Numerical OH and simulated OH fluorescence results along the flame axis: (a) H_2O diluted flame; (b) CO_2 diluted flame.

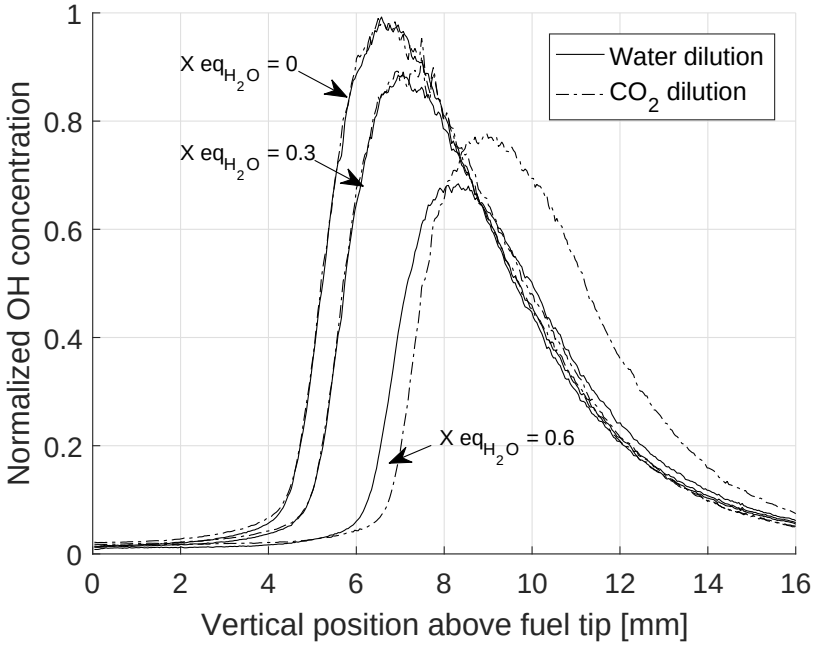

Figure 5.13: Experimental OH along the flame axis for the H_2O and CO_2 diluted flames.

Figure 5.15 shows the horizontal distribution of OH obtained through numerical simulation. The horizontal position is selected as half way between the flame edge and the axial position of the maximum OH gradient, this is half way up the flame wing, as shown in Figure

5.14 for a typical flame. As in the concentration along the axis, performing simulated fluorescence on the numerical results does not change the location of the peak concentration. As expected, water has a larger quenching effect than CO_2. Those results are consistent with the results shown before: at higher dilution concentration, the water diluted case presents higher amounts of OH. Figure 5.16 reports the experimental results. In this case, the curves are obtained by vertically integrating the pixel line at the mid location of the flame wing, with the next two pixels. The image shows corresponding peaks between water and CO_2 diluted flames, suggesting higher concentrations in the water case if quenching was to be considered. This results is also in agreement with the trends shown before. Figures 5.15 and 5.16 also show a difference in the peak horizontal location between the experiments and the numerical simulations. PeleLM predicts the peaks to be closer to the flame axis than is seen in the experiments.

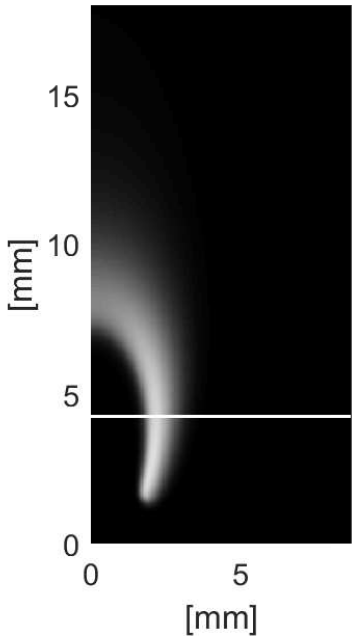

Figure 5.14: Mid location of the flame wing in a typical flame.

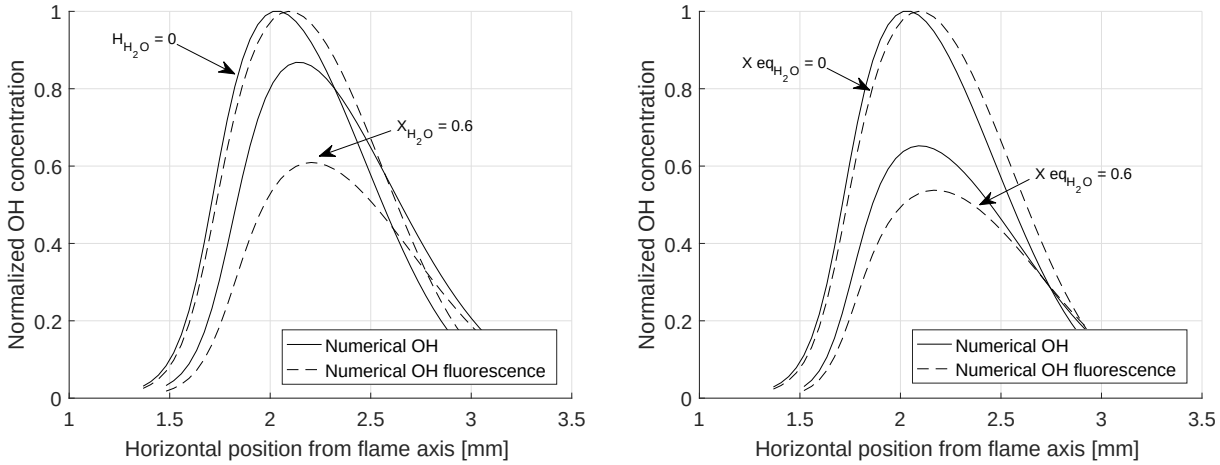

Figure 5.15: Numerical OH and simulated OH fluorescence results horizontally half way between the flame edge and the maximum OH gradient on the axis: (a) H_2O diluted flame; (b) CO_2 diluted flame.

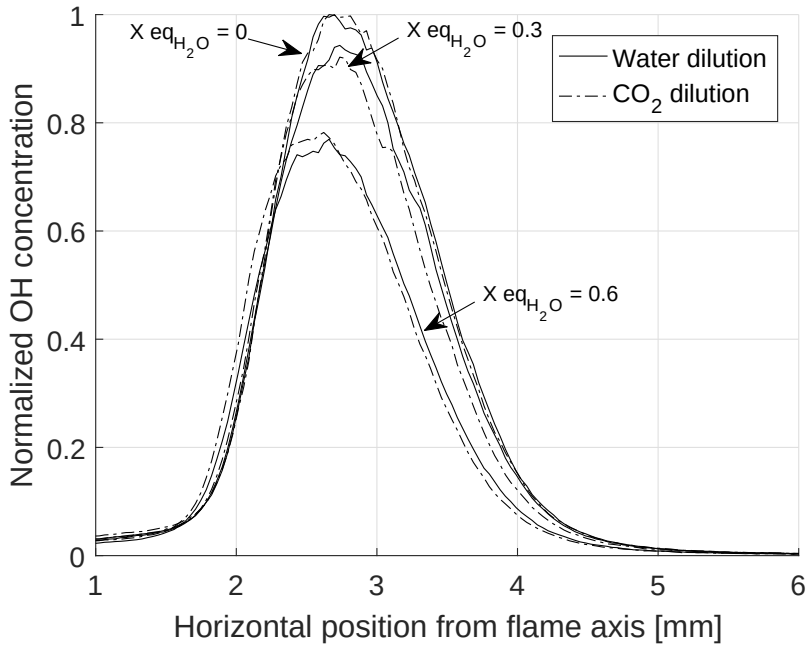

Figure 5.16: Experimental OH horizontally half way between the flame edge and the maximum OH gradient on the axis for the H_2O and CO_2 diluted flames.

5.2.3 O and H numerical concentrations

Figures 5.17 and 5.18 show the trends of the radical species O and H obtained from the PeleLM simulation. The star data points represent water, while the triangles represent CO_2 dilution. Blue is used for normalized O concentrations, while red is used for the H radical. It is clear from the images, that O is always present in larger amounts when the flame is diluted with CO_2, while the H concentrations trends are similar for the two diluents considered. This behavior of the CO_2 diluted flame is related to the diluent molecule being an active participant in the reaction, just as occurs for water but in a different way. This result support the hypothesis that the water diluted flame is weaker than the CO_2 flame even with larger amounts of OH present. In the CO_2 case, more O is present in the flame which is also an important radical to sustain the reaction process.

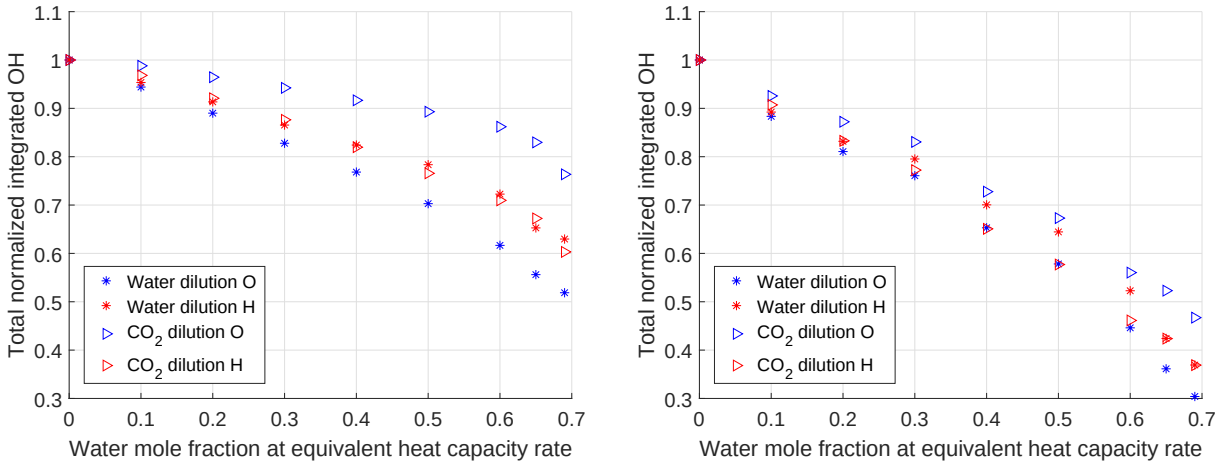

Figure 5.17: Simulated O and H concentrations for H_2O and CO_2 diluted flames: (a) integrated O and H over the whole domain; (b) integrated O and H over the whole domain, normalized by flame wing height.

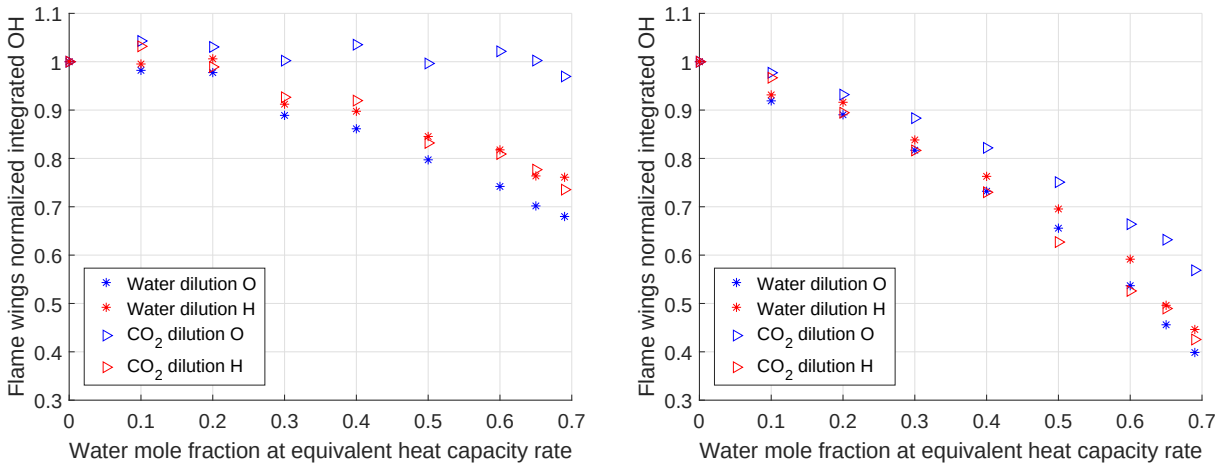

Figure 5.18: Simulated O and H concentrations for H_2O and CO_2 diluted flames: (a) integrated O and H over the wing region; (b) integrated O and H over the wing region, normalized by flame wing height.

5.2.4 N_2 dilution

In the previous sections, numerical and experimental results from water and carbon dioxide diluted flames showed than both diluents can actively participate in the reaction chemistry. Water promotes OH, while dilution with CO_2 enhance production of the O radical in the flame. A better comparison would include dilution with an inert species. PeleLM simulations were run, for some selected condition, using nitrogen as a diluent. Figure 5.19 shows the integrated OH and temperature results. In Figure 5.19 (a) the integrated OH over the entire region shows that OH concentrations are higher than in the case of carbon dioxide dilution when nitrogen is added to the fuel stream. As expected, OH concentration in the water case are nigher than the N_2 case. Additional plots of OH concentrations can be found in Appendix F. However, independently from the figure of merit used, OH concentrations in the nitrogen case are always higher than in the CO_2 diluted flames, and lower than in the water case. Figure 5.19 (b) shows agreement in peak temperatures between the water and nitrogen case, as was also seen from the experimental results. Figure 5.20 reports O and H radicals concentrations. O and H concentrations remain almost constant as additional inert

is introduced into the combustion process.

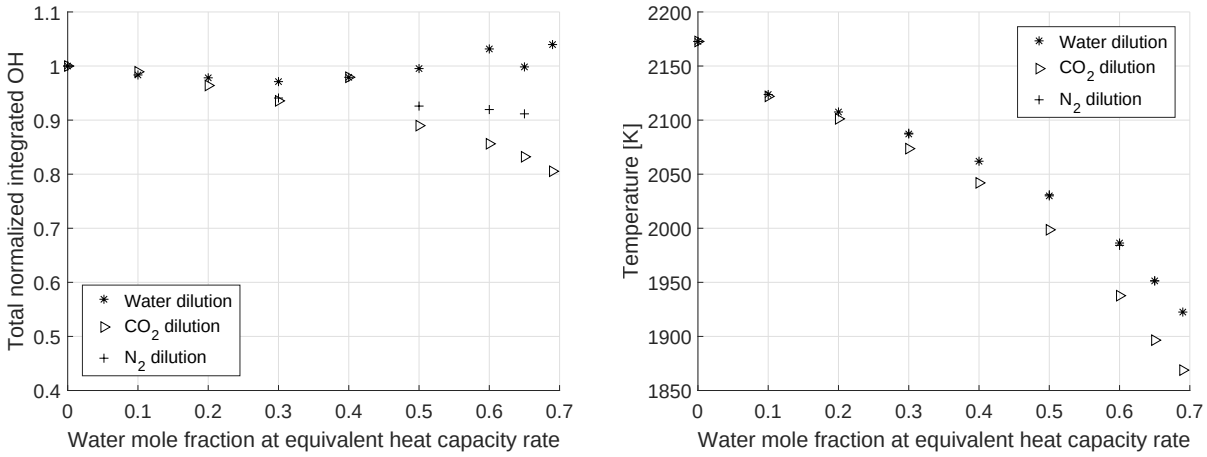

(a) (b)

Figure 5.19: Simulated results for H_2O, CO_2 and N_2 diluted flames: (a) simulated integrated OH over the whole domain; (b) flame peak temperature.

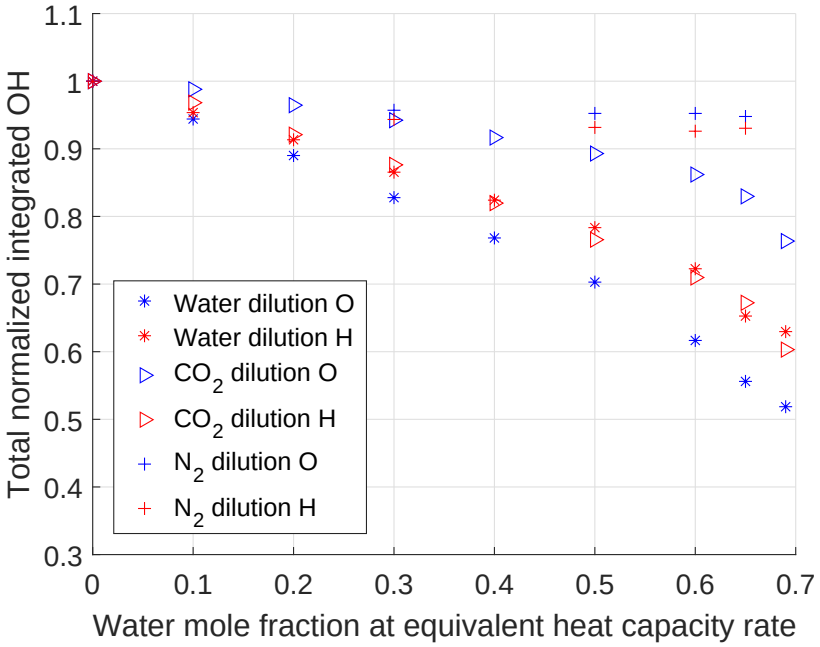

Figure 5.20: Integrated O and H over the whole domain for H_2O, CO_2 and N_2 diluted flames.

5.3 Strain rates

One possibility to explain the difference in the flames diluted with CO_2 versus water vapor is the physical changes due to local strain rates when the flame shape and location varies. To investigate this element of the flames, strain rates were calculated from the velocity profiles obtained numerically. The maximum temperature sheet was identified, and the tangential strain rate in this region was calculated as the spatial derivative of the tangential velocity. Figure 5.21 shows an example of the maximum temperature flame sheet plotted on top the numerical temperature profiles for a typical flame.

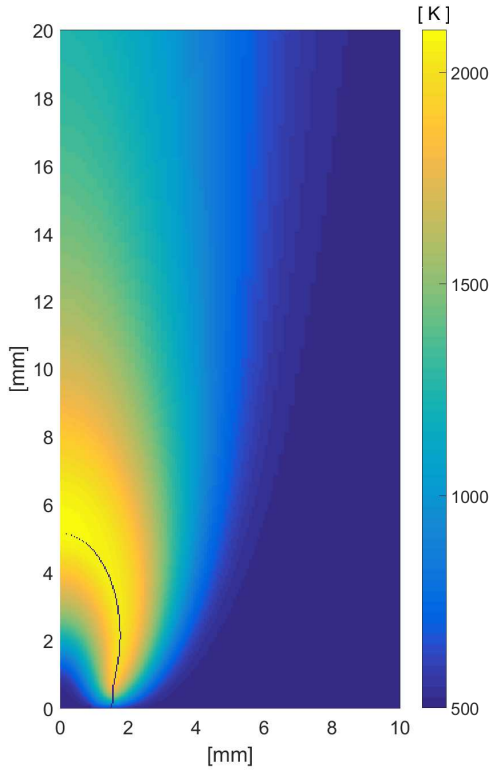

Figure 5.21: Numerical temperature profile, and maximum temperature flame sheet of a typical flame.

Figures 5.23 and 5.24 show the strain rates, temperatures and gas velocities for the 0.3 and 0.6 water mole fractions diluted flames. The strain rates and velocities are calculated on the location of the maximum temperature line, in the flame edge region. The ignition

temperatures for the diluted flames, were calculated using the Chemkin-Pro perfectly stirred reactor module [61]. The ignition temperature does not change greatly with water addition; it ranges between 1395 K and 1435 K from 0 to 0.69 mole fractions of water added to the fuel. Because the temperature does not vary significantly, another possibility for the difference in the positioning of the flame edge between the water and CO_2 cases would be a variation in flame burning velocities. The flame laminar burning velocity was calculated using the Chemkin-Pro flame speed module, with increasing amounts of H_2O and CO_2 dilution to a methane fuel stream. For inlet temperatures of 510 K (as the ones in the experiments), the calculated flame burning velocities are plotted in Figure 5.22. The plots show lower velocities with increasing dilution levels, and higher velocities for addition of water with respect to CO_2 as diluent. The difference in laminar burning velocities of the two diluents is due to the higher specific heat capacity of carbon dioxide [62]. In classical flame stabilization theory for the flame edge to remain anchored and stable, the gas velocity has to be equal to the laminar burning velocity. Thus, the gas velocities at the flame edge (as shown in Figures 5.23 and 5.24) can be compared to the laminar burning velocities. The gas velocities are significantly smaller than the laminar burning velocities reported in Figure 5.22. Thus, it is not possible to explain the flame edge positioning with respect to the fuel tube tip by direct comparison of the flame speed. The laminar burning velocities are also affected by the flame stretching. Several works found in the literature showed that laminar burning velocities increase with flame stretch [63, 64]. This result would not explain the higher lift-off height of the water diluted flame near extinction with respect to the carbon dioxide diluted one. Hence, the location of the flame edge is not associated with a balanced flow and burning velocity configuration. Rather, the flame edge will be governed by a mixing process of fuel and oxidizer.

As dilution is increased, the strain rate at the flame edge, around the ignition temperature, decreases for both diluents considered. Moreover, strain rates are higher in the case of CO_2 addition. The water diluted flame sits on a less strained region even if both numerical

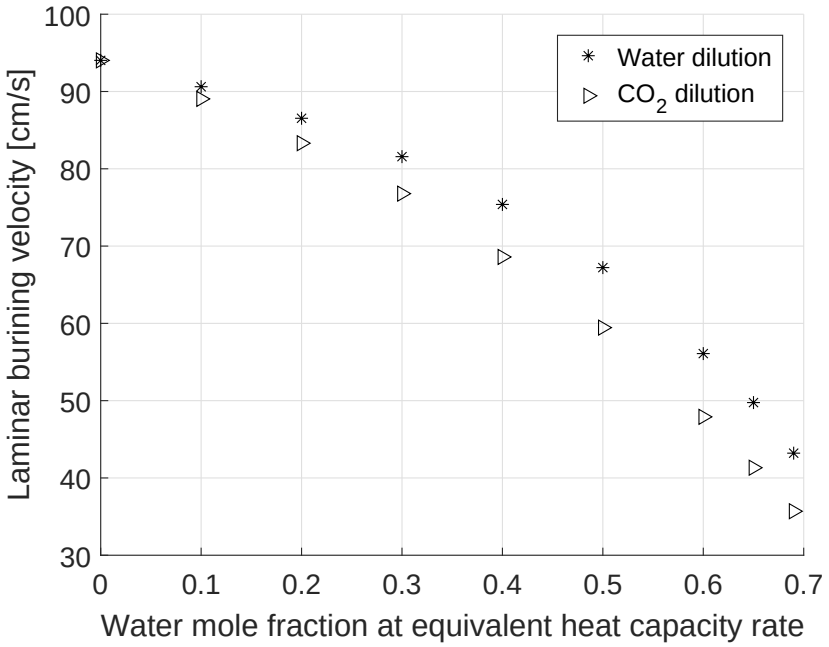

Figure 5.22: Laminar burning velocities for H_2O and CO_2 diluted flames with 510 K inlet temperature.

and simulation results show a slightly higher temperature and higher OH concentrations with respect to the CO_2 case. This suggests that the flame, even with higher OH radical concentration, is weaker than the CO_2 diluted flame.

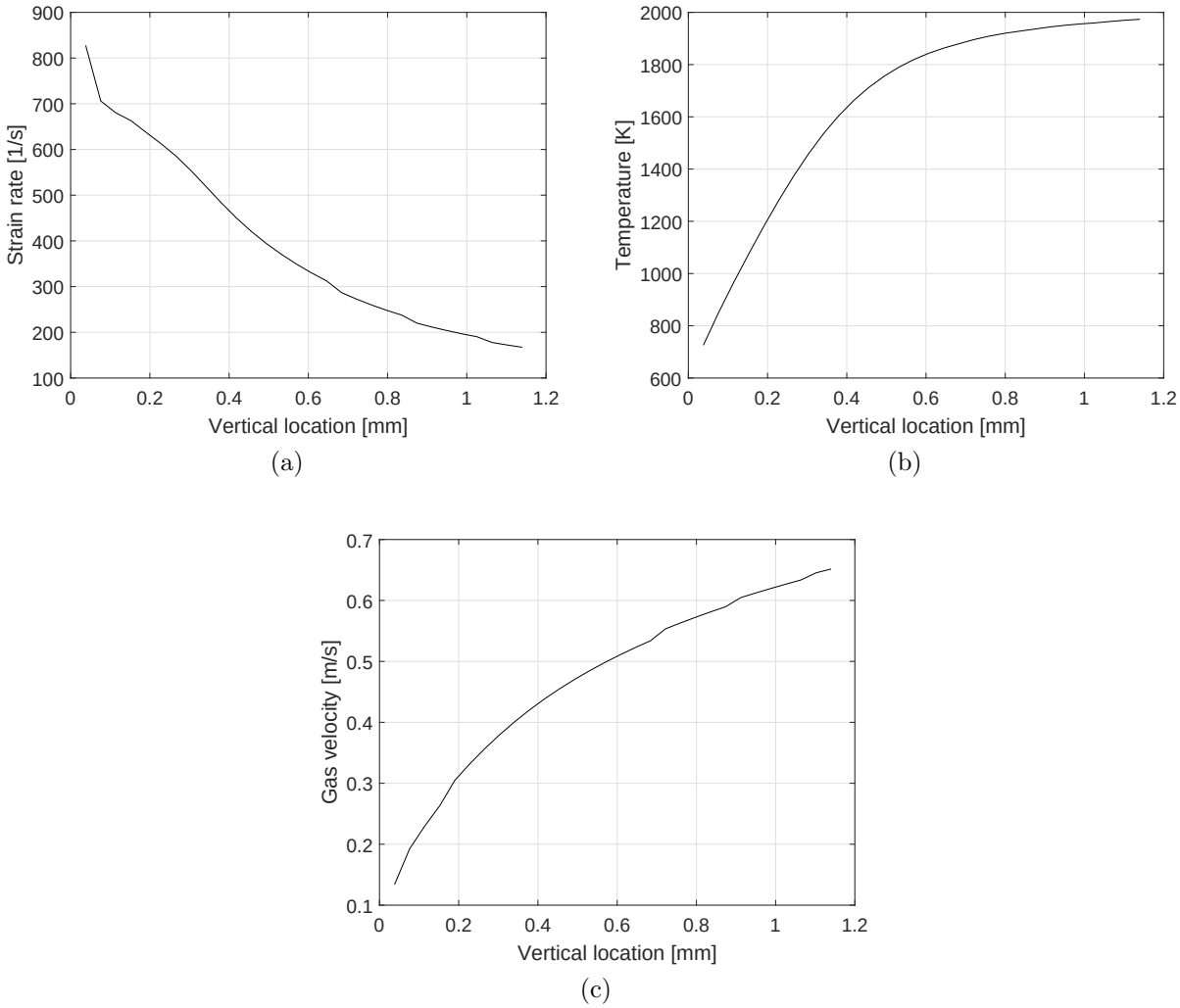

Figure 5.23: 0.3 water mole fraction diluted flame: (a) Strain rate along the maximum temperature line; (b) temperature; (c) gas velocity.

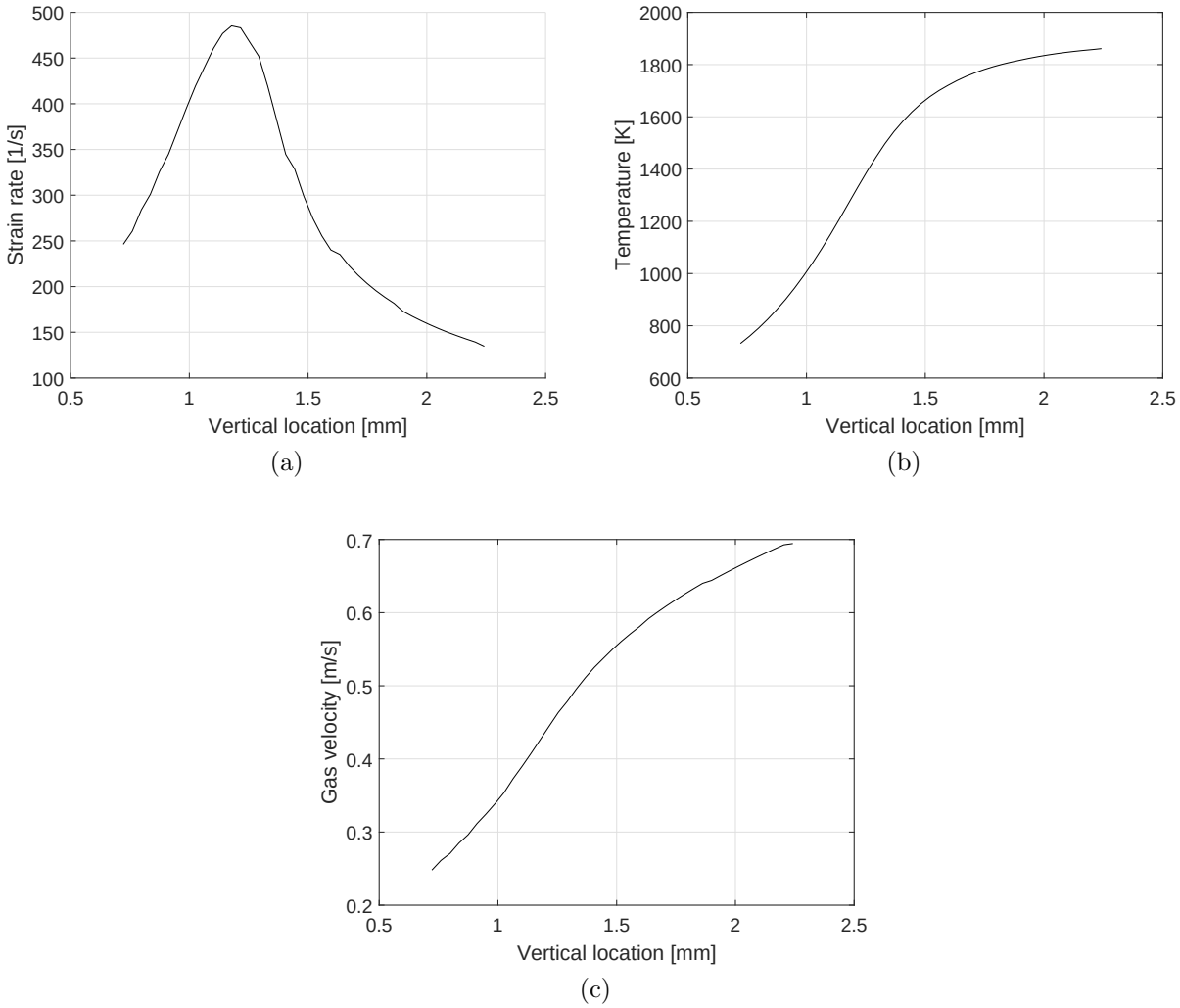

Figure 5.24: 0.6 water mole fraction diluted flame: (a) Strain rate along the maximum temperature line; (b) temperature; (c) gas velocity.

Chapter 6

Conclusions and future work

6.1 Summary and conclusions

Several studies can be found in literature investigating the role of liquid and vapor water in combustion processes. However, water addition in premixed flames or dilution of the oxidizer stream of diffusion flames are the more common configurations investigated. As discussed in Chapter 1, the role of water addition in combustion has several facets that have not been resolved, particularly in the case of non-premixed combustion when water dilutes the fuel. In addition to the lack of information regarding this configuration, numerical and experimental investigations of water dilution found in the literature are performed under a wide spread of conditions and set-ups. This generates confusion and ambiguity when results are to be compared. Furthermore, most studies, especially the experimental ones, are often carried out at low concentrations of water addition. This is mainly due to the technical difficulties in seeding the gas flows with controlled high steam concentrations. However, it is of particular interest to investigate and understand the behavior of combustion processes when the extinction limits are approached, as this is where the water vapor will have its

most significant impact.

This work focused on the experimental and numerical analysis of a coflow diffusion flame when different diluents are added to the fuel stream and introduced into the combustion process. In particular, the aim of the work was the understanding of the chemical and thermal effects of water addition to a diffusion flame. The work presented in this document can be divided in two main parts: experimental measurements and numerical analysis.

Temperature profiles, extinction limits and OH concentrations were measured with different diluents added to the flame: Ar, N_2, CO_2 and vapor water. A reliable water addition system was developed to obtain precise concentrations of steam in the fuel stream. The measurements show that peak temperatures and extinction limits are comparable between different dilution gases when the heat capacity rate introduced in the fuel line is kept constant. This finding hints that the extinction process is mainly driven by the thermal effects of dilution. If this was the case, temperature would be the only driver of extinction by allowing chain branching reactions to produce the radicals needed for the flame to be sustained. However, OH laser induced fluorescence measurements showed higher concentrations of OH in water diluted flames when compared to CO_2 dilution. Different figures of merit of the measured OH profiles consistently showed larger OH amounts when water was added to the combustion process. This suggests that the extinction process is not only driven by temperature, but the diluents are also actively participating in the reaction. Being the CO_2 flame sustained at the same temperature as the water case, but with lower concentrations of OH, it appears that counterbalancing chemical effects are present in the combustion process when the different diluting species are added to the flame. These experimental results are useful in direct comparison to determine the impact of dilution, but also represent a comprehensive data collection that can be used for model and simulation validation.

Numerical simulations were carried out using the open source combustion software PeleLM developed by the Lawrence Berkeley National Laboratory. The software solves the Navier

Stokes equations for reacting flows in the low Mach number regime. The coflow flame was simulated using the GRI 3.0 chemistry model, and taking advantage of the software adaptive mesh refinement algorithm. This feature is used to regrid the initial coarse numerical mesh according to user defined criteria. The numerical results were necessary to perform radiation corrections for TFP, and to quantify the local quenching species to obtain quantitative measures of OH concentrations. Furthermore, analysis on the O and H concentrations in the diluted simulated flames were carried out. Comparison between experiments and simulations showed a disagreement in the flame position with respect to the burner location at high water concentrations, the numerical results predict a flame that lifts far more than what experiments show when high dilution is introduced in the fuel stream. This disagreement between simulations and experiments was not observed in the CO_2 diluted flame, suggesting that the water simulated flame does not predict well the mixing behavior, or that third body efficiency chemical effects are important and not captured accurately in the simulation. Simulations were shown to predict well the flame peak temperature, especially at high dilution levels. Simulated fluorescence was carried out and compared to experimental florescence results, showing good agreement, especially for the water diluted case. OH concentrations were always higher in the case of H_2O addition with respect to the CO_2 diluted flames at the equivalent levels of heat capacity rate introduced in the domain. However, higher concentrations of O were presents in the CO_2 case. Concentrations of H were shown to be comparable between the two dilution gas cases. This finding indicates that a larger concentration of OH does not directly correlate with a stronger flame, as is often implied by the discussions in the literature about water diluted flames. Other important radicals, such as O and H, are also key to the process as the effect of increase in OH due to water dilution happens at the expense of O and H radical pools. Calculation of the strain rates at the flame edge showed that the straining of the flame does not explain the behavior of the water flame to position itself downstream just before extinction happens. However, it was possible to see that the CO_2 flame edge can positions itself in regions of higher strains. This again, is evidence that

the CO_2 diluted flame is stronger than the water one, even if lower concentrations of OH are present.

As discussed in Chapter 1, the flame configuration studied in this work is relevant for a number of applications. In particular, the results of this dissertation are of particular interest in the combustion of wet fuels, as the boundary of humidification for highly diluted systems can be extrapolated from the data provided in this work. OH PLIF measurements can be used as a tool to monitor combustion processes, such as in flares, to avoid the near extinction region. In fact, the results in this work showed that a roll-off in the measured OH signal appears as the flame is nearing extinction while the measured OH PLIF signal is linearly decreasing with dilution at lower dilution levels. Water has also been used as a means to lower temperature and thus lower emissions from combustion processes. Some of the works found in the literature claim that water diluted flames are stronger because of higher OH concentrations. However, this work shows that carbon dioxide diluted flames are stronger near extinction and can be sustained at a lower temperature and lower OH concentrations. At low levels of dilution the watery flames are possibly stronger than the CO_2 diluted ones but this region is less interesting from the perspective of lowering emissions.

In summary, the main conclusions of the work are as follows:

- The treatment of gaseous diluents as non reactive inerts in the combustion process is reasonable if only the thermal outcome is of interest. Dilution with different gases by introduction of equivalent amounts of thermal capacitance showed similar thermal structures and extinction limits of the coflow flame with additions of water vapor, carbon dioxide, argon and nitrogen in the fuel stream. However, it was shown that water vapor and carbon dioxide are both active reactants in the combustion process, thus not acting as simple diluents. Water vapor dilution enhances OH production, while higher concentrations of the O radical are present with carbon dioxide dilution.

- Specific conditions of the experimental configuration, such as the air coflow velocity, are important to determine the absolute limits of humidification in the flame. However, all the configurations tested provided the same physical insights on the role of water on the enhancement of OH production in the flame.

- Chemistry models predict well peak temperatures with water and carbon dioxide dilution. The predictions are better at high concentrations of diluents as radiation heat losses and heat transfer to the burner, which were not modeled, are smaller. OH concentrations compare well to OH fluorescence measurements after quenching is considered in the numerical model. The experimental results need to be analyzed after considering the large quenching effects of the diluents, especially in the water case.

- The flame ignition location appears to be very sensitive and challenging to be modeled when the fuel is diluted with high concentrations of water. The same issue was not encountered when carbon dioxide was used as a diluent suggesting a mixing related issue in the water flame. This aspect needs further investigation, but it is of particular interest as the 2D coflow flame configuration is the simplest flame model requiring the interaction between the chemistry and transport models. 1D simulations do not permit the analysis of such phenomena.

6.2 Future work

The possibility of introducing fictitious molecules, that mimic the thermal and transport properties of diluents but are non-reactive, into the computational chemistry models, can help in isolating the thermal and chemical effects of different diluents. The H_2O and CO_2 diluted flames will be numerically studied introducing such fictitious molecules into the system to investigate possible differences in temperatures and radical pools.

Previous works on diluted non-premixed counterflow flames at high pressure showed non-monotonic behavior in extinction strain rates with increasing pressures [65]. The authors found that chemical-kinetic mechanisms performed with varying success when predicting the extinction of highly diluted counterflow diffusion flames, suggesting that further investigations of rate parameters are needed to improve the performance of the mechanisms at high pressure. In future work, the diluted diffusion coflow flame will be investigated at higher pressures. The high pressure system allows dilution with different gases, as well as water vapor.

Bibliography

[1] F.L. Dryer. Water addition to practical combustion systems - Concepts and applications. *Symposium (International) on Combustion*, 16(1):279–295, 1977.

[2] A. M. Lentati and H. K. Chelliah. Dynamics of water droplets in a counterflow field and their effect on flame extinction. *Combustion and Flame*, 115(1-2):158–179, 1998.

[3] W. Yang and R.J. Kee. The effect of monodispersed water mists on the structure, burning velocity, and extinction behavior of freely propagating, stoichiometric, premixed, methane-air flames. *Combustion and Flame*, 130(4):322–335, 2002.

[4] C. Arnal, M. U. Alzueta, A. Millera, and R. Bilbao. Influence of water vapor addition on soot oxidation at high temperature. *Energy*, 43(1):55–63, 2012.

[5] Y. Ying and D. Liu. Effects of water addition on soot properties in ethylene inverse diffusion flames. *Fuel*, 247:187–197, 2019.

[6] L. Blevins and R. Roby. An experimental study of NOx reduction in laminar diffusion flames by addition of high levels of steam. *Proceedings of the ASME 1995 International Gas Turbine and Aeroengine Congress and Exposition*, page V003T06A054, 1995.

[7] D. Zhao, H. Yamashita, K. Kitagawa, N. Arai, and T. Furuhata. Behavior and effect on NOx formation of OH radical in methane-air diffusion flame with steam addition. *Combustion and Flame*, 130(4):352–360, 2002.

[8] S. Lee, C.H. Shin, S. Choi, and O.C. Kwon. Characteristics of NOx emissions of counterflow nonpremixed water-laden methane/air flames. *Energy*, 164:523–535, 2018.

[9] A. N. Mazas, B. Fiorina, D. A. Lacoste, and T. Schuller. Effects of water vapor addition on the laminar burning velocity of oxygen-enriched methane flames. *Combustion and Flame*, 158(12):2428–2440, 2011.

[10] T. Le Cong and P. Dagaut. Effect of water vapor on the kinetics of combustion of hydrogen and natural gas: Experimental and detailed modeling study. *Energy & Fuels*, 23(2):725–734, 2009.

[11] I. Glassman. *Combustion*. Academic Press, 3 edition, 1977.

[12] R. Seiser and K. Seshadri. The influence of water on extinction and ignition of hydrogen and methane flames. *Proceedings of the Combustion Institute*, 30(1):407–414, 2005.

[13] J. Suh and A. Atreya. The effect of water wapor on counterflow diffusion flames. *International Conference on Fire Research and Engineering*, pages 103–108, 1995.

[14] J. Park, S.C. Kim, S.I. Keel, D.S. Noh, C.B. Oh, and D. Chung. Effect of steam addition on flame structure and no formation in H_2-O_2-N_2 diffusion flame. *International Journal of Energy Research*, 28(12):1075–1088, 2004.

[15] L. Wang, Z. Liu, S. Chen, C. Zheng, and J. Li. Physical and chemical effects of CO_2 and H_2O additives on counterflow diffusion flame burning methane. *Energy & Fuels*, 27(12):7602–7611, 2013.

[16] S. Lee, R. Padilla, D. Dunn-Rankin, T. Pham, and O.C. Kwon. Extinction limits and structure of counterflow nonpremixed H_2O-laden CH_4/air flames. *Energy*, 93:442–450, 2015.

[17] R.E. Padilla, D. Escofet-Martin, T. Pham, W.J. Pitz, and D. Dunn-Rankin. Structure and behavior of water-laden CH_4/air counterflow diffusion flames. *Combustion and Flame*, 196:439–451, 2018.

[18] F. Liu, J.L. Consalvi, and A. Fuentes. Effects of water vapor addition to the air stream on soot formation and flame properties in a laminar coflow ethylene/air diffusion flame. *Combustion and Flame*, 161(7):1724–1734, 2014.

[19] H. Xu, F. Liu, S. Sun, Y. Zhao, S. Meng, and W. Tang. Effects of H_2O and CO_2 diluted oxidizer on the structure and shape of laminar coflow syngas diffusion flames. *Combustion and Flame*, 177:67–78, 2017.

[20] C. Dai, Z. Shu, P. Li, and J. Mi. Combustion characteristics of a methane jet flame in hot oxidant coflow diluted by H_2O versus the case by N_2. *Energy & Fuels*, 32(1):875–888, 2018.

[21] J. Park, S.I. Keel, and J.H. Yun. Addition effects of H_2 and H_2O on flame structure and pollutant emissions in methaneair diffusion flame. *Energy & Fuels*, 21(6):3216–3224, 2007.

[22] M. Roshandell, J. Santacana-Vall, S. Karnani, J. Botimer, P. Taborek, and D. Dunn-Rankin. Burning ice - Direct combustion of methane clathrates. *Combustion Science and Technology*, 188(11-12):2137–2148, 2016.

[23] T. Kadota and H. Yamasaki. Recent advances in the combustion of water fuel emulsion. *Progress in Energy and Combustion Science*, 28(5):385–404, 2002.

[24] Z. Wang, S. Shi, S. Huang, J. Tang, T. Du, X. Cheng, R. Huang, and J.-Y. Chen. Effects of water content on evaporation and combustion characteristics of water emulsified diesel spray. *Applied Energy*, 226:397–407, 2018.

[25] Y. Solomon, B. Natan, and Y. Cohen. Combustion of gel fuels based on organic gellants. *Combustion and Flame*, 156(1):261–268, 2009.

[26] A.V. Bridgwater. Review of fast pyrolysis of biomass and product upgrading. *Biomass and Bioenergy*, 38:68–94, 2012.

[27] H. Guo, J. Min, C. Galizzi, D. Escudi, and F. Baillot. A numerical study on the effects of CO_2/N_2/Ar addition to air on liftoff of a laminar CH_4/air diffusion flame. *Combustion Science and Technology*, 182(11-12):1549–1563, 2010.

[28] P. Sabia, M. Lubrano Lavadera, G. Sorrentino, P. Giudicianni, R. Ragucci, and M. de Joannon. H_2O and CO_2 dilution in MILD combustion of simple hydrocarbons. *Flow, Turbulence and Combustion*, 96(2):433–448, 2016.

[29] F. Cepeda, A. Jerez, R. Demarco, F. Liu, and A. Fuentes. Influence of water-vapor in oxidizer stream on the sooting behavior for laminar coflow ethylene diffusion flames. *Combustion and Flame*, 210:114–125, 2019.

[30] M. Vicariotto and D. Dunn-Rankin. Temperature profiles and extinction limits of a coflow water-vapor laden methane/air diffusion flame. *Experiments in Fluids*, 59(9):136, 2018.

[31] D. Giassi. *Optical Diagnostics Applied to Quantitative Characterization of Coflow Laminar Diffusion Flames in Microgravity and Normal Gravity.* PhD thesis, Yale University, 2017.

[32] V. Vilimpoc, L.P. Goss, and B. Sarka. Spatial temperature-profile measurements by the thin-filament-pyrometry technique. *Opt. Lett.*, 13(2):93–95, 1988.

[33] V. Vilimpoc and L.P. Goss. SiC-based thin-filament pyrometry: theory and thermal properties. *Symposium (International) on Combustion*, 22(1):1907–1914, 1989.

[34] J.D. Maun, P.B. Sunderland, and D.L. Urban. Thin-filament pyrometry with a digital still camera. *Applied Optics*, 46(4):483, 2007.

[35] B. Ma, G. Wang, G. Magnotti, R.S. Barlow, and M.B. Long. Intensity-ratio and color-ratio thin-filament pyrometry: Uncertainties and accuracy. *Combustion and Flame*, 161(4):908–916, 2014.

[36] R.E. Padilla. *Structure and Behavior of Water-Laden Methane/Air Non-Premixed Flames.* PhD thesis, University of California, Irvine, 2015.

[37] D. Coffin. DCRAW http://www.dechifro.org/dcraw/ (December 2019).

[38] G.P. Smith, D.M. Golden, M. Frenklach, N.W. Moriarty, B. Eiteneer, M. Goldenberg, C.T. Bowman, R.K. Hoanson, S. Song, V.V. Lissianski, W.C. Gardiner, and Z. Qin. http://combustion.berkeley.edu/gri-mech/ (December 2019).

[39] A.C. Eckbreth. *Laser Diagnostics for combustion temperature and species measurements*, volume 3. Gordon and Breach Publishers, 2 edition, 1993.

[40] D. Escofet Martin. *Laser diagnostics for high pressure combustion.* PhD thesis, University of California, Irvine, 2017.

[41] V. Nori and J. Seitzman. *Evaluation of Chemiluminescence as a Combustion Diagnostic Under Varying Operating Conditions*. 46th AIAA Aerospace Sciences Meeting and Exhibit, 2008.

[42] A.G. Gaydon. *The Spectroscopy of Flames*. Chapman and Hall, 1957.

[43] A.G. Gaydon and H.G. Wolfhard. *Flames, their structure, radiation, and temperature*. Chapman and Hall, 1979.

[44] K. Devriendt, H. Van Look, B. Ceursters, and J. Peeters. Kinetics of formation of chemiluminescent $CH(A^2\Delta)$ by the elementary reactions of $C_2H(X^2\Sigma^+)$ with $O(^3P)$ and $O_2(X^3\Sigma_g^-)$: A pulse laser photolysis study. *Chemical Physics Letters*, 261(4):450–456, 1996.

[45] R.W. Schefer. Flame sheet imaging using CH chemiluminescence. *Combustion Science and Technology*, 126(1-6):255–279, 1997.

[46] M. Roder, T. Dreier, and C. Schulz. Simultaneous measurement of localized heat-release with OH/CH_2O-LIF imaging and spatially integrated OH chemiluminescence in turbulent swirl flames. *Proceedings of the Combustion Institute*, 34(2):3549–3556, 2013.

[47] S. Sardeshmukh, M. Bedard, and W. Anderson. The use of OH* and CH* as heat release markers in combustion dynamics. *International Journal of Spray and Combustion Dynamics*, 9(4):409–423, 2017.

[48] L. He, Q. Guo, Y. Gong, F. Wang, and G. Yu. Investigation of OH* chemiluminescence and heat release in laminar methaneoxygen co-flow diffusion flames. *Combustion and Flame*, 201:12 – 22, 2019.

[49] M.F. Kasim, J. Holloway, L. Ceurvorst, M.C. Levy, N. Ratan, J. Sadler, R. Bingham, P.N. Burrows, R. Trines, M. Wing, and P. Norreys. Quantitative single shot and spatially resolved plasma wakefield diagnostics. *Phys. Rev. ST Accel. Beams*, 18:081302, 2015.

[50] R.L. Axelbaum and C.K. Law. Soot formation and inert addition in diffusion flames. *Symposium (International) on Combustion*, 23(1):1517–1523, 1991.

[51] F.G. Roper. The prediction of laminar jet diffusion flame sizes: Part i. Theoretical model. *Combustion and Flame*, 29:219–226, 1977.

[52] OpemFOAM. https://www.openfoam.com/ (December 2019).

[53] Center for Computational Sciences PeleLM and Engineering at LBNL. https://amrex-combustion.github.io/PeleLM/ (December 2019).

[54] M.S. Day and J.B. Bell. Numerical simulation of laminar reacting flows with complex chemistry. *Combustion Theory and Modelling*, 4(4):535–556, 2000.

[55] A. Nonaka, J.B. Bell, M.S. Day, C. Gilet, A.S. Almgren, and M.L. Minion. A deferred correction coupling strategy for low mach number flow with complex chemistry. *Combustion Theory and Modelling*, 16(6):1053–1088, 2012.

[56] E.L. Petersen, D.M. Kalitan, S. Simmons, G. Bourque, H.J. Curran, and J.M. Simmie. Methane/propane oxidation at high pressures: Experimental and detailed chemical kinetic modeling. *Proceedings of the Combustion Institute*, 31(1):447–454, 2007.

[57] A. Matynia, M. Idir, J. Molet, C. Roche, S. de Persis, and L. Pillier. Absolute OH concentration profiles measurements in high pressure counterflow flames by coupling LIF, PLIF, and absorption techniques. *Applied Physics B*, 108(2):393–405, 2012.

[58] B.E. Battles and R.K. Hanson. Laser-induced fluorescence measurements of NO and OH mole fraction in fuel-lean, high-pressure (110 atm) methane flames: Fluorescence modeling and experimental validation. *Journal of Quantitative Spectroscopy and Radiative Transfer*, 54(3):521–537, 1995.

[59] P.H. Paul, J. A. Gray, J.L. Durant, and J.W. Thoman. A model for temperature-dependent collisional quenching of NO $A^2\Sigma^+$. *Applied Physics B*, 57(4):249–259, 1993.

[60] E.C. Rea, A.Y. Chang, and R.K. Hanson. Collisional broadening of the $A^2\Sigma^+ \leftarrow X^2\Pi(0,0)$ band of OH by H_2O and CO_2 in atmospheric-pressure flames. *Journal of Quantitative Spectroscopy and Radiative Transfer*, 41(1):29 – 42, 1989.

[61] Chemkin-Pro. https://www.ansys.com/products/fluids/ansys-chemkin-pro (December 2019).

[62] B. Galmiche, F. Halter, F. Foucher, and P. Dagaut. Effects of dilution on laminar burning velocity of premixed methane/air flames. *Energy & Fuels*, 25(3):948–954, 2011.

[63] C.K. Wu and C.K. Law. On the determination of laminar flame speeds from stretched flames. *Symposium (International) on Combustion*, 20(1):1941–1949, 1985.

[64] J. Natarajan, T. Lieuwen, and J. Seitzman. Laminar Flame Speeds and Strain Sensitivities of Mixtures of H_2 With CO, CO_2 and N_2 at Elevated Temperatures. Turbo Expo 2007:751–760, 2007.

[65] U. Niemann, K. Seshadri, and F.A. Williams. Methane, ethane, and ethylene laminar counterflow diffusion flames at elevated pressures: Experimental and computational investigations up to 2.0 MPa. *Combustion and Flame*, 161(1):138–146, 2014.

[66] Colorado State Unibersity Chemical Equilibrium Calculator. http://navier.engr.colostate.edu/code/code-4/index.html (December 2019).

[67] A.W. Cook. Enthalpy diffusion in multicomponent flows. *Physics of Fluids*, 21(5):055109, 2009.

[68] A. Dasgupta. *Numerical Simulations of Axisymmetric Laminar Diffusion Flames with Soot.* PhD thesis, Pennsylvania State University, 2015.

[69] J.A. Tinajero. *Flame Dynamics and Chemi-Ion Flows Driven by Applied Electric Fields.* PhD thesis, University of California, Irvine, 2017.

[70] T.A. Davidson. *A simple and accurate method for calculating viscosity of gaseous mixtures*. United States Bureau of Mines, 1993.

[71] C. R. Wilke. A viscosity equation for gas mixtures. *The Journal of Chemical Physics*, 18(4):517–519, 1950.

Appendix A

Demosaicking and defocusing

The Nikon D90 camera has a Bayer filter array. Each sensor pixel is associated to a color filter, the filters create a pattern of alternating colors, as shown in Figure A.1. In a raw photograph, the intensity associated to each pixel corresponds to a single color. A demosaicking interpolation algorithm is then needed to evaluate the remaining two color values for each pixel. Figure A.2 shows a raw TFP image before colors are assigned to each pixel. It is possible to see the mosaic created by the Bayer filter array.

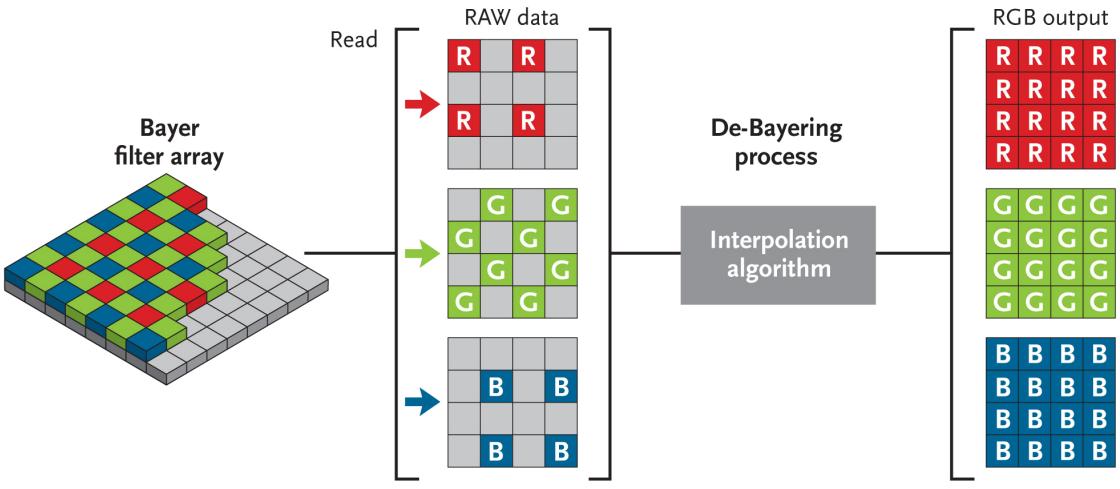

Figure A.1: Bayer filter array and demosaicking (from www.skyandtelescope.com).

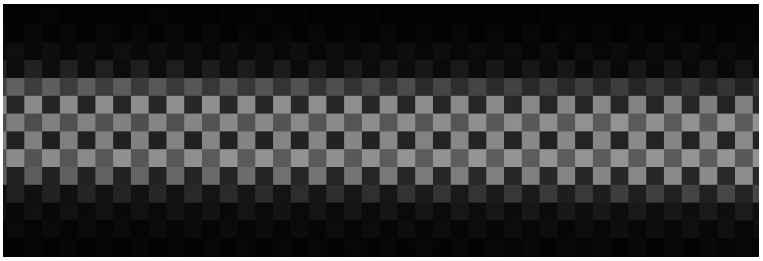

Figure A.2: Raw picture of the fiber, before demosaicking.

Commercial cameras, as the one used in this work, internally apply demosaicking to the pictures when converting the images to common formats (i.e ".jpeg"). Taking the TFP images and processing them with DCRAW allows to control the type of algorithm used for demosaicking. Using DCRAW software it is possible to choose between four different types of demosaicking algorithms: high speed and low quality bilinear interpolation, variable number of gradients (VNG) interpolation, patterned pixel grouping (PPG) interpolation, or adaptive homogeneity-directed (AHD) interpolation. It is not in the objectives of this work to go into details on how the interpolations algorithms function, however some examples of processed TFP images with different demosaicking methods are reported below. Two different cases are reported: the first is an image focused on the SiC fiber, in the second case the fiber is slightly out of focus. Figures A.3 (d) and A.4 (d) show how the demosaicking algorithm greatly impacts the processed TFP focused image. In Figure A.3 the AHD interpolation method is used, while the VNG one is used in Figure A.4. Plots (a), (b) and (c) report the pixel intensity values for each horizontal line where the TFP signal is visible. Since the fiber width is resolved in only a few pixels it is possible to see, especially in the blue channel, that the array lines where the blue filters are missing are not well resolved by the AHD interpolation method. This has a great effect on the color ratios as seen in Figure A.3 (d). The VNG interpolation method improves the color ratios vs temperature output, suggesting that the method can better handle the lack of information caused by the focusing on the fiber creating a more uniform color distribution. Figures for the other two demosaicking methods can be found below (Figures A.7, A.8, A.9 and A.10).

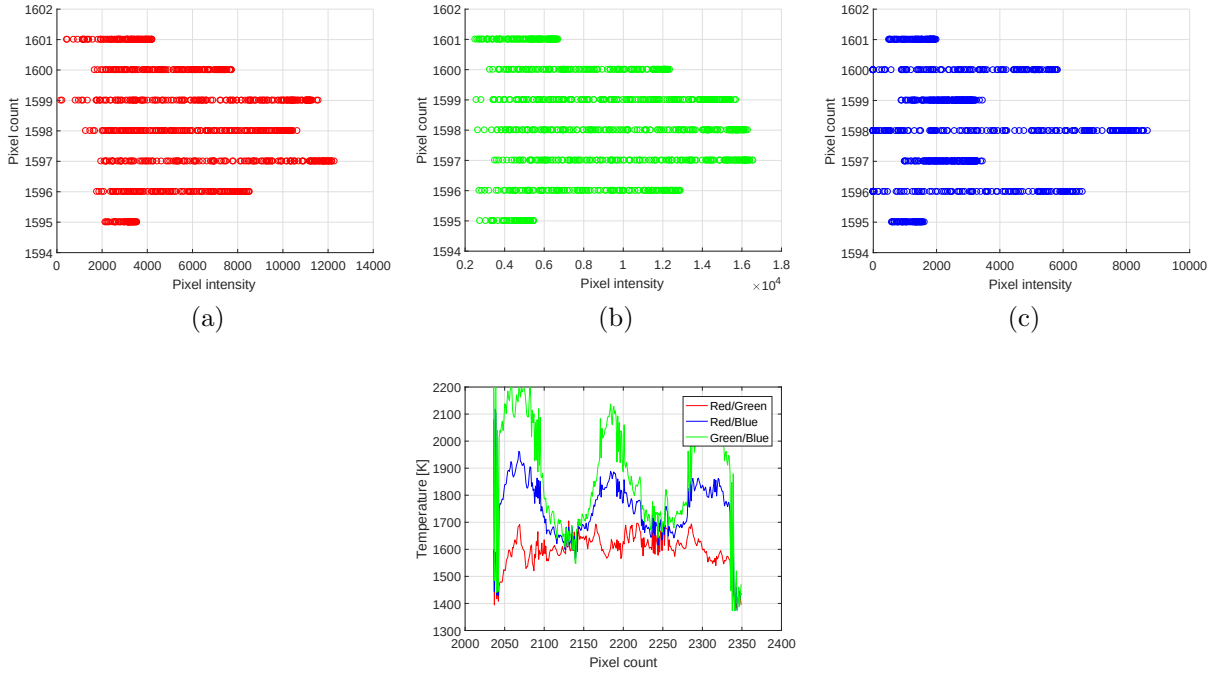

Figure A.3: Focused image, adaptive homogeneity-directed interpolation algorithm.

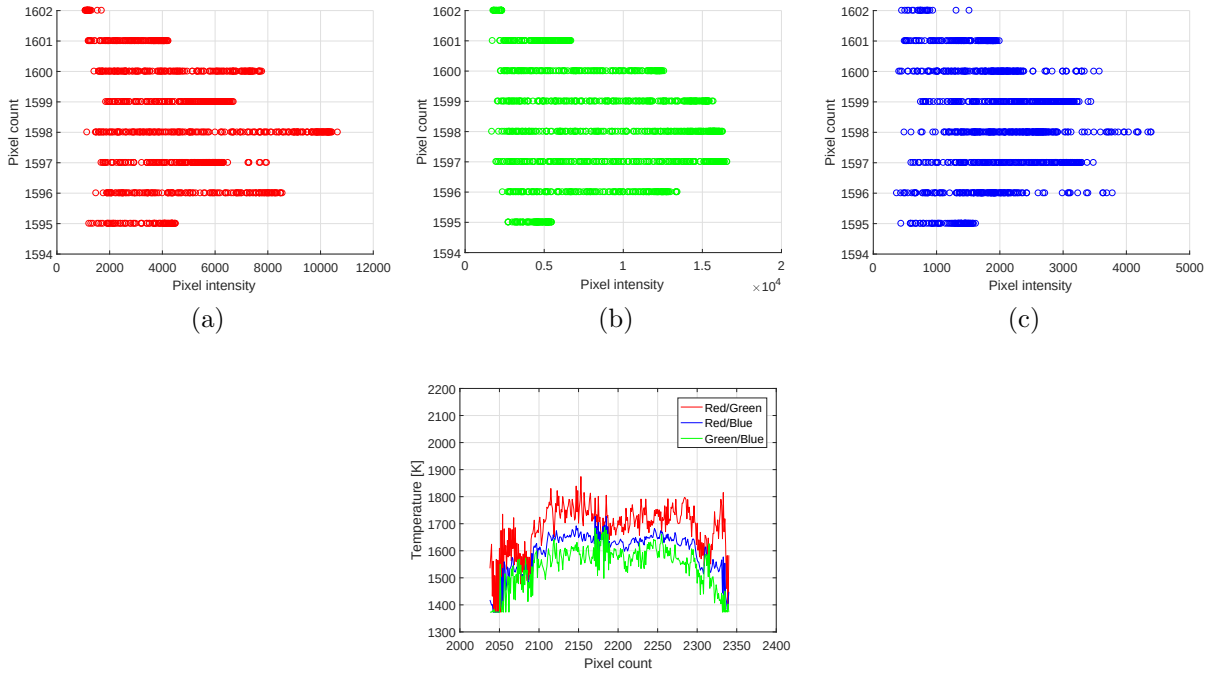

Figure A.4: Focused image, variable number of gradients interpolation algorithm.

Figures A.5 and A.6 are obtained using the AHD and VNG interpolation methods, respectively, on de-focused fiber image. It is clear that as the fiber width is now resolved with a larger number of pixels, and using different demosaicking algorithms does not effect the color ratio results as much as in the focused case. All the TFP measurements were then taken de-focusing the fiber and using the VNG interpolation method.

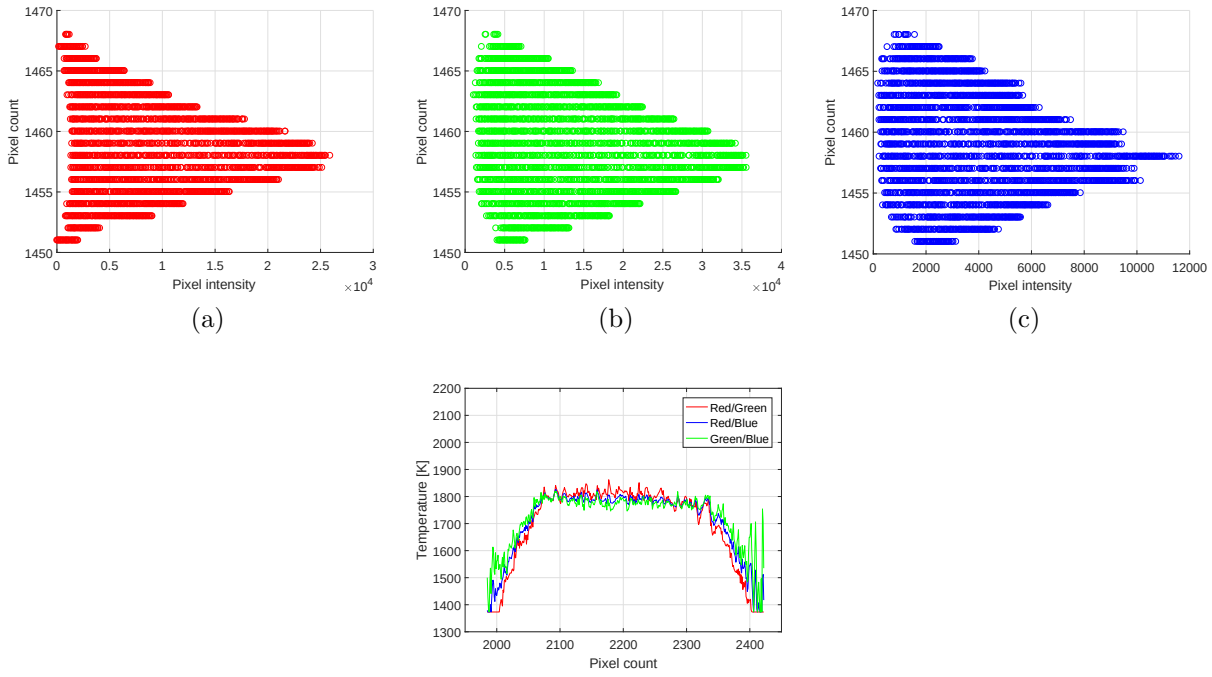

Figure A.5: Defocused image, adaptive homogeneity-directed interpolation algorithm.

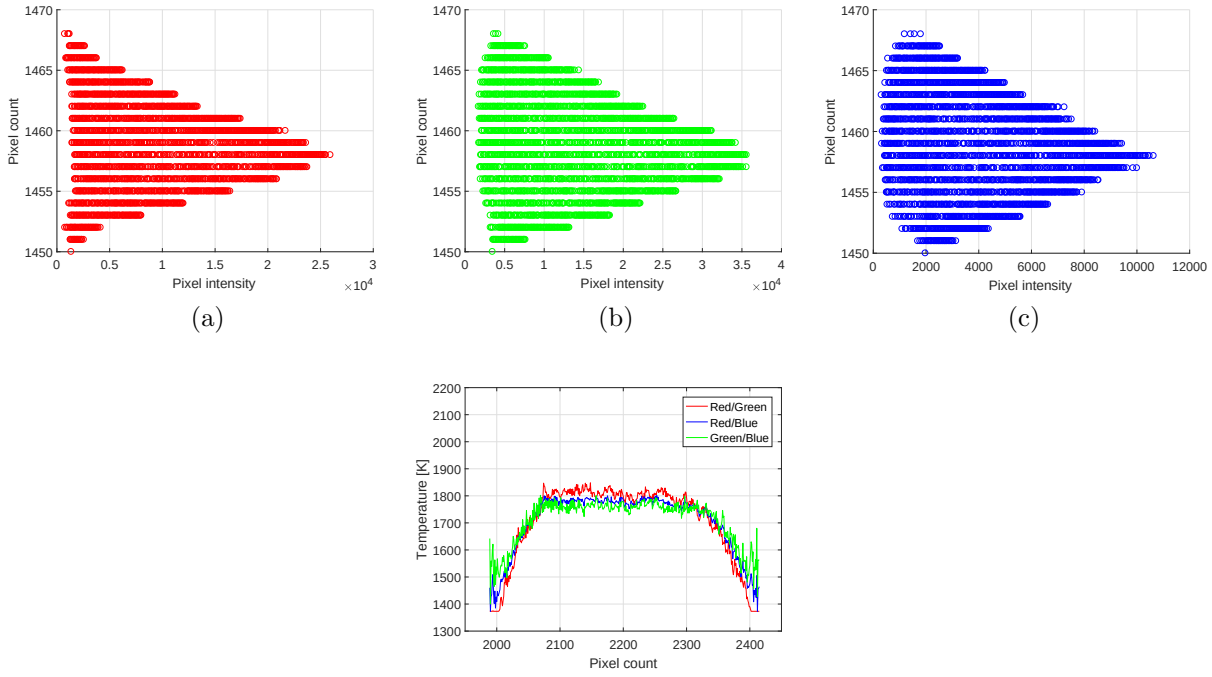

Figure A.6: Defocused image, variable number of gradients interpolation algorithm.

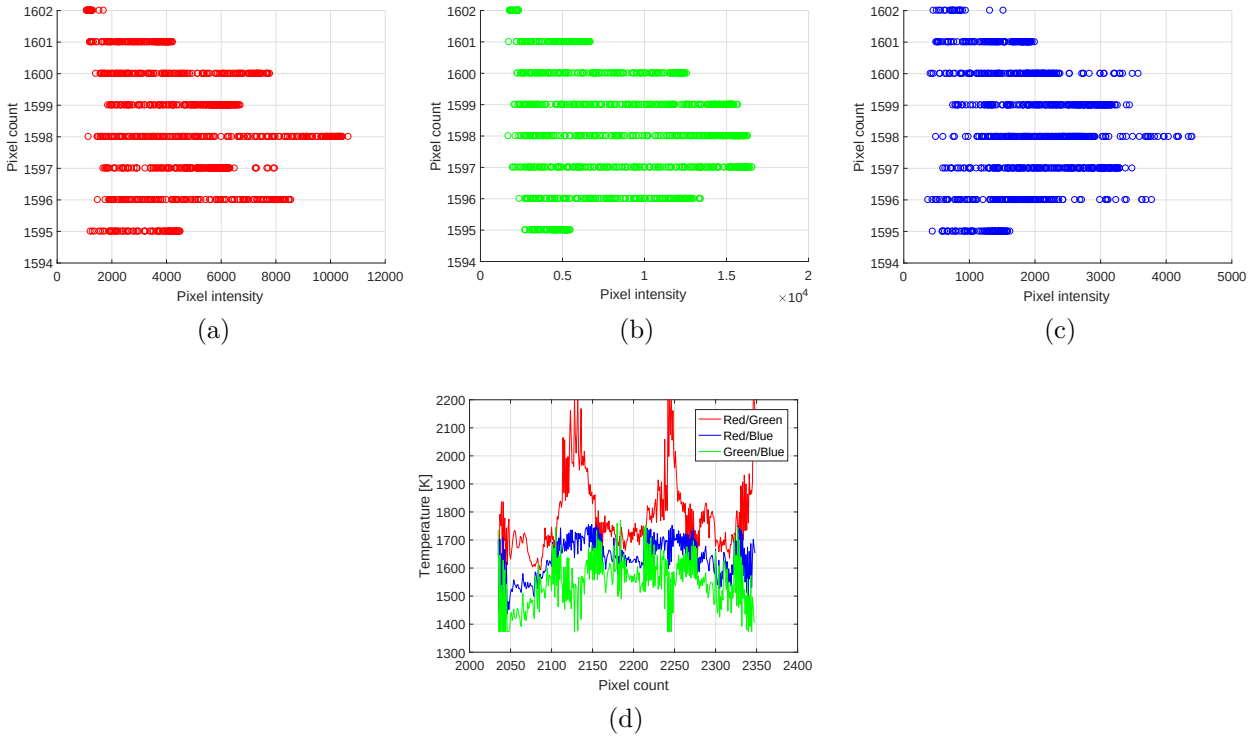

Figure A.7: Focused image, high-speed, low-quality bilinear algorithm for demosaicking.

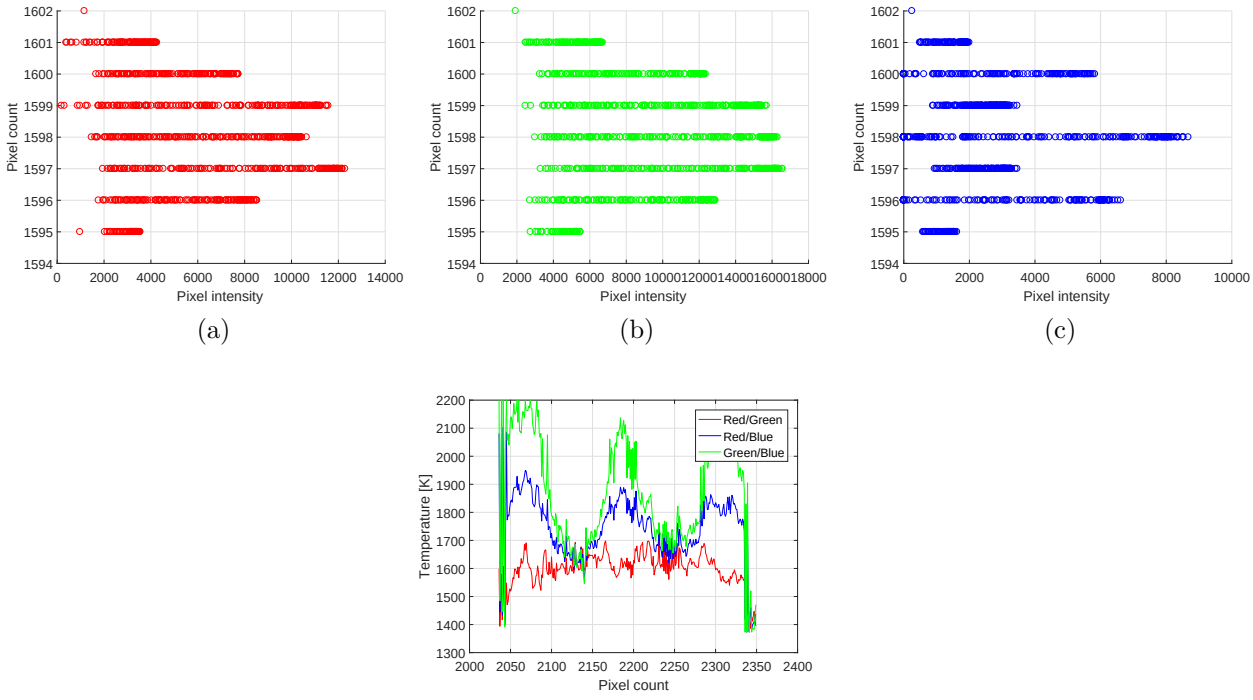

Figure A.8: Focused image, patterned pixel grouping algorithm for demosaicking.

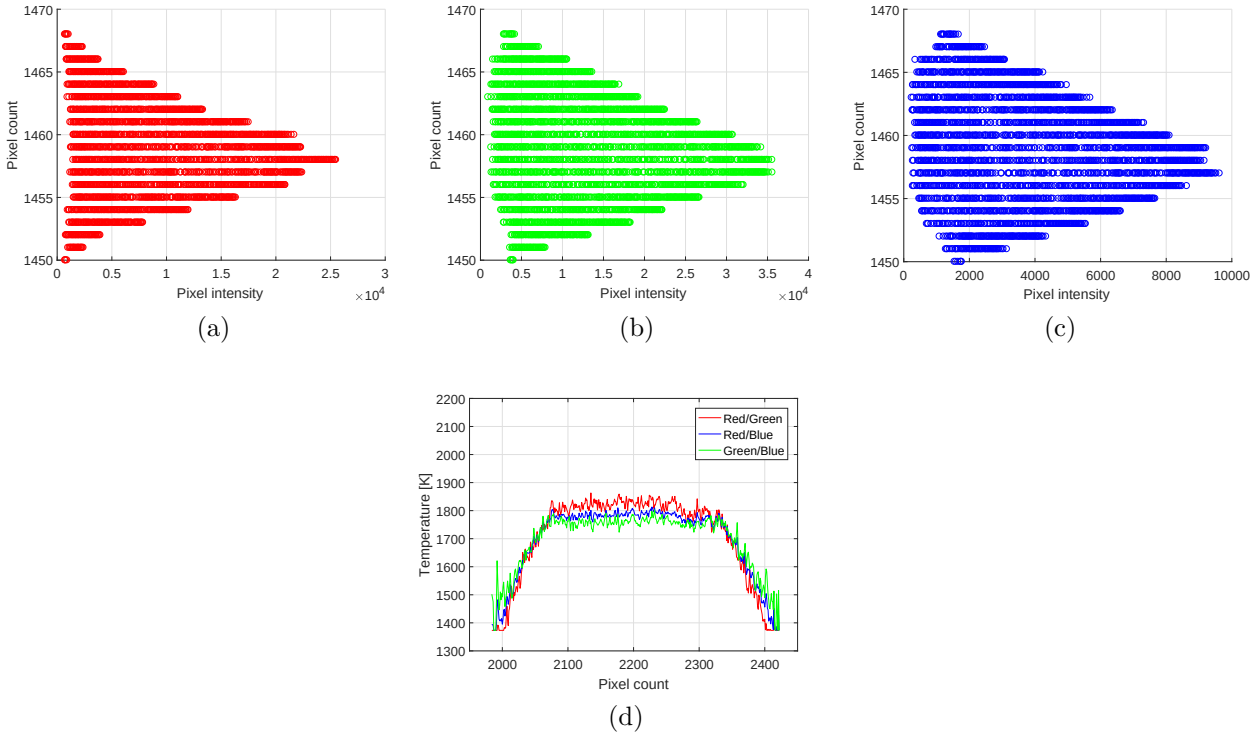

Figure A.9: Defocused image, high-speed, low-quality bilinear algorithm for demosaicking.

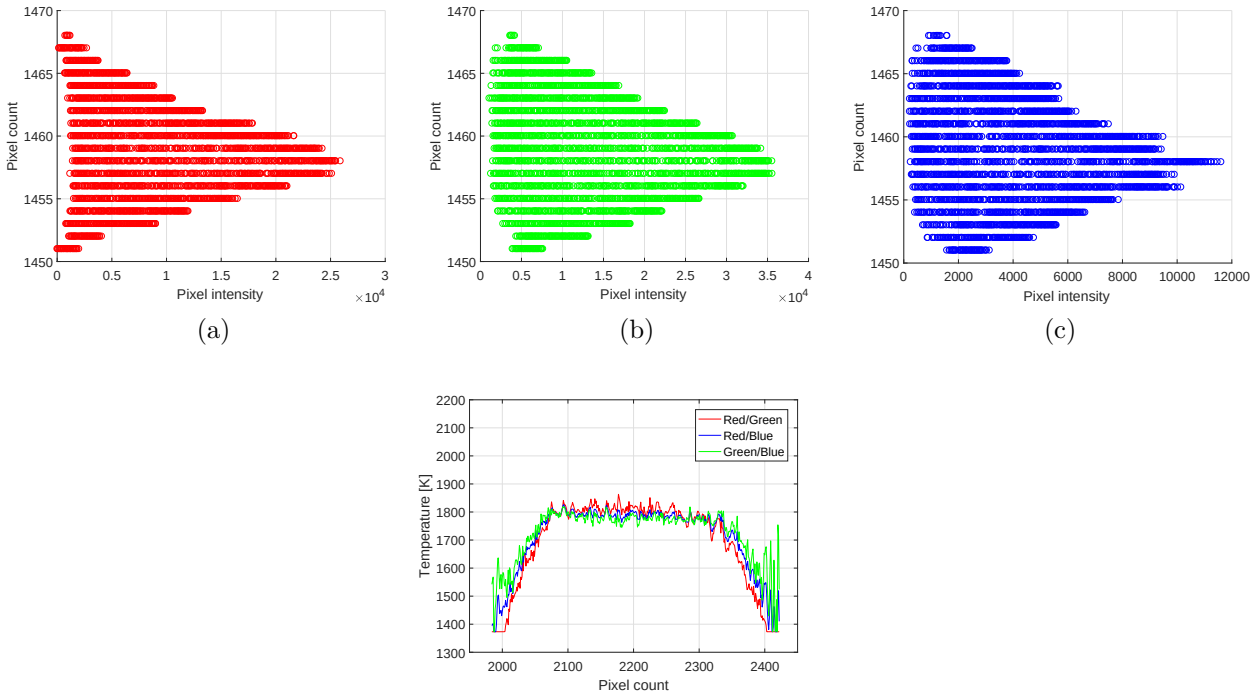

Figure A.10: Defocused image, patterned pixel grouping algorithm for demosaicking.

Appendix B

Raw temperature profiles

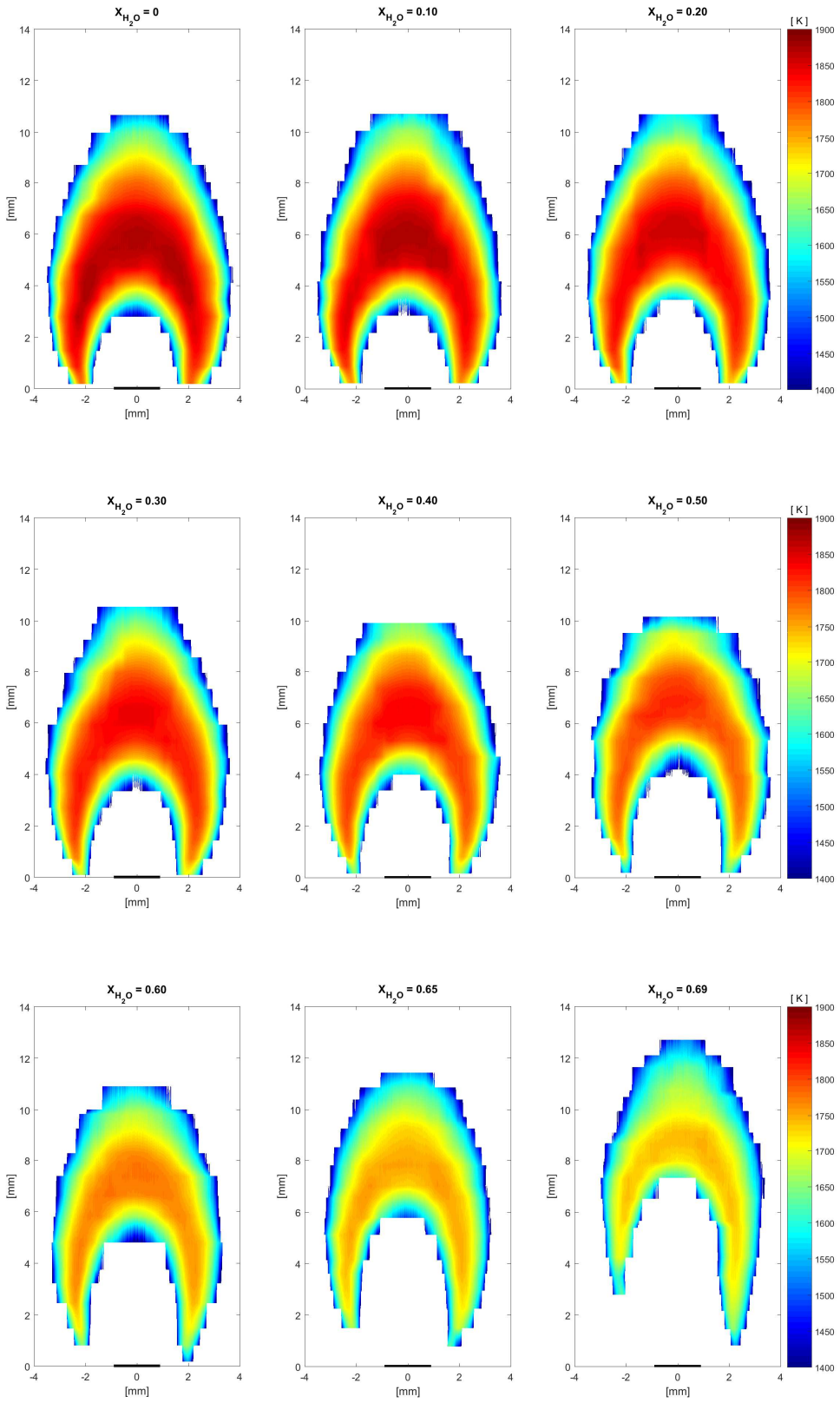

Figure B.1: Raw temperature contours of water diluted flame.

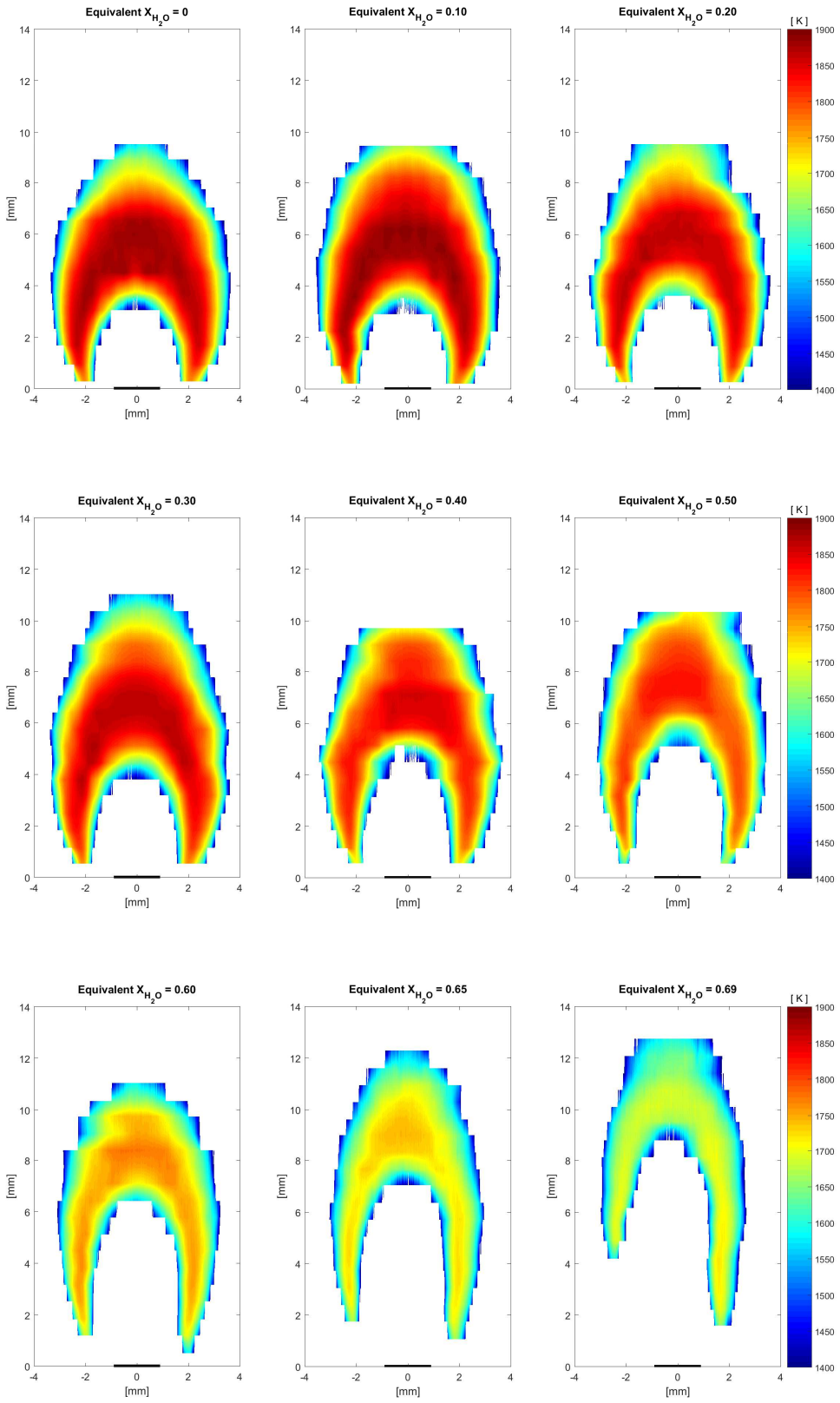

Figure B.2: Raw temperature contours CO_2 diluted flame.

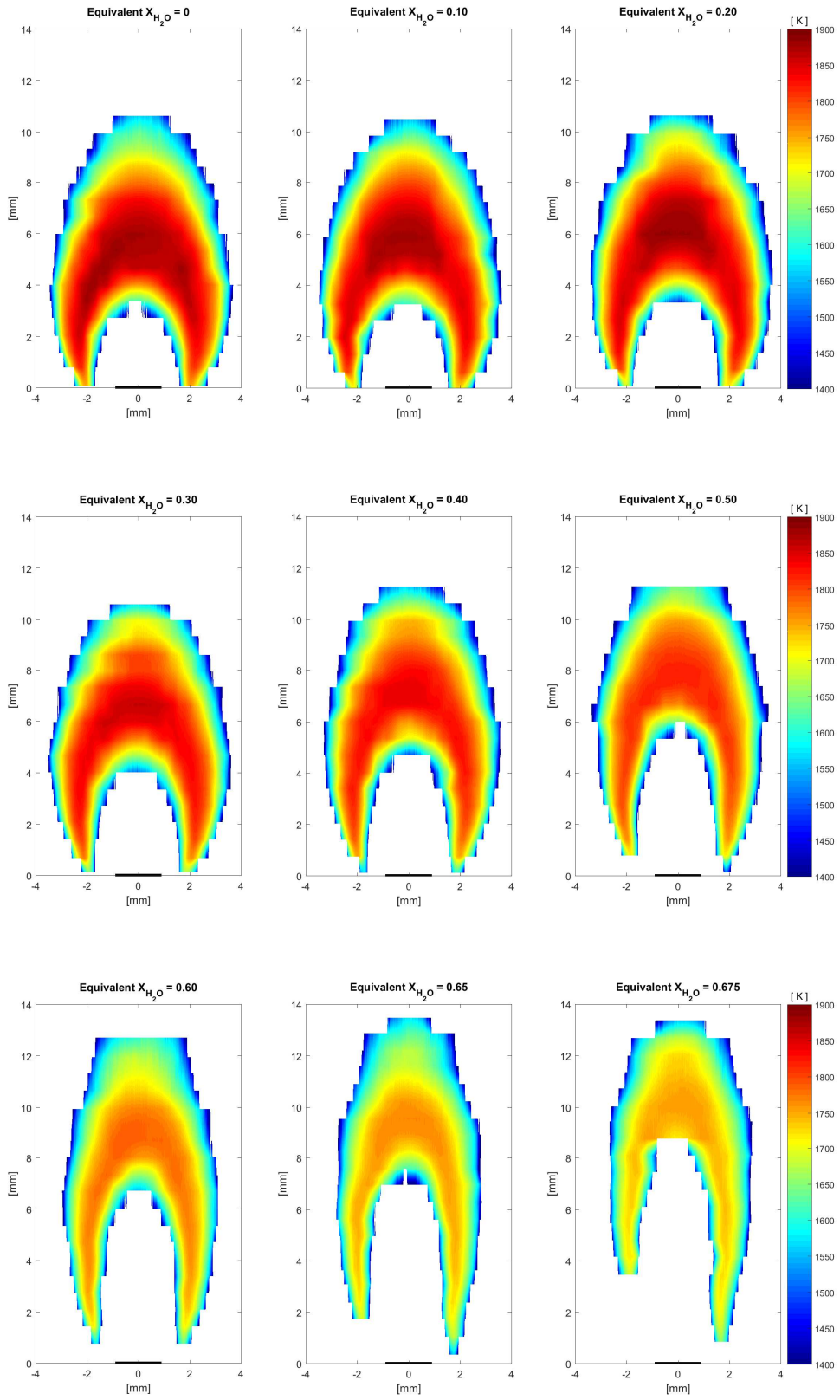

Figure B.3: Raw temperature contours Ar diluted flame.

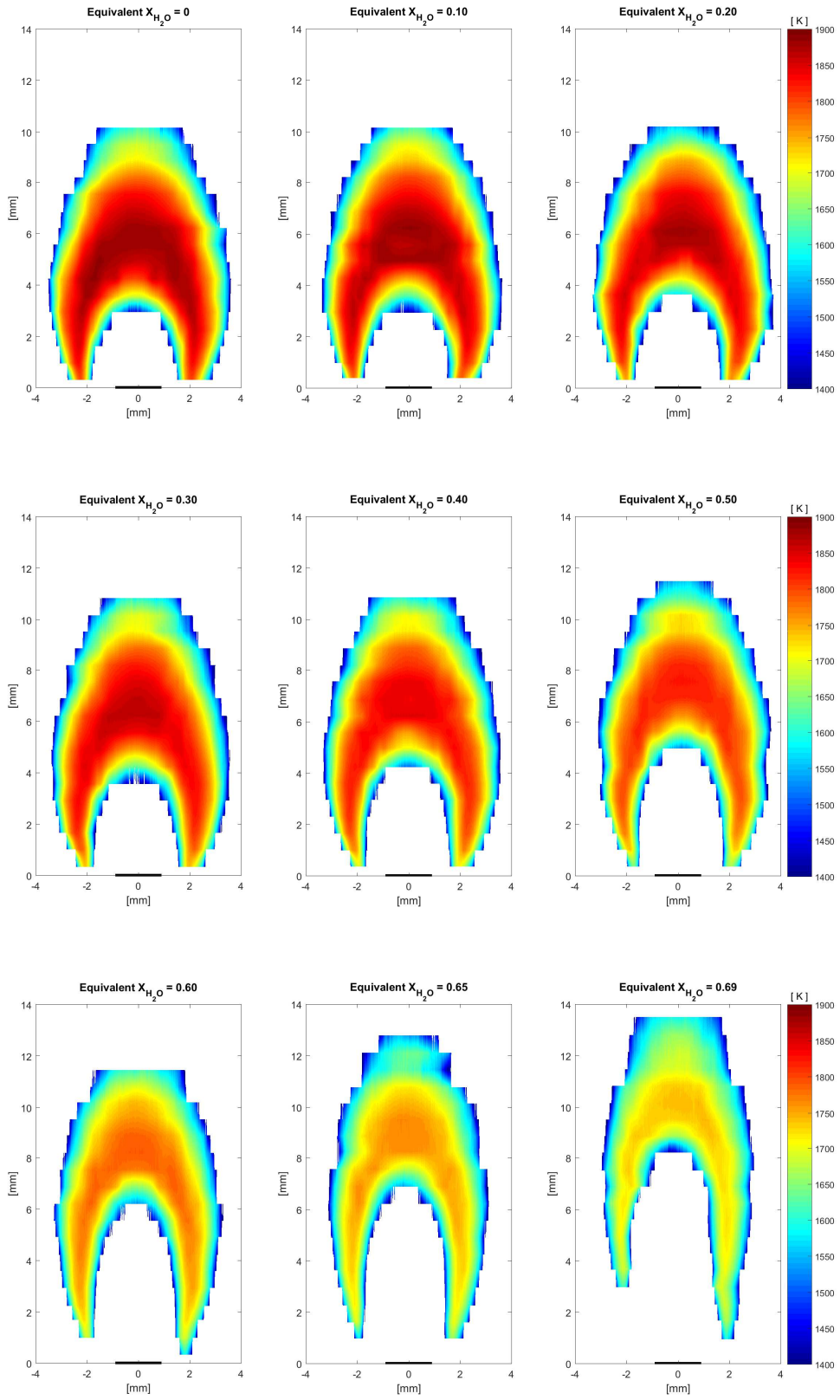

Figure B.4: Raw temperature contours N_2 diluted flame.

Appendix C

Additional PLIF results

Figures C.1 and C.2 shows the OH fluorescence images for the diluted flames when the air velocity matches, at each condition, the velocity of the fuel mixture. As in the case for fixed air velocities, the water and the carbon dioxide diluted flames extinguish at a similar heat capacity rate. Moreover, the water diluted flames still shows the a larger lift-off before extinction when compared to the CO_2 dilution case. Thus, this behavior cannot be related only to the coflow velocity.

Figure C.3 and C.4 show the experimental integrated OH signal normalized to the non diluted flame case. Standard deviations for the 1000 images takes at each condition are also reported to be always less than 5%.

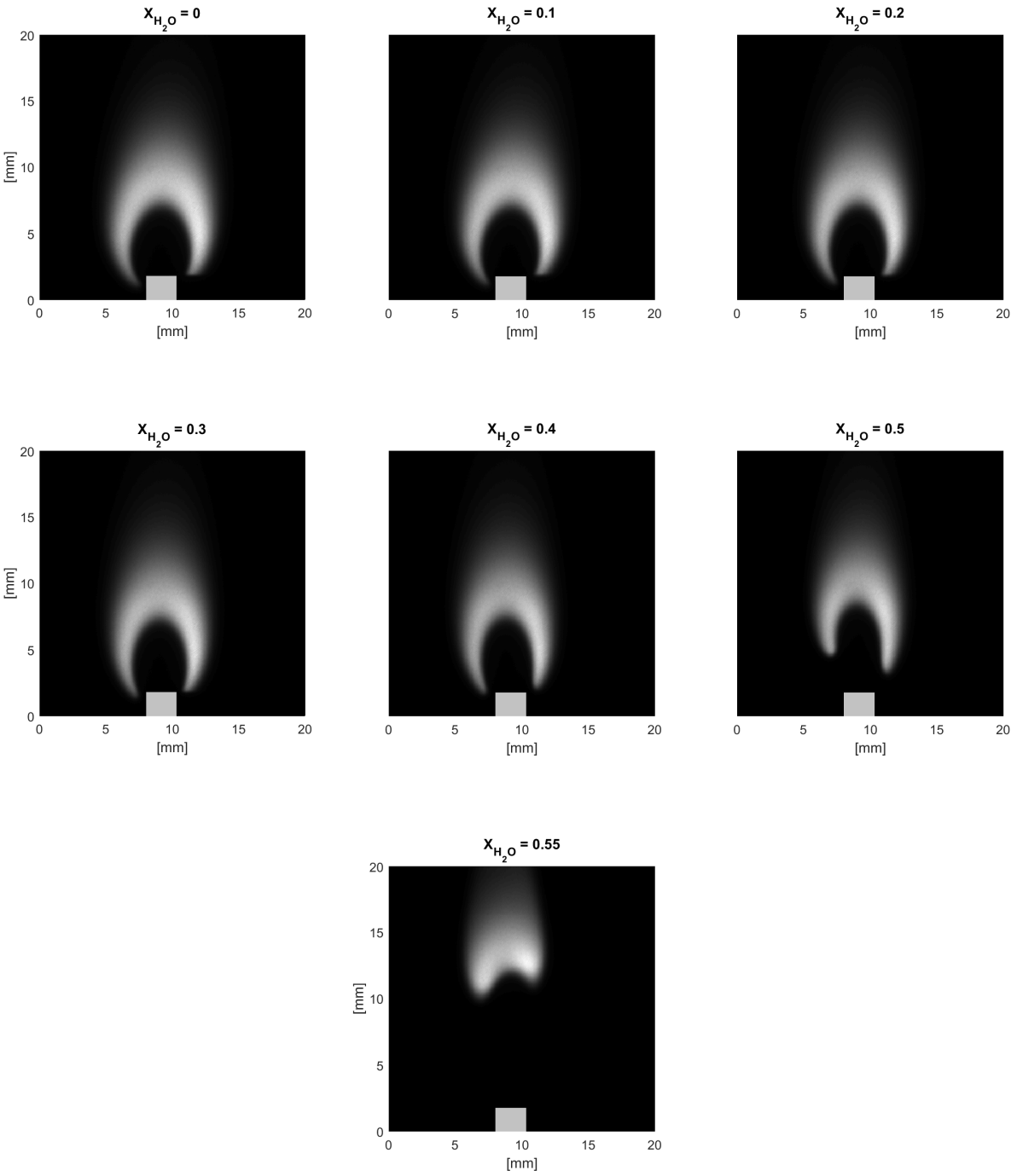

Figure C.1: OH PLIF images of water diluted flame, air coflow velocity matched to fuel velocity.

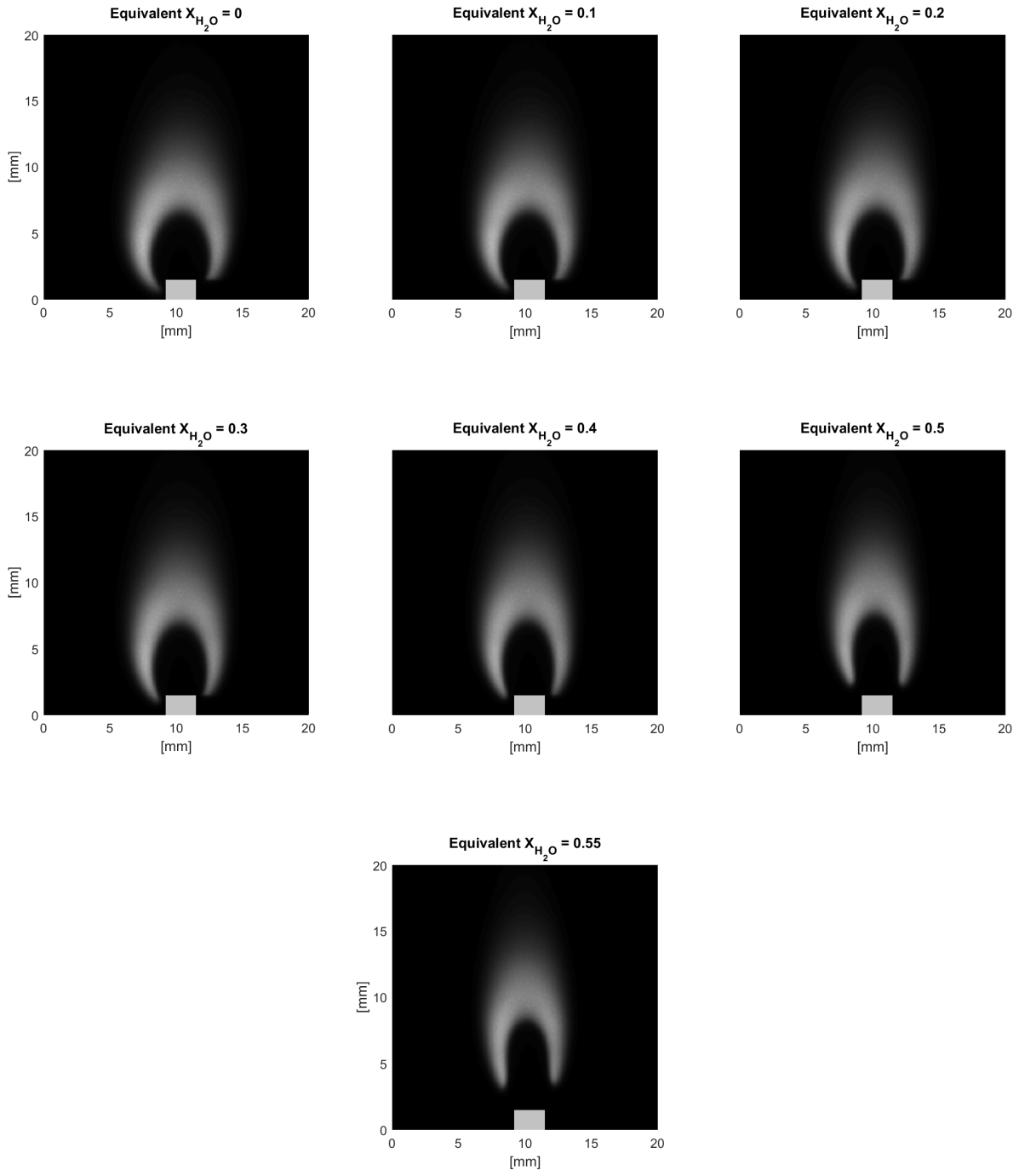

Figure C.2: OH PLIF images of CO_2 diluted flame, air coflow velocity matched to fuel velocity.

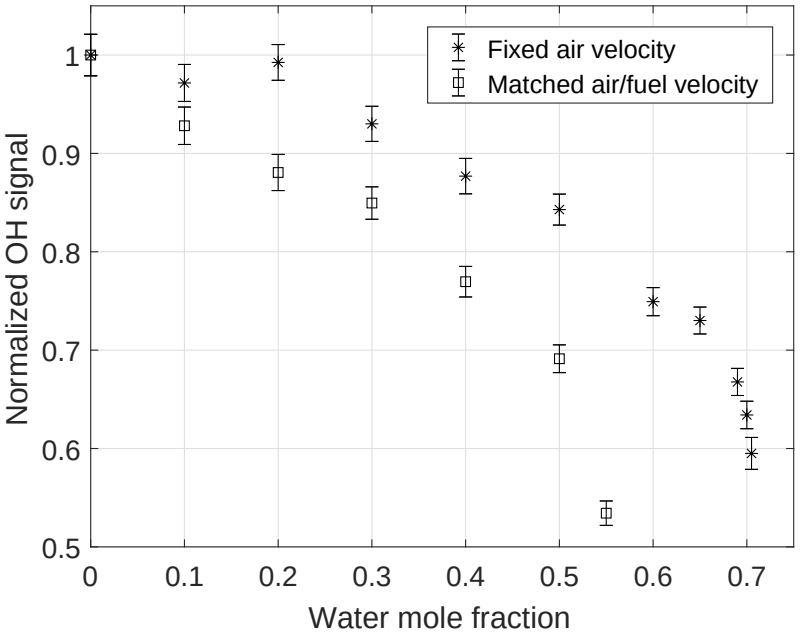

Figure C.3: Integrated OH signal of the water diluted flame.

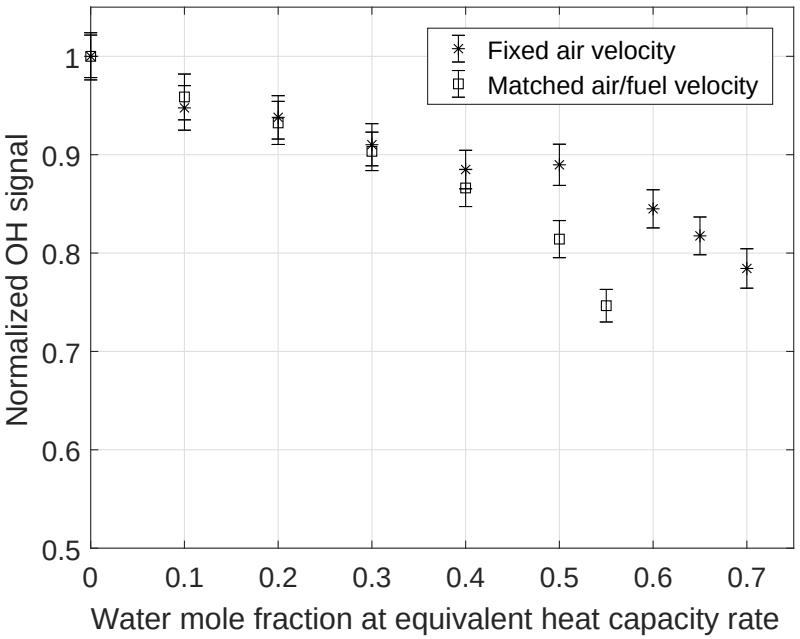

Figure C.4: Integrated OH signal of the CO_2 diluted flame.

OH PLIF experiments were also performed by keeping the flame adiabatic temperature constant. The adiabatic flame temperature of the water diluted flame near extinction (at 0.7 water mole fraction in the fuel line), was calculated using the Colorado State University Chemical Equilibrium Calculator [66]. Keeping this temperature constant, N_2 was substitute to water in the fuel stream in increasing concentration until methane was only diluted with nitrogen. The same procedure was followed for the CO_2 dilution case. For the carbon dioxide condition, the adiabatic flame temperature is still the same as in the water case, which correspond to a flame diluted with 0.65 CO_2 mole fraction in the methane stream. To keep the adiabatic flame temperature constant and equal to the 0.7 water mole fraction case, the addition of N_2 would need to be above the extinction limit that was already tested and reported in previous chapter. Thus, to have a flame at such condition, the air coflow flow was decreased by half. In those experiments, the coflow velocity was 23 cm/s. In such a condition the diluted flame is expected to lift-off and extinguish at a higher diluent concentration. However, the aim of this particular experiment was not to look at extinction limits, but to determine differences in OH concentration only due to chemical effects while keeping temperature constant. The OH PLIF images are reported in Figures C.5 and C.6.

Figure C.7 shows the integrated OH signal, normalized by the first test condition, as a function of diluent mole fraction. Again, the measured OH concentrations follow a similar trend when the flame is diluted with water or carbon dioxide. As quenching effects are larger when water is present, the OH concentration in the case of H_2O dilution is expected to be larger. Moreover, it is possible to see than the decrease in OH detected with PLIF is lower in the case of adiabatic flame temperature with respect to the case reported in Section 5.2.2. This suggests that higher concentrations of OH are present when keeping temperature constant, as it would be expected.

Similar conclusions are found from the experiments reported in Figures C.8 and C.9, where the adiabatic flame temperature was kept constant and equal to the one in the condition of

a 0.3 mole fraction water diluted flame. The integrated OH signals for the water and carbon dioxide diluted flames are shown in Figure C.10.

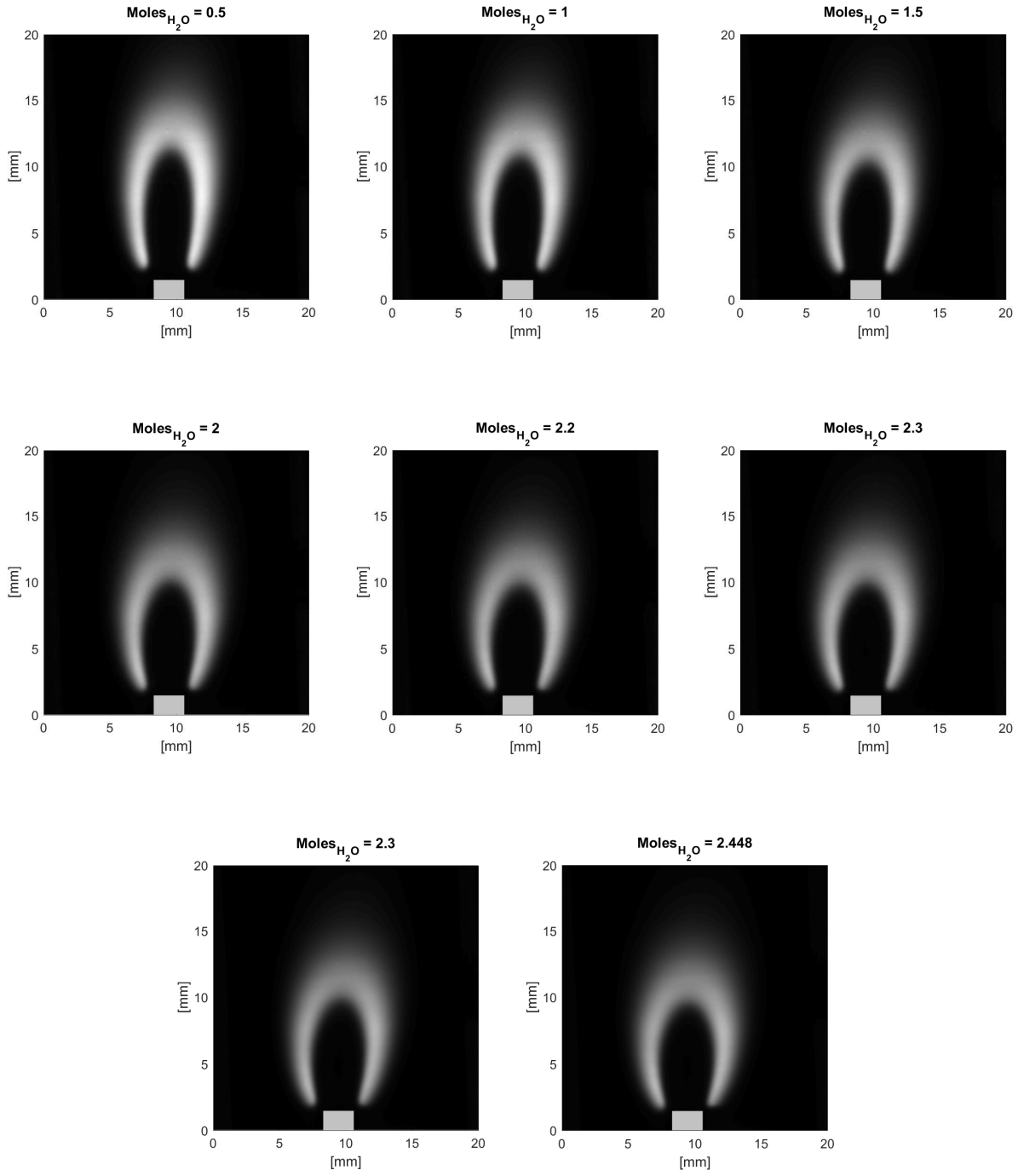

Figure C.5: OH PLIF images of water diluted flames at constant adiabatic flame temperature (flame temperature of the 0.7 water mole fraction diluted flame).

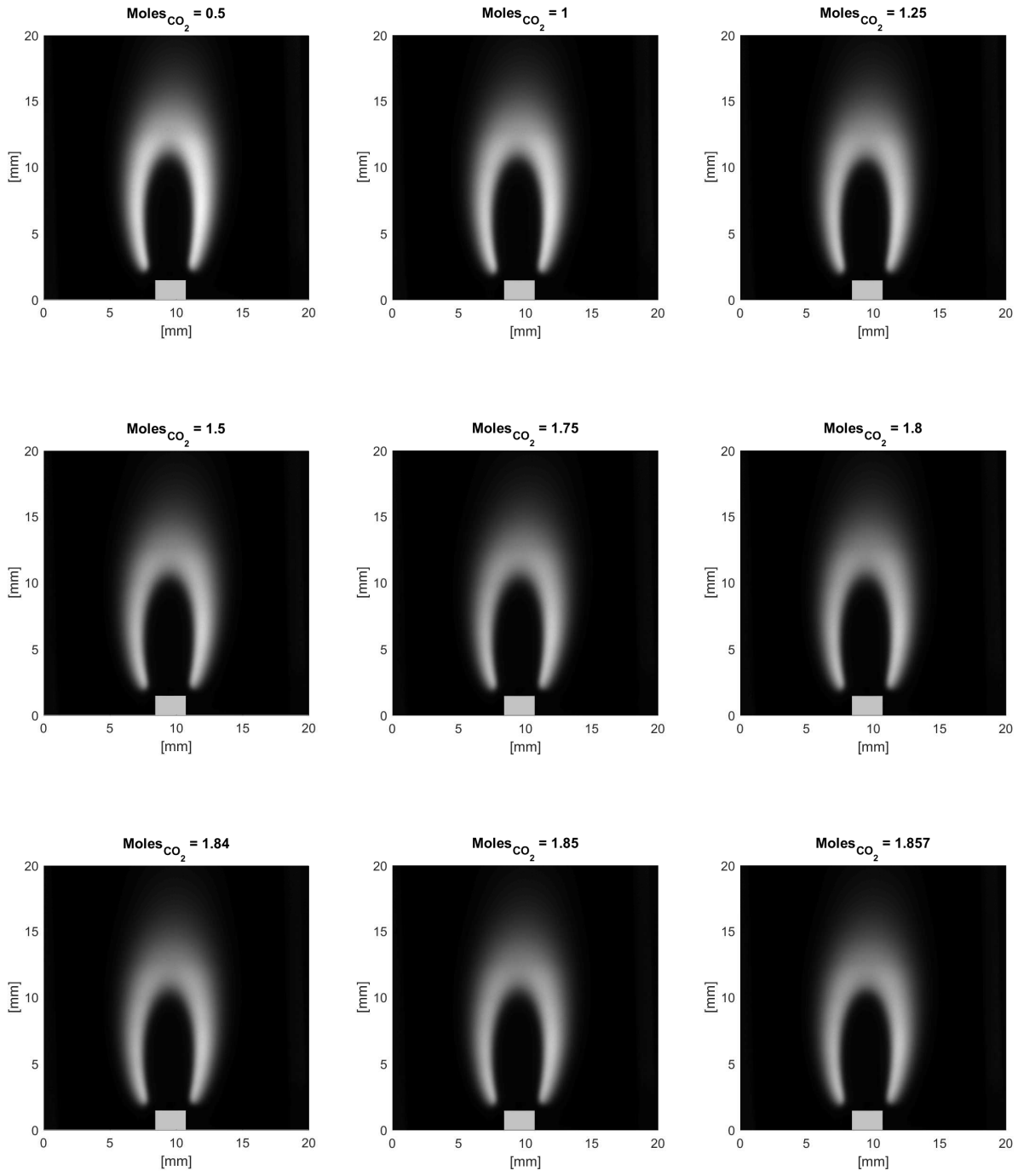

Figure C.6: OH PLIF images of CO_2 diluted flames at constant adiabatic flame temperature (flame temperature of the 0.7 water mole fraction diluted flame).

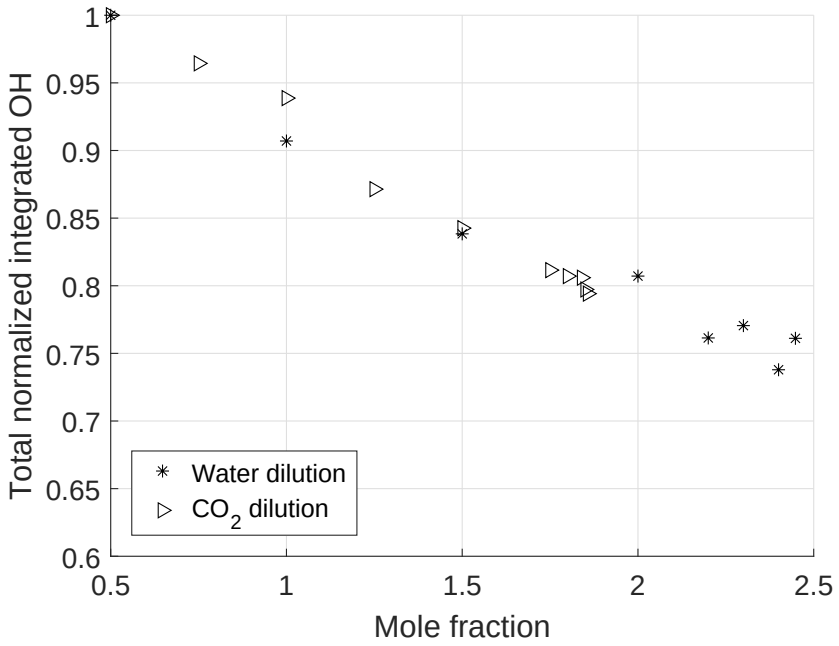

Figure C.7: Integrated OH signal for H_2O and CO_2 diluted flames at constant adiabatic flame temperature (flame temperature of the 0.7 water mole fraction diluted flame).

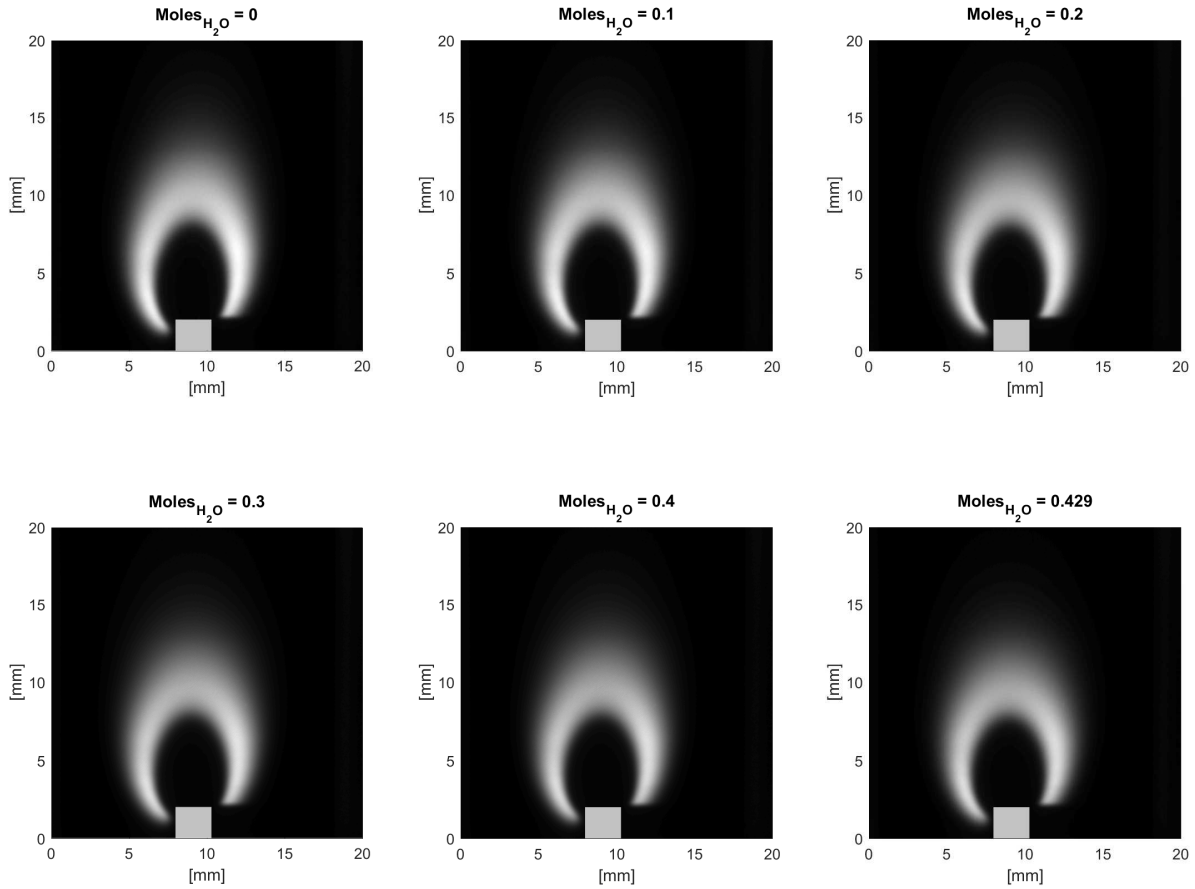

Figure C.8: OH PLIF images of water diluted flames at constant adiabatic flame temperature (flame temperature of the 0.3 water mole fraction diluted flame).

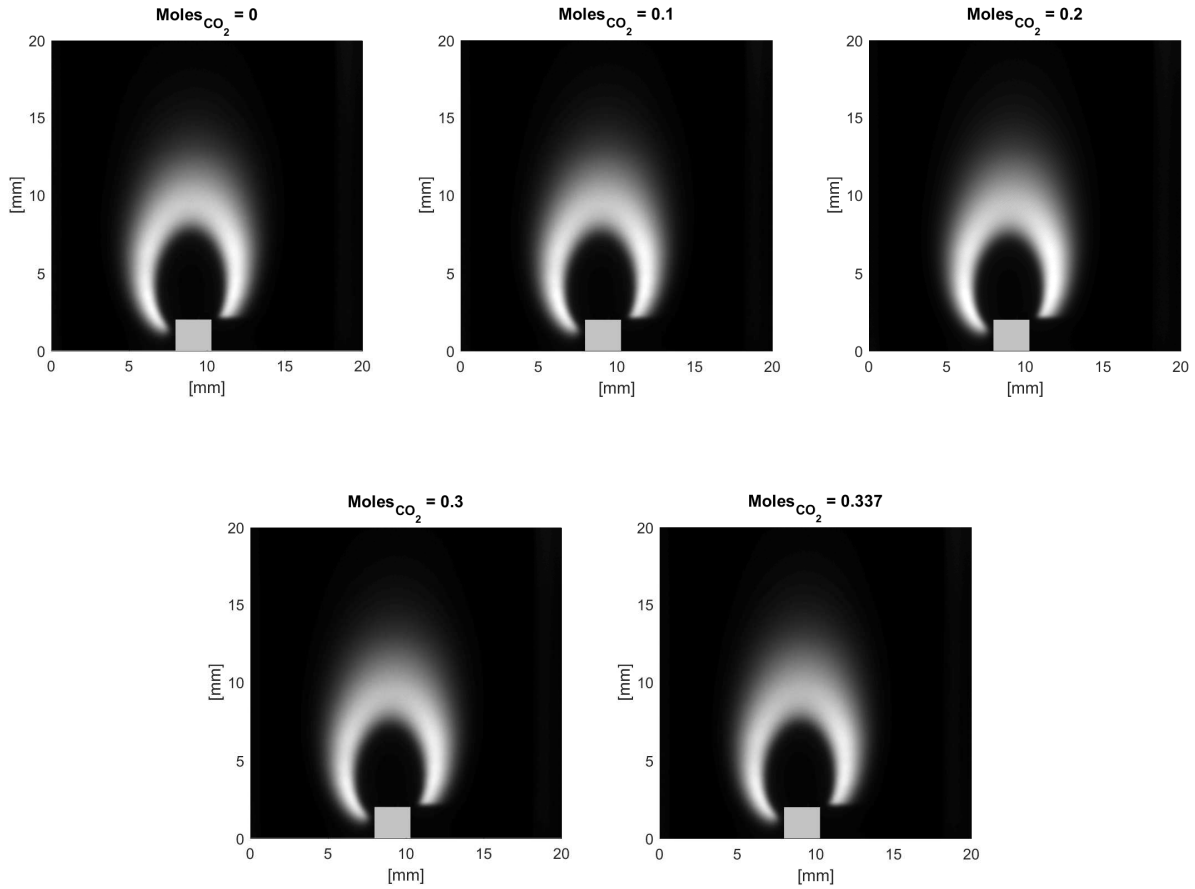

Figure C.9: OH PLIF images of CO_2 diluted flames at constant adiabatic flame temperature (flame temperature of the 0.3 water mole fraction diluted flame).

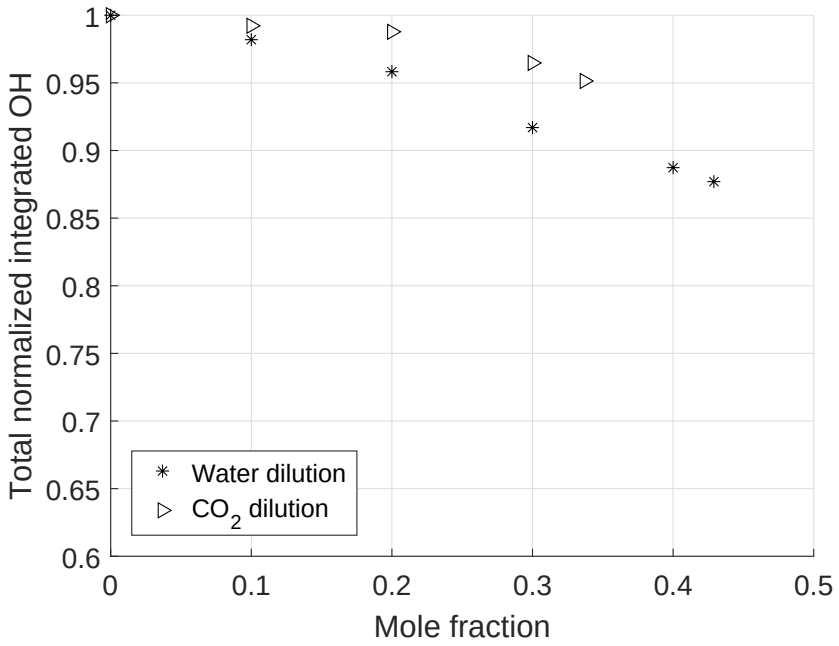

Figure C.10: Integrated OH signal for H_2O and CO_2 diluted flames at constant adiabatic flame temperature (flame temperature of the 0.3 water mole fraction diluted flame).

Appendix D

OpenFOAM computational approach

Simulation in open-source software OpenFOAM were run using the ReactingFoam solver. A three dimensional wedge, with a 5°angle, was used to represent a slice of the axial-symmetric geometry. The tip of the wedge represents the axis of symmetry, the r-z plane has dimensions of 20 mm and 36 mm, respectively. The extruded 6 mm tip of the burner is also accounted for in the mesh geometry. The grid was non-uniform to achieve a finer mesh in the flame zone (33 x 150 μm), and a progressively coarser mesh outside the flame region. Results show no change with smaller grid sizes. The fuel inlet velocity is set as a parabolic fully developed profile, with an average velocity always matched to the corresponding experimental case. The air coflow velocity is set to have a uniform value of 46 cm/s. The simulation is run in three different steps. Firstly, inlet temperatures of fuel, air, and burner wall are set to 800 K and a single-step chemical mechanism is used to ignite the flame to achieve a steady state condition in a short computational time. Secondly, inlet and burner wall temperatures are lowered to 510 K. Finally, the chemical mechanism is changed to GRI-Mech 3.0, the more detailed chemistry including 53 species and 325 reactions. TFP corrections were evaluated with results from the second step, as discussed in Chapter 2.

Figure D.1 shows an example of the OpenFOAM results. Figure D.1 (a) is the case of zero

water dilution, (b) and (c) correspond to 0.6 water mole fraction, constant methane flow rate and constant total mass flow rate respectively. The images show that OpenFOAM predicts well the shrinking of the flame in the condition of constant total flow rate, however temperatures are overestimated with respect to the measured ones. Peak temperatures calculated with OpenFOAM are significantly higher than the ones calculated with PeleLM, which, as discussed in previous chapters, overestimate the measured temperature at low dilution levels but not at higher diluent concentrations.

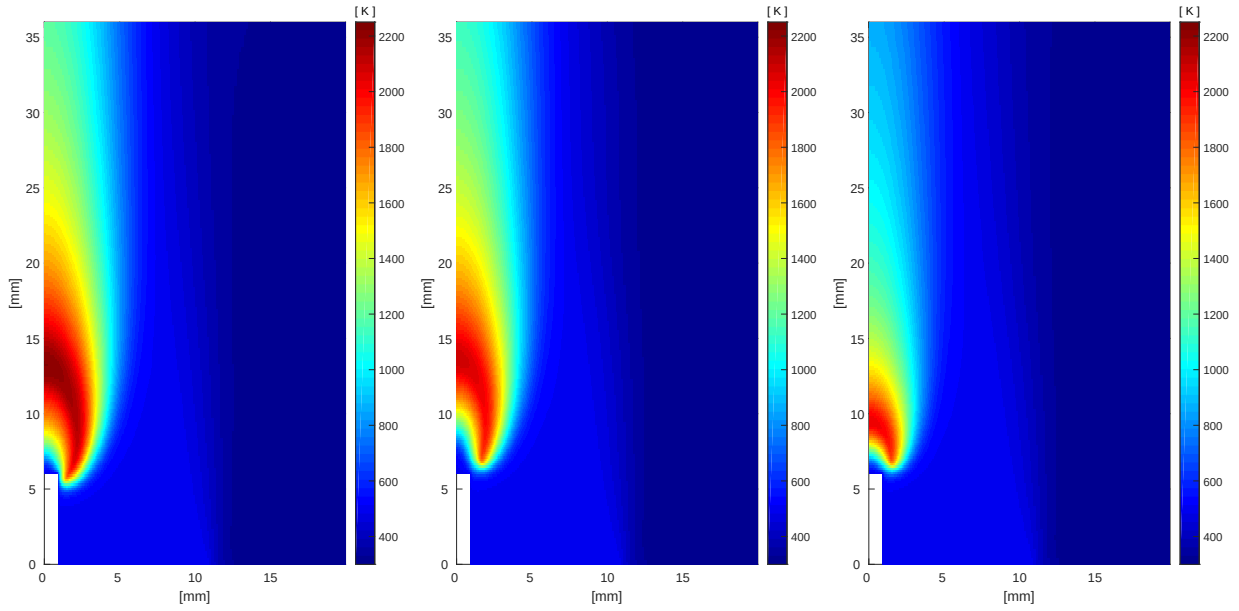

Figure D.1: OpenFOAM temperature profiles: (a) 0 water mole fraction, (b) 0.6 water mole fraction in constant methane flow rate condition, (c) 0.6 water mole fraction in constant total mass flow rate condition.

The choice of using PeleLM instead of OpenFOAM stems from two main differences in the computational approach, in addition to the adaptive mesh refinement method utilized by PeleLM which allows for the mesh to be refined only in selected regions. The first difference in the codes is related to the interdiffusion flux term in the energy equation. This term accounts for enthalpy changes associated with species diffusion. This enthalpy flux is neglected in OpenFOAM, while it is not neglected in PeleLM. The effect of neglecting the interdiffu-

sion flux can be alleviated by assuming unity Lewis number (part of the term cancels out under such assumption); however, unity Lewis number was not assumed for the OpenFOAM simulations in this work. It was shown that omission of the interdiffusion flux can lead to anomalous temperature gradients [67, 68]. This is believed to be one of the reasons for the mismatch in the peak temperatures between OpenFOAM and PeleLM.

The second difference in the computational approaches is related to the evaluation of transport properties. OpenFOAM uses a simplified method to calculate the mixture viscosity and diffusion coefficient. Viscosity of each species μ_i is calculated as a function of temperature through Sutherlands Law:

$$\mu_i = \frac{A_{s_i}\sqrt{T}}{1 + T_{s_i}/T} \tag{D.1}$$

where A_{s_i} and T_{s_i} are gas dependent constants. The mixture viscosity is then computed as a mass average of the μ_i of the N species:

$$\mu = \sum_{i=1}^{N} \mu_i Y_i \tag{D.2}$$

where Y_i is the mass fraction of species i. The mixture mass diffusivity D_m is calculated by assuming fixed Schmidt number equal to 0.7:

$$Sc = \frac{\mu}{\rho D_m} \tag{D.3}$$

The assumption of Schmidt number equal to 0.7 was shown to be a good approximation for a diffusion methane flame [69], however further analysis would be needed to confirm the validity of this assumption for the water-laden methane flame. The diffusion coefficient D_m simplifies molecular diffusion as it is used, without differentiation, in each species continuity equation.

Equation D.2 calculates the mixture viscosity as a simple mass average, lacking separate terms for the interaction of dissimilar molecules [70]. This model is adequate for many mixtures in which the components have nearly the same molecular weight. When the molecular weight ratio is different from unity, mixtures can deviate from this behavior greatly. PeleLM, instead, uses a mixture-averaged approach to evaluate viscosity accounting for the interaction between dissimilar molecules. The Wilke empirical model [71] achieves this with an adjustment term in the denominator of Equation D.2:

$$\mu = \sum_{i=1}^{N} \frac{\mu_i X_i}{\sum_{j=1}^{N} X_j \Phi_{ij}} \tag{D.4}$$

where X_i is the mole fraction of species i, and:

$$\Phi_{ij} = \frac{1}{\sqrt{8}} \left(1 + \frac{W_i}{W_j}\right)^{-1/2} \left(1 + \left(\frac{\mu_i}{\mu_j}\right)^{1/2} \left(\frac{W_j}{W_i}\right)^{1/4}\right)^2 \tag{D.5}$$

where W_i is the molecular weight of species i. Mass diffusivities $D_{i,m}$ are calculated for each species in the mixture i with the mixture-averaged formulation in Equation D.6, accounting for the binary diffusion coefficients D_{ij} of species pair i,j:

$$D_{i,m} = \frac{\sum_{j \neq i} Y_j}{\sum_{j \neq i} X_j / D_{ij}} \tag{D.6}$$

Differently from OpenFOAM, PeleLM evaluates the diffusivity associated to each species in the mixture, without the need of an assumption on the Schmidt or Lewis numbers. This guarantees a more accurate prediction of the transport properties.

Appendix E

Burner tip temperature

The burner tip temperature was monitored using a FLIR SC 620 IR camera. As the emissivity of the fuel tube was not known, the temperature was recorded for different values of emissivity. Figure E.1 shows the temperature for different flame conditions. The line referred as 'No flame', reports the temperature for increasing values of emissivity of the fuel tube tip when the burner was heated, and the air and methane were flowing through the system. The other two lines refer to the tip temperature as the flame was burning with either no dilution, corresponding to no lifting, or with water dilution corresponding to a flame lift-off of about 2 mm. It is clear from the image that, independently from the emissivity, heat transfer to te burner plays an important role for low dilution cases.

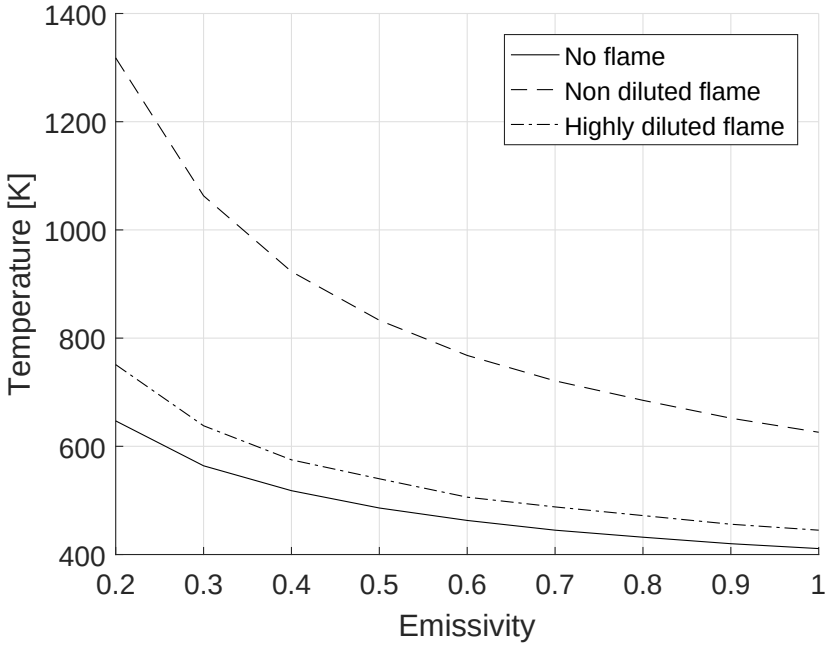

Figure E.1: Burner tip temperatures of lifted and non lifted flames.

Appendix F

Additional simulation results with N_2 dilution

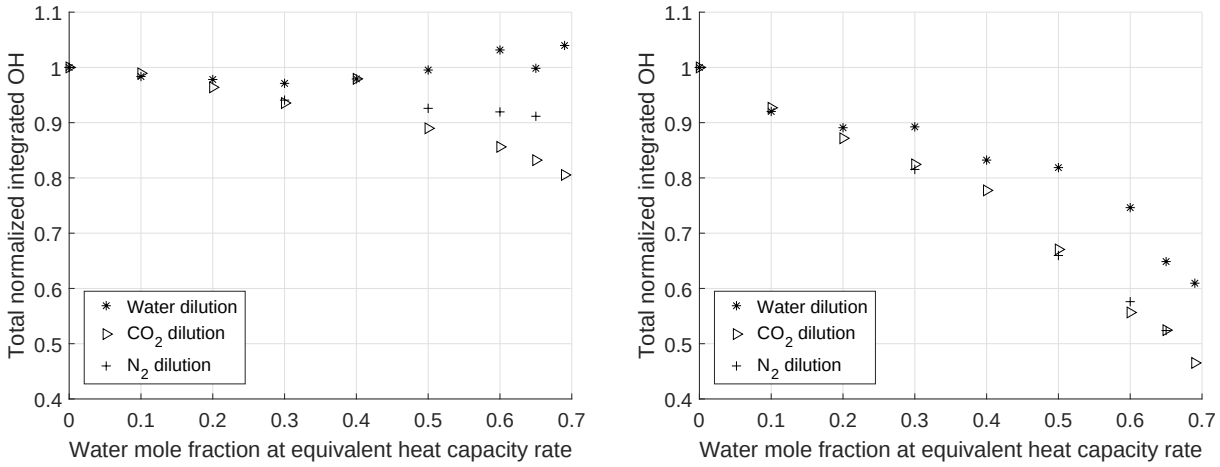

Figure F.1: Simulated OH concentrations for H_2O, CO_2 and N_2 diluted flames: (a) Integrated OH over the whole domain; (b) Integrated OH over the whole domain, normalized by flame wing height.

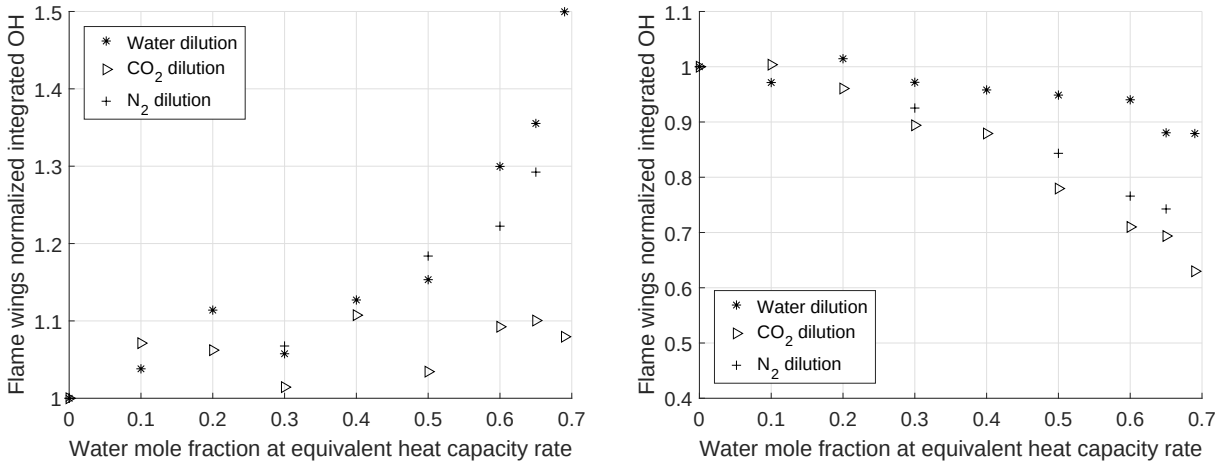

Figure F.2: Simulated OH concentrations for H_2O, CO_2 and N_2 diluted flames: (a) Integrated OH over the wing region; (b) Integrated OH over the wing region, normalized by flame wing height.

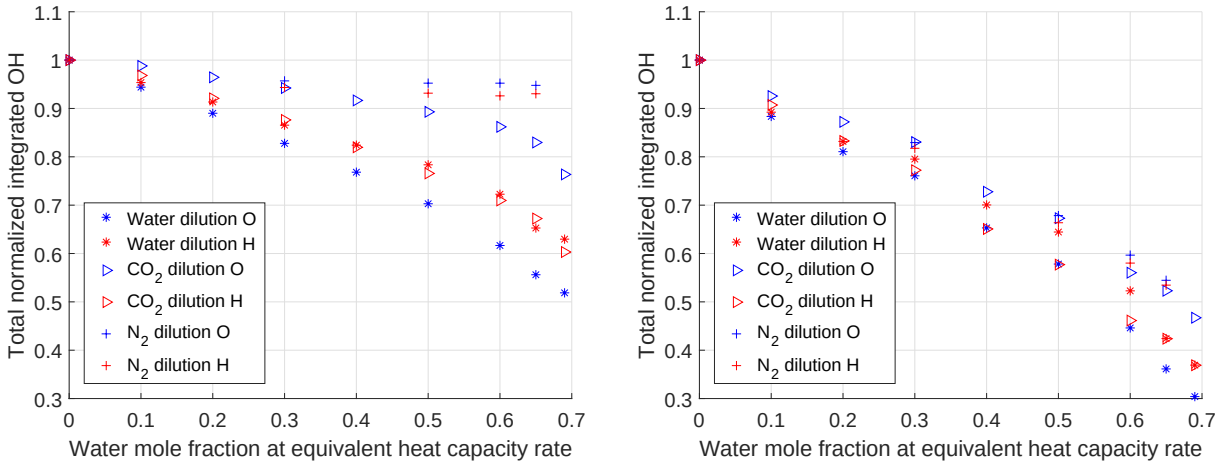

Figure F.3: Simulated O and H concentrations for H_2O, CO_2 and N_2 diluted flames: (a) Integrated O and H over the whole domain; (b) Integrated O and H over the whole domain, normalized by flame wing height.

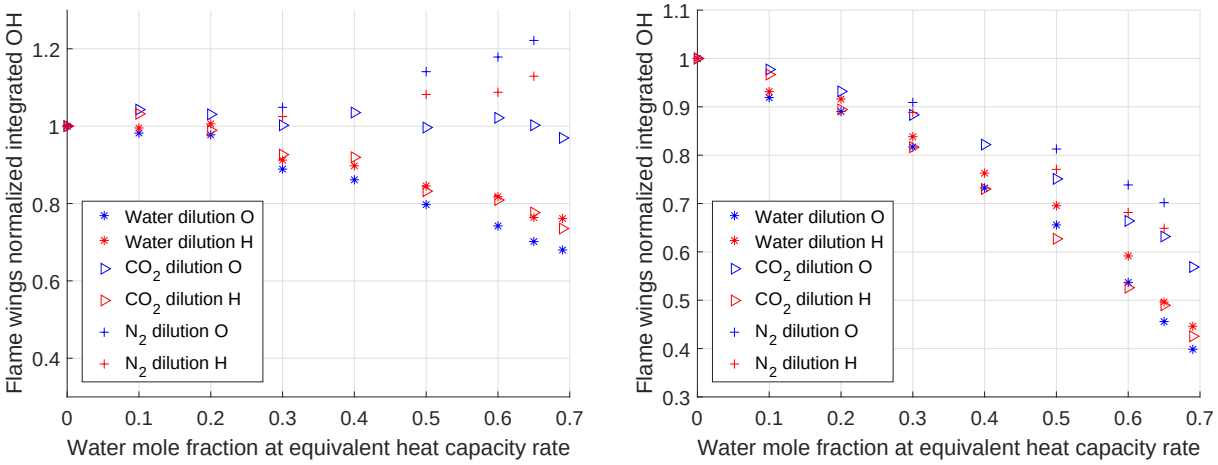

Figure F.4: Simulated O and H concentrations for H_2O, CO_2 and N_2 diluted flames: (a) Integrated O and H over the wing region; (b) Integrated O and H over the wing region, normalized by flame wing height.